A PROSPECTING SYSTEM USING NATURAL ELECTROMAGNETIC RADIATION IN THE E.L.F. BAND

by

CHARLES J.M. HEWLETT, B.A.

A Thesis submitted for the degree

of

DOCTOR OF PHILOSOPHY

AT THE

UNIVERSITY OF LONDON

Geophysics Section, Royal School of Mines

London S.W.7

OCTOBER 1973

TABLE OF CONTENTS

	List of Illustrations	v
	Acknowledgements	ix
	Abstract	1
	Introduction	2
	Chapter 1 MAGNETOTELLURIC AND TELLURIC THEORY	
1.1	Units, coordinate systems, symbols and abbreviations	5
1.2	Solution of Maxwell's equations	6
1.3	Solution of the Scalar Diffusion Equation	10
1.4	The Apparent Resistivity and Skin Depth	12
1.5	The Layered Half-Space Model	14
1.6	Lateral Conductivity Variations	17
1.7	The Telluric Method	19
1.8	The Telluric Tensor	22
	Chapter 2 NATURAL FIELD MEASUREMENTS AND TRANSDUCERS	
2.1	The Geomagnetic Spectrum	25
2.2	Errors in Natural Field Measurements	26
2.3	Uniformity of the Source Field	28
2.4.1	Choice of Magnetometers	29
2.4.2	Design Considerations for Induction Magnetometers	32
2.4.3	Noise	32
2.4.4	The Magnetometer Design	35
2.5.1	Horizontal Electric Field Pickup	36
2.5.2	Signal Pickup Noise	40
2.5.3	The Electric Preamplifier Design	42
2.6	Calibration	43

Chapter 3 PORTABLE RECORDING AND TELEMETRY EQUIPMENT

3.1	General Description of Equipment	47
3.2	Construction	48
3.3	The Main Amplifier Modules	52
3.3.1	Notch Filter	52
3.3.2	Low Pass Filter	55
3.3.3	High Pass Filter	55
3.3.4	Gain Stages	56
3.3.5	Meter and Balance Circuits	56
3.4	Dual Voltage Controlled Oscillator Module	57
3.5	Pilot Tone/Mixer Module	58
3.6	Telemetry Link	58
3.7	Dual Demodulator Module	59
3.8	Power Stabilizer and Batteries	61

Chapter 4 DATA REDUCTION

4.1	Data Reduction	62
4.1.1	Frequency Analysis	62
4.1.2	Cross Spectra and Coherency, Cross Correlation	66
4.2	Determination of Tensor Elements	67
4.3	Practical Considerations	71
4.4	Implementation of Digital Frequency Analysis	73
4.5	Implementation of Analogue Frequency Analysis	76
4.5.1	Power Spectral Estimation	76
4.5.2	Phase Measurement	78
4.5.3	Effects of Noise on the Phasemeter	82
4.5.4	Phasemeter Tests	85

Chapter 5 TELLURIC TRAVERSES AT SOURTON TOR

5.1	Sourton Tor Test Site	87
5.2	Analogue Measurements	88
5.3	Digital Analysis	96

Chapter 6 MODELLING AND INTERPRETATION

6.1	Modelling and Interpretation	105
6.2	Two-Dimensional Models	109
6.2.1	The Finite Difference Method	110
6.2.2	Finite Difference Computer Programs	112
6.2.3	Three-Dimensional Models	113
6.3	Interpretation of Sourton Tor Results	113

Chapter 7 CONCLUSIONS AND SUGGESTIONS FOR FURTHER WORK

7.1	Summary	119
7.2	Future Developments	120

Appendix A ADJUSTMENT, OPERATION AND CIRCUITRY OF EQUIPMENT

A.1	General Notes on Operation and Adjustment	122
A.2.1	Main Amplifier Notch Filter	123
A.2.2	Low Pass Filter	124
A.2.3	High Pass Filter	124
A.2.4	AC Meter Zero Adjustment	125
A.2.5	Gain Setting	125
A.3	Dual V.C.O. Module	125
A.4	Pilot Tone and Mixer Module	126
A.5	Telemetry Transmitter and Receiver	126
A.6.1	Dual Demodulator Module, Bandpass Filters	127
A.6.2	Pulse Width and Offset Adjustment	128
A.7	Dual RMS Meter	129
A.8.1	Filter/Phasemeter	130
A.8.2	Phasemeter Adjustments	130
A.8.3	Filter Adjustments	131
A.9	Electric Preamplifier	132
A.9.1	D.C. Balance Adjustment	132
A.10	Magnetometer Preamplifier	133
A.11	Power Stabilizer Module	133
A.12	Timer Module and U.V. Recorder Interfacing	133

Appendix B COMPUTER MODELLING OF ELECTRICAL CONDUCTIVITY STRUCTURES 155

LIST OF REFERENCES 163

LIST OF ILLUSTRATIONS

1/1	Coordinate axes for source over uniform half space	9
1/2	H components at the i^{th} boundary in a multilayer case	9
1/3	Telluric system over a two dimensional configuration	20
2/1	The Geomagnetic amplitude spectrum	27
2/2	Flow chart of Magnetotelluric measurement, showing noise	27
2/3	Equivalent circuit of an induction magnetometer	34
2/4	Construction of Magnetometer	34
2/5	Constructional details of Magnetometer	35
2/6	Magnetometer frequency response	38
2/7	Electric preamplifier frequency response	38
2/8	Equivalent circuit for electric field pickup	39
2/9	Electric preamplifier schematic diagram	39
2/10	Absolute calibration of magnetometer	46
2/11	Relative calibration electric/magnetic	46
3/1	Carrier frequencies for FM recording and telemetry	48
3/2	Block diagram of field recording and telemetry system	49
3/3	Station A, rack and modules	50
3/4	A main amplifier module	50
3/5	Plug-in modules and their functions	51
3/6	Station B. rack and modules	53
3/7	Station B rack a) 4 channel configuration b) 6 channel configuration	53 53
3/8	Main amplifier block diagram	54
3/9	Main amplifier frequency response and specifications	54
3/10	Dual demodulator block diagram	60

4/1	Some functions and Fourier transforms	65
4/2	a) Telluric tensor equations for diagonal elements	69
	b) Telluric tensor equations for off-diagonal elements	70
4/3	F.M. tape replay. Schematic diagram	75
4/4	Digitized traces and power spectra for magnetotelluric data from Keel. Co. Longford (S. Ireland)	77
4/5	Block diagram of RMS meter and phasemeter modules	80
4/6	Phasemeter waveforms for sinusoidal inputs with delay τ	81
4/7	a) Phasemeter output against lag between sinewave inputs of period t	81
	b) Normalized correlation function for sinewaves of period t	81
4/8	Difference between zero and π shifted phasemeter readings for correlated random inputs	86
4/9	Difference between zero and π shifted phasemeter readings for noisy correlated random inputs	86
5/1	The area around Sourton Tor triangulation point showing geology and traverse lines	89
5/2	Electrode configuration	89
5/3	Sketched section through line A12, looking SW, showing IGS boreholes St-1, 2a, 2b, 3	90
5/4	8Hz amplitude ratios measured in the field	90
5/5	Line A12 Amplitude ratio NW component	92
5/6	Line A12 Amplitude ratio SW component	93
5/7	Line A12 Phase NW components	94
5/8	Line A12 Phase SW components	95
5/9	Digitized section of recording at Station 7	98
5/10	Digitized section of recording at Station 12	98
5/11	Station 7 Power spectral densities	99
5/12	Station 7 Cross Phase spectra	100
5/13	Station 12 Power spectral densities	101
5/14	Station 12 Cross Phase spectra	102

5/15 Printout for Station 12 digitized section 103
5/16 Telluric tensor printout, line A12, Station 9 104
6/1 One dimensional model fitted to magneto-telluric data from Ireland 107
6/2 One dimensional model fitted to magneto-telluric data from Ireland 108
6/3 Resistivity and I.P. (100' collinear dipoles) compared with telluric traverse 116
6/4 Horizontal coplanar loop EM results (440Hz real part) from Sourton Tor 116
6/5 Two dimensional Model for line A12, Sourton Tor 117
6/6 Model results, compared with field results, Line A12, Ev/Ey, 32Hz 118

Appendix A

A/1 Main Frame Wiring, Station A 135
A/2 Main Frame Wiring, Station B 136
A/3 Main Amplifier module, notch and low pass filters 137
A/4 Main Amplifier module, high pass filter and gain stages 138
A/5 Main Amplifier module, control layout 139
A/6 Main Amplifier module, high pass filter step response 139
A/7 Dual V.C.O. module circuit 140
A/8 V.C.O. frequency settings 141
A/9 Dual V.C.O. module, control layout 141
A/10 Pilot tone/mixer module circuit 142
A/11 Pilot tone/mixer module, control layout 143
A/12 Receiver output buffer circuit 143
A/13 Dual demodulator module circuit 144
A/14 Dual demodulator module, control layout 145
A/15 Dual demodulator settings 145

A/16 Dual RMS meter module and meter box circuits 146
A/17 Dual RMS meter module, control layout 147
A/18 Filter/Phasemeter module, control layout 147
A/19 Filter/Phasemeter module circuit 148
A/20 Electric Field Preamplifier circuit 149
A/21 Electric Field Preamplifier Layout 150
A/22 Magnetometer Preamplifier Layout 150
A/23 Magnetometer Preamplifier circuit 151
A/24 Power Stabilizer module, control layout 151
A/25 Power Stabilizer module and battery module circuits 152
A/26 Battery Module Layout 153
A/27 Timer Module, control layout 153
A/28 Timer Module circuit, Lennartz demodulator/ U.V. recorder interface circuit 154

Appendix B

Table 1 159
Table 2 160
Figure 1 161

ACKNOWLEDGEMENTS

I gratefully acknowledge the assistance of the following, during the preparation of this thesis:

Dr. A.R. Barringer, who created the project and organized its financial backing.
Mr. Keith Beer, of I.G.S., who provided information about the Sourton Tor test site.
My contemporaries at the Geophysics section of the Royal School of Mines for many discussions.
Mr. Ron Matthews for his help with equipment construction and field work.
My parents for their continued support.
Mr. Geoff Ricketts for counsel about electronics.
Rio Tinto Zinc Corporation Ltd., who provided 3 years' finance for field work and equipment.
The Royal Dutch Shell Co. Ltd., who provided a research bursary for 3 years.
Dr. Hans Tammemagi, for his painstaking reading of the thesis drafts and for his encouragement and constructive criticism.
Dr. Anna Thomas-Betts, for her comments on the early part of the tract.
Miss Judy Vertue, for her expert typing and invaluable help with proof reading.
Mr. Jim Wheildon, my supervisor, for administration.

C.J.M. Hewlett

October 1973

ABSTRACT

This thesis describes the design, construction and operation of new portable field equipment for telluric and magnetotelluric measurements. The frequency range covered is from about 0.1 to 100Hz, higher than is customarily used in conventional magnetotelluric and telluric surveys.

The equipment includes a six channel FM tape recording system, with input filters and amplifiers. A radio telemetry system enables two of the amplifier channels to be remote from the recorder for telluric measurements. Analogue circuitry for measuring amplitude and phase in the field is also incorporated.

Measurements were made with the equipment over a highly conducting zone at Sourton Tor, on the edge of the Dartmoor Granite in S.W. England. The results are in good agreement with those obtained by other electrical methods. The behaviour of natural electromagnetic fields over conducting structures is discussed, and a "telluric tensor" is defined, by analogy with the magnetotelluric impedance tensor. Numerical techniques for data reduction and interpretation are reviewed, and applied to the Sourton data.

It is concluded that the methods and equipment described above provide a useful supplement to the existing tools of the exploration geophysicist.

INTRODUCTION

Just over 100 years ago, at the Greenwich Observatory, Astronomer Royal George Airy commented "I alluded in my last report to the possible establishment of galvanic wires which would record, perhaps upon the same photographic sheet which bears the declination and horizontal force, the magnitude and direction of earth currents in two directions. I conceive that this may be justly regarded as an important physical experiment ..." (Airy, 1861). This is one of the earliest references to simultaneous measurements of Geomagnetic variations and Earth currents. However, few quantitative observations were made about their relationships for almost another 50 years. In 1908, W. van Bemmelen reported a correspondence between orthogonal horizontal magnetic and electric field variations in Java. He also noted that the relative amplitudes of the oscillations changed with period and that the magnitude of the horizontal electric field depended on the local ground conductivity. This fact was subsequently used by Conrad Schlumberger (1921) as the basis for the telluric current method of prospecting (Latin Tellus, Earth). It was not until 1953 that Louis Cagniard provided the theoretical basis of "Magnetotellurics", a word coined by him to describe methods of using natural magnetic and electric field oscillations for investigating electrical conductivity variations beneath the earth's surface (Cagniard, 1953).

The depth penetration achieved by magnetotelluric or telluric studies depends on the period of the electromagnetic variations used and on the subsurface conductivities. Usable oscillations occur over a period range of several decades and the depth of investigation over land varies correspondingly from a few metres to tens of kilometres. Magnetotellurics has obvious applications, not only as a tool for

studies of the Earth's crust and upper mantle and for the investigation of sedimentary basins in oil exploration, but also for mineral prospecting. Measurement of oscillations with periods of up to about 10^4 seconds may be required in the first case, and down to about .001 seconds in the last.

In crust and upper mantle investigations, and in petroleum exploration, magnetotellurics has been used to supplement the sometimes scanty information available from other sources. Its use at the smaller depth penetrations required in mineral and ground water exploration has been more restricted, primarily because of the availability of other efficient geophysical and geochemical techniques. The main disadvantage of the magnetotelluric and telluric methods lies in the random nature of the source field; relatively elaborate data processing is required which delays the results of surveys and pushes up costs. Some of the advantages are as follows:

a) Free, naturally occurring source field - low power requirements.
b) Excellent depth penetration.
c) Electrical "soundings" and determinations of strike direction can be made from a single station measurement.

Although numerous papers have been written about the theory of magnetotellurics, the number of published case histories is small. This is particularly true of the higher frequencies useful in mineral prospecting, probably because of a lack of suitable equipment. One of the chief aims of this project was to build apparatus to be used for assessing the practicability of the various ways in which Extremely Low Frequency (E.L.F.) natural fields can be used for mineral prospecting. A novel feature of the resulting

field equipment is the telemetry system, which enables signals from two widely separated locations to be recorded or analyzed in "real time" at one station. In many geological situations, much information can be obtained by measuring only two components of the magnetotelluric field. The equipment allows the validity of such simplifications to be assessed by recording up to six data channels at a time. Also included are facilities for simple analogue two channel phase and amplitude measurements. The condensed guide below gives a rough indication of the topics covered by each chapter of the thesis and picks out features of particular interest.

Chapter 1	Magnetotelluric Theory - the telluric tensor.
Chapter 2	Fields and their measurement - magnetometer design.
Chapter 3	The field equipment - telemetry system.
Chapter 4	Data reduction - analogue phasemeter.
Chapter 5	Field work - traverse over good conductor.
Chapter 6	Modelling - 2-D model.
Chapter 7	Conclusions and suggestions for further work
Appendix A	Details of Equipment, setting up and circuits.
Appendix B	Corrections to a published 2-D modelling program.

CHAPTER 1

MAGNETOTELLURIC AND TELLURIC THEORY

1.1 Units, coordinate systems, symbols and abbreviations

Unless otherwise stated, an m.k.s. system of units is used throughout the text. Cartesian coordinate systems have axes x (North), y (East) and ż (down). If an additional coordinate system is required, as in measurements involving a base and roving station, the roving axes are u (North), v (East) and w (down). Additional rotated coordinate systems will usually be indicated by primes, e.g. x', y', z'.

Vectors are indicated by underlining : $\underline{E}$
Components of vectors by subscripts : Ex
Matrices are indicated thus : $\underline{\underline{A}}$

Other notation is introduced in the text, as it occurs.

Abbreviations :

A.C. alternating current
D.C. direct current
E.L.F. Extremely Low Frequency. By definition, 30-300Hz but commonly used to describe frequencies down to 1Hz
e.m.f. electromotive force
F.E.T. Field Effect Transistor
F.M. Frequency Modulated
I.C. Integrated Circuit
I.G.S. Institute of Geological Sciences
I.P. Induced Polarization
I/P input
O/P output

Q Quality factor of a resonant system, defined as (resonant frequency)/(Bandwith between half power points of frequency response)

R.M.S. root mean square

S.P. Self Potential

T.E. Transverse Electric. Refers to an electromagnetic wave which has no electric field component in the direction of propagation

T.M. Transverse Magnetic. Refers to an electromagnetic wave which has no magnetic field component in the direction of propagation

U.V. Ultra-Violet, as in U.V. recorder, an oscillograph using ultra-violet sensitive paper.

V.C.O. Voltage controlled oscillator

V.L.F. Very low frequency. 300 - 30,000Hz

1.2. Solution of Maxwell's Equations

Maxwell's equations are the starting point for theoretical investigations of magnetotelluric fields. They are :

$$\text{div } \underline{D} = p \quad \text{Gausses theorem in electrostatics} \qquad 1:1$$

$$\text{div } \underline{B} = 0 \quad \text{Gausses theorem in magnetostatics} \qquad 1:2$$

$$\text{curl } \underline{E} = -\frac{\partial \underline{B}}{\partial t} \quad \text{Faraday's and Lenz's Law} \qquad 1:3$$

$$\text{curl } \underline{H} = \underline{J} + \frac{\partial \underline{D}}{\partial t} \quad \text{Ampère's Law} \qquad 1:4$$

where

$\underline{B}$ = Magnetic induction vector (tesla)

$\underline{D}$ = Electric displacement vector (Coulomb/metre^2)

$\underline{E}$ = Electric field Intensity vector (volt/metre)

$\underline{H}$ = Magnetic field Intensity vector (amp/metre)

$\underline{J}$ = Current density vector (amp/metre^2)

p = free charge density (Coulomb/metre^3)

t = time (secs)

In addition we define :

$\underline{D} = \epsilon \underline{E}$; ϵ = permittivity (Farad/metre)
$\underline{B} = \mu \underline{H}$; μ = permeability (Henry/metre)
$\underline{J} = \sigma \underline{E}$; σ = conductivity (mho/metre) 1:5

ϵ, μ and σ represent the physical properties of the medium in which the fields propagate; for air, $\sigma = 0$, $\mu = \mu_0$ and $\epsilon = \epsilon_0$ to a good approximation, where μ_0 = permeability of free space = $4\pi \times 10^{-7}$ H/m
ϵ_0 = permittivity of free space = 8.85×10^{-12} F/m

For most rocks and minerals, $\mu \simeq \mu_0$, but in some cases μ may be as large as $1.25\,\mu_0$ (some sulphide ores) or even $5\,\mu_0$ (massive magnetite). ϵ generally lies between ϵ_0 and $81\,\epsilon_0$, according to the water content of the medium. (The relative permittivity of water is 81.). In the derivations which follow, it is assumed that μ everywhere has the free space value μ_0.

Equation 1:1 can be rewritten

$$\text{div}(\epsilon \underline{E}) = 0 \qquad 1:6$$

The current density in a conducting medium is not generally zero. Conservation of charge implies that for a given volume

$$\frac{\partial p}{\partial t} + \text{div}\,\underline{J} = 0 \qquad 1:7$$

hence

$$\text{div}(\sigma \underline{E}) = \text{div}\,\underline{J} = 0 \qquad 1:8$$

if ϵ and σ are independent of position and orientation, equations 1:6 and 1:8 both give

$$\text{div}\,\underline{E} = 0 \qquad 1:9$$

and from 1:2, 1:3 and 1:4,

$$\text{div}\,\underline{H} = 0 \qquad 1:10$$

$$\text{curl } \underline{E} = -\mu \frac{\partial \underline{H}}{\partial t} \qquad 1:11$$

$$\text{curl } \underline{H} = \sigma \underline{E} + \epsilon \frac{\partial \underline{E}}{\partial t} \qquad 1:12$$

taking the curl of both sides of 1:11 gives

$$\text{curl (curl } \underline{E}) = -\mu \text{curl } \frac{\partial \underline{H}}{\partial t} \qquad 1:13$$

and differentiating 1:12 with respect to time,

$$\text{curl } \frac{\partial \underline{H}}{\partial t} = \sigma \frac{\partial \underline{E}}{\partial t} + \epsilon \frac{\partial^2 \underline{E}}{\partial t^2} \qquad 1:14$$

combining 1:13 and 1:14 to eliminate $\underline{H}$ and using the vector identity,

$$\text{curl (curl } \underline{E}) = \text{grad (div } \underline{E}) - \nabla^2 \underline{E}$$

We find, since div $\underline{E} = 0$ from equation 1:9,

$$\nabla^2 \underline{E} = \sigma\mu \frac{\partial \underline{E}}{\partial t} + \epsilon\mu \frac{\partial^2 \underline{E}}{\partial t^2} \qquad 1:15$$

1:15 is the well known "Equation of Telegraphy". The second term on the right hand side arises from the displacement current $\partial \underline{D}/\partial t$ in 1:4 and the first from $\underline{J}$, the conduction current. For an oscillating field of frequency, ω, $\underline{E}$ is proportional to e^{jwt} and the ratio of these two terms is therefore $-\omega\epsilon/\sigma j$. With the range of values for ϵ and σ given above and with $\omega < 100\pi$ radian/sec the displacement term is a factor of approximately 10^5 less than the conduction term and may justifiably be neglected. Equation 1:15 then becomes the diffusion equation

$$\nabla^2 \underline{E} = j\omega\sigma\mu\underline{E} \qquad 1:16$$

The equation for $\underline{H}$ can be derived similarly :

$$\nabla^2 \underline{H} = j\omega\sigma\mu\underline{H} \qquad 1:17$$

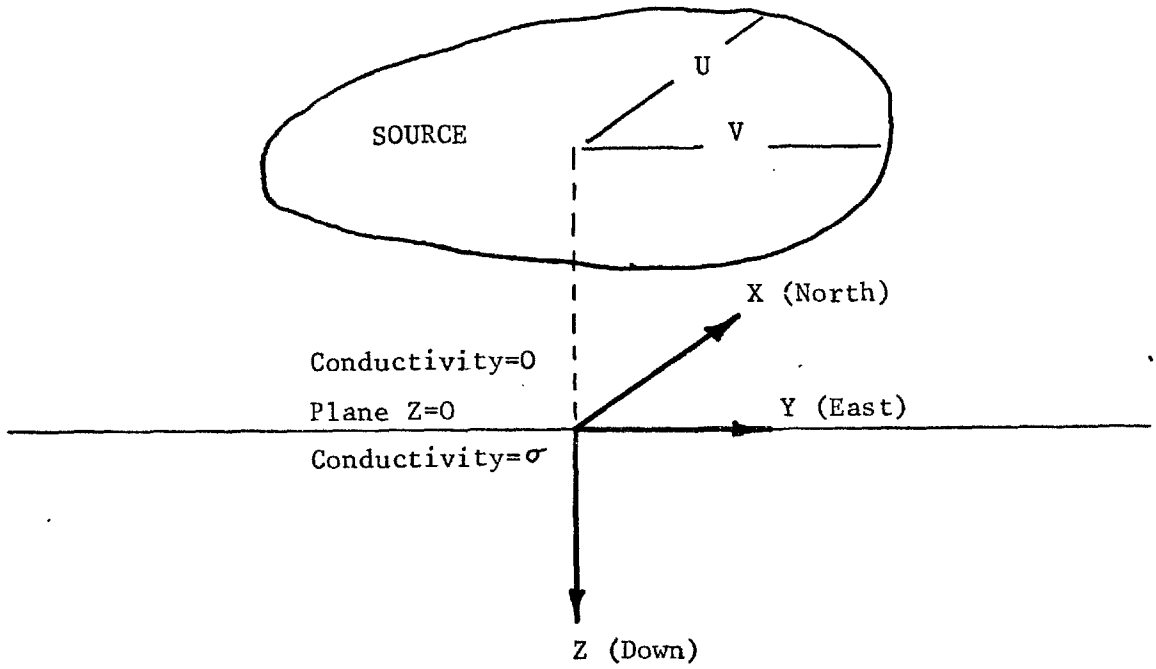


Figure 1/1 Coordinate axes for source over a uniform half space

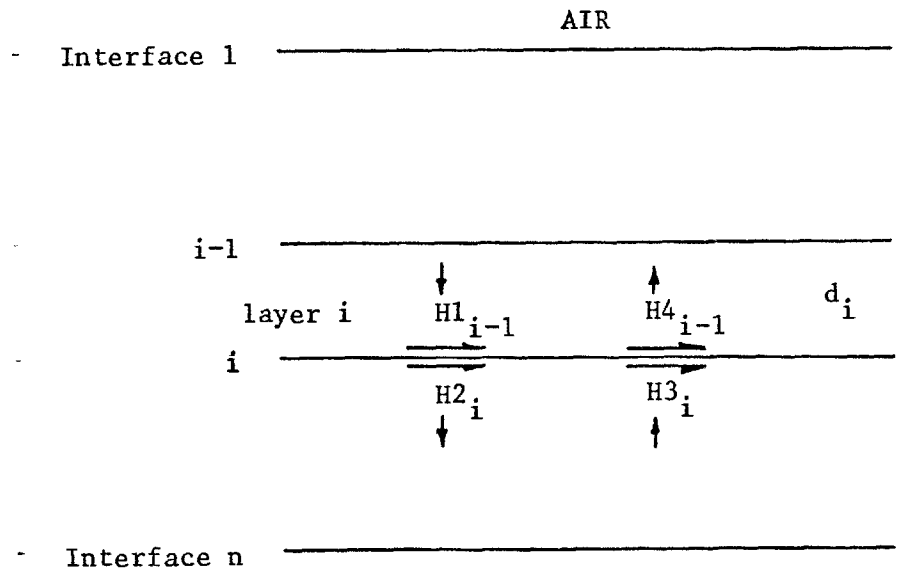


Figure 1/2 H components at the i^{th} interface in a multilayer case

1.3 Solution of the Scalar Diffusion Equation

There exist solutions of equations 1:16 and 1:17 which are the product of several functions, each of which depends only on one variable. These solutions are not general and can only be used if the boundary conditions satisfy certain conditions of symmetry and homogeneity. (Hopf, 1948, p 84). The equations separate into scalar equations of the type

$$\nabla^2 a = j\omega\sigma\mu a \qquad 1:18$$

where a is Ex, Ey, Ez, Hx, Hy or Hz. We try a solution a = XYZ, where X is a function of x alone, Y is a function of y alone and Z is a function of z alone :

$$\frac{1}{X}\frac{d^2X}{dx^2} + \frac{1}{Y}\frac{d^2Y}{dy^2} + \frac{1}{Z}\frac{d^2Z}{dz^2} = c^2 \qquad 1:19$$

where $c^2 = j\omega\mu\sigma$. We can therefore write

$$\frac{d^2X}{dx^2} = -p^2X, \quad \frac{d^2Y}{dy^2} = -q^2Y \text{ and } \quad \frac{d^2Z}{dz^2} = -r^2Z \qquad 1:20$$

provided $p^2 + q^2 + r^2 = -c^2$, where p, q and r are real or complex constants to be determined by boundary conditions. The elementary solution of 1:18 is thus of the form

$$a = Ae^{\pm j(px+qy+rz)} \qquad 1:21$$

where A is a constant for each particular solution, which comprises sums, for different values of A, of harmonic or exponential functions according to whether p, q and r are real or complex. Consider now the form of solution applicable to the situation of an "electric" or "magnetic" source over a uniform conducting half space (see Fig 1/1). For a quasi-static electric source, the tangential electric field just inside the conductor is zero if displacement

currents are neglected. The normal component is also zero inside the conductor because no current can flow across the boundary, although a normal electric field can exist above the boundary if there is a surface charge distribution. There is, therefore, a negligible field inside the conductor due to an electric source.

A simple consideration of the boundary conditions appropriate to the situation depicted in Fig 1/1 allows certain solutions of 1:18 to be rejected. Exponential solutions in the x and y directions can be excluded to avoid infinite fields as x and y tend to ∞, as can positive exponential solutions in the Z direction for similar reasons. Putting $r^2 = -(p^2 + q^2 + c^2)$, the solution inside the conductor therefore consists only of terms of the type

$$a = A \begin{matrix}\sin \\ \cos\end{matrix} px \begin{matrix}\sin \\ \cos\end{matrix} qy \; e^{(p^2+q^2+c^2)^{1/2}z} \qquad 1:22$$

where $\begin{matrix}\sin \\ \cos\end{matrix}$ means "sin or cos"

The function representing the shape of the source, f(x,y), can be written as a Fourier series of the type

$$f(x,y) = \sum_{m=0}^{\infty}\sum_{l=0}^{\infty} b_{lm} \begin{matrix}\sin \\ \cos\end{matrix} \frac{l\pi x}{U} \begin{matrix}\sin \\ \cos\end{matrix} \frac{m\pi y}{V} \qquad 1:23$$

where U and V are constants characterizing the dimensions of the source, l and m are integers and b_{lm} is a constant coefficient. Solutions are then restricted by boundary conditions to terms of the type given in 1:22 with $p = l\pi/U$ and $q = m\pi/V$. If the source varies slowly with x and y, the coefficient b_{lm} becomes negligibly small when l and m are increased above certain limits L and M. The maximum values of p and q which contribute appreciably to the solution are then given by $p = L\pi/U$ and

$q = M\pi/V$, which may be thought of as representing the wave numbers of the shortest wavelength spatial variations of the source.

For x and y constant, 1:22 reduces to

$$a = Ae^{cz} \qquad 1:24$$

$$\text{for } c \gg p^2 + q^2 \qquad 1:25$$

where A is a new constant and p and q have their maximum values. Equation 1:25 is the criterion for the minimum permissible source dimensions which allow solutions of the type 1:24 to be used. If this criterion is satisfied, we may write for the component Hx

$$Hx = Be^{(j\omega\mu\sigma)^{1/2}z} e^{j\omega t} \qquad 1:26$$

where B is a constant and the $e^{j\omega t}$ time dependency of the field has been reinserted.

Unless otherwise stated, in future calculations the above conditions will be assumed to apply so that the propagation constant is equal to c. The problem of source dimensions is discussed in detail in Wait (1962) and Srivastava (1965).

1.4 The Apparent Resistivity and skin depth

The wave impedance at the surface of the model in Fig 1/1 is defined by

$$Z = E/H \qquad 1:27$$

Z, the wave impedance, is independent of azimuth and position on the surface provided the source dimensions are large. E and H are any pair of orthogonal components in the xy plane. From equation 1:11, with partial derivatives with respect to x and y

zero, $$\frac{\partial E_y}{\partial z} = \mu \frac{\partial H_x}{\partial t}$$

hence $$Z = \left(\frac{j\omega\mu}{\sigma}\right)^{1/2} = \frac{j\omega\mu}{c} \qquad 1:28$$

or since $c = (j\omega\mu\sigma)^{1/2}$

$$\sigma = \omega\mu\left(\frac{H_x}{E_y}\right)^2 \qquad 1:29$$

This reduces to the well known Cagniard formula

$$\rho = 0.2T\left(\frac{E}{H}\right)^2 \qquad 1:30$$

where E and H are any orthogonal components in the plane $z = 0$, and are measured in microvolt/metre and nanoteslas (gammas) respectively. T is the period in seconds, ρ is the resistivity of the half-space and is equal to $1/\sigma$. If a resistivity ρ_a is calculated from orthogonal components of $\underline{E}$ and $\underline{H}$ at a point on the surface of a half space containing arbitrary conductivity variations, ρ_a is known as the "apparent resistivity" of the half space at that point.

The "Skin Depth" δ for a medium of conductivity σ is defined as the distance over which the amplitude of a propagating electromagnetic wave is attenuated by a factor e. From 1:24 this occurs with $z = 1/c$ so that

$$\delta = \left|(j\omega\mu\sigma)^{-1/2}\right| = \sqrt{\frac{2}{\omega\mu\sigma}} \qquad 1:31$$

The source dimension criterion 1:25 becomes

$$\delta \ll (p^2+q^2)^{-1/2} \qquad 1:32$$

implying that the skin depth must be small compared with the dimensions of lateral variations in the source.

The "wave impedance" Z should not be confused with the "characteristic impedance" Z_1, of a medium with propagation constant c_1, defined by

$$Z = \frac{j\omega\mu}{c_1} \qquad 1:33$$

$Z = Z_1$ only in the case of a uniform isotropic space.

1.5 The Layered half space Model

Fig 1/2 depicts an arbitrary, horizontally layered half space, a more complex, but much more useful model than the uniform case. Consider the tangential magnetic field on the top surface of the i^{th} interface of an n layer model; the field can be imagined as a downward propagating part $H1_{i-1}$ from the layer above and an upward propagating part $H4_{i-1}$ from the layer below due to reflections from lower interfaces. Azimuthal symmetry and an $e^{j\omega t}$ time dependency are assumed. Just below the interface the corresponding fields are $H2_i$ and $H3_i$ so that application of the boundary condition for tangential continuity of H gives

$$H1_{i-1} + H4_{i-1} = H2_i + H3_i \qquad 1:34$$

If the characteristic impedances of the media above and below the interface are Z_{i-1} and Z_i, the continuity of the tangential components of the electric field gives, because $E = ZH$,

$$(H1_{i-1} - H4_{i-1})Z_{i-1} = (H2_i - H3_i)Z_i \qquad 1:35$$

The components of H above the interface may now be expressed individually in terms of those below by combining the above two equations to give

$$H4_{i-1} = \frac{H3_i(Z_i + Z_{i-1}) - H2_i(Z_i - Z_{i-1})}{2Z_{i-1}} \qquad 1:36$$

$$H1_{i-1} = \frac{H2_i(Z_i + Z_{i-1}) - H3_i(Z_i - Z_{i-1})}{2Z_{i-1}} \qquad 1:37$$

The wave impedance Za_i just below the i^{th} surface is given by the ratio of the electric and magnetic fields :

$$Za_i = Z_i\,(H2_i - H3_i)/(H2_i + H3_i) \qquad 1:38$$

Rearranging terms to obtain an expression for $H2_i$,

$$H2_i = H3_i\,(Za_i + Z_i)/(Z_i - Za_i) \qquad 1:39$$

Substituting 1:39 into 1:36 and 1:37 gives expressions for $H4_{i-1}$ and $H1_{i-1}$ in terms of $H3_i$

$$H1_{i-1} = \frac{H3_i\,A}{Z_{i-1}(Z_i - Za_i)}$$

$$H4_{i-1} = \frac{-H3_i\,B}{Z_{i-1}(Z_i - Za_i)} \qquad 1:40$$

where $A = (Z_i Za_i + Z_i Z_{i-1})$, $B = (Z_i Za_i - Z_i Z_{i-1})$ 1:41

The fields just below the $i-1^{th}$ interface can be calculated from those just above the i^{th} interface from the propagation constant c_{i-1},

$$H3_{i-1} = H4_{i-1} \exp(-c_{i-1} d_{i-1}) \qquad 1:42$$

$$H2_{i-1} = H1_{i-1} \exp(+c_{i-1} d_{i-1}) \qquad 1:43$$

where c_{i-1} can be calculated from Z_{i-1} and equation 1:28, and d_{i-1} is the distance between the $i-1^{th}$ and the i^{th} interfaces. The wave impedance Za_{i-1} just below the $i-1^{th}$ interface is calculated from an expression similar to 1:38

$$Za_{i-1} = Z_{i-1}(H2_{i-1} - H3_{i-1})/(H2_{i-1} + H3_{i-1}) \qquad 1:44$$

substituting in this equation for $H3_{i-1}$ and $H2_{i-1}$ from 1:42 and 1:43

$$Za_{i-1} = Z_{i-1}\left\{\frac{H1_{i-1}e^{c_{i-1}d_{i-1}} - H4_{i-1}e^{-c_{i-1}d_{i-1}}}{H1_{i-1}e^{c_{i-1}d_{i-1}} + H4_{i-1}e^{-c_{i-1}d_{i-1}}}\right\} \qquad 1:45$$

substituting for $H1_{i-1}$ and $H4_{i-1}$ from equations 1:41 and 1:40 gives an expression for Za_{i-1} in terms of Za_i, Z_{i-1}, Z_i and the thickness of layer $i-1$. After elimination of H3,

$$Za_{i-1} = Z_{i-1}\left\{\frac{Ae^{c_{i-1}d_{i-1}} + Be^{-c_{i-1}d_{i-1}}}{Ae^{c_{i-1}d_{i-1}} - Be^{-c_{i-1}d_{i-1}}}\right\} \qquad 1:46$$

where A and B are as in equation 1:41. Dividing top and bottom of 1:46 by $\sqrt{AB}$ and putting $\sqrt{A/B} = \exp(\ln\sqrt{A/B})$ we obtain the expression

$$Za_{i-1} = Z_{i-1}\left\{\frac{e^{(c_{i-1}d_{i-1} + \frac{1}{2}\ln(A/B))} + e^{(c_{i-1}d_{i-1} - \frac{1}{2}\ln(A/B))}}{e^{(c_{i-1}d_{i-1} + \frac{1}{2}\ln(A/B))} - e^{(c_{i-1}d_{i-1} - \frac{1}{2}\ln(A/B))}}\right\} \qquad 1:47$$

The hyperbolic cotangent $\coth(x)$ is given by

$$\coth(x) = \frac{e^{x} + e^{-x}}{e^{x} - e^{-x}}$$

hence

$$Za_{i-1} = Z_{i-1}\coth(c_{i-1}d_{i-1} + \tfrac{1}{2}\ln(A/B)) \qquad 1:48$$

Just below the bottom interface of an n layer model there is no reflected component $H3_n$ so that from 1:38, $Za_n = Z_n$. The wave impedance just below the ground surface for any number of layers can be derived from the recursion formula 1:48 and the expressions 1:41 for A and B. The apparent resistivity is obtained from 1:27 and 1:30

$$\rho_a = \frac{\omega\mu}{Za_1^2} \qquad 1:49$$

Curves of apparent resistivity against frequency for some two and three layer cases are shown in Keller and Frishknecht (1966, p 219). Computer programs, using 1:48 are easily realisable so that surface impedances can be calculated for large numbers of layers. Gradual changes in conductivity can be simulated by approximating them to many thin layers with small conductivity contrasts.

1.6 Lateral Conductivity Variations

A "two-dimensional case" is a situation in which σ can vary with x or y, and z. In a "three-dimensional case" σ can vary with all three space coordinates. Consider the form of solution for the two dimensional case in which σ is a function of y and z. Equations 1:10, 1:11 and 1:12 are still applicable, but 1:8 must be used instead of 1:9. With derivatives with respect to x set to zero and neglecting displacement currents, the equations in component form become:

$$\frac{\partial}{\partial y}(\sigma E_y) + \frac{\partial}{\partial z}(\sigma E_z) = 0 \qquad 1:50$$

$$\frac{\partial H_y}{\partial y} + \frac{\partial H_z}{\partial z} = 0 \qquad 1:51$$

$$\frac{\partial E_y}{\partial z} - \frac{\partial E_z}{\partial y} = \mu \frac{\partial H_x}{\partial t} \qquad 1:52$$

$$\frac{\partial E_x}{\partial z} = -\mu \frac{\partial H_y}{\partial t} \qquad 1:53$$

$$\frac{\partial E_x}{\partial y} = \mu \frac{\partial H_z}{\partial t} \qquad 1:54$$

$$\frac{\partial H_y}{\partial z} - \frac{\partial H_z}{\partial y} = -\sigma E_x \qquad 1:55$$

$$\frac{\partial H_x}{\partial z} = \sigma E_y \qquad 1:56$$

$$\frac{\partial H_x}{\partial y} = -\sigma E_z \qquad 1:57$$

Equations 1:50, 1:52, 1:56 and 1:57 contain only the components Hx, Ey and Ez, whereas 1:51, 1:53, 1:54 and 1:55 contain only Ex, Hy and Hz. The field thus propagates in two independent modes, called the transverse magnetic (TM or H - parallel) and the transverse electric (TE or E - parallel). Generally, the wave impedances for the two modes differ, i.e.

$$Z_{TM} = -\frac{E_y}{H_x} \qquad 1:58$$

$$Z_{TE} = \frac{E_x}{H_y} \qquad 1:59$$

If the electric field is measured at some arbitrary angle φ to the x - axis, it will be influenced by both the parallel and the perpendicular magnetic fields. This phenomenon is expressible in matrix form (Cantwell, 1960)

$$\begin{vmatrix} E'_x \\ E'_y \end{vmatrix} = \begin{vmatrix} Z'_{11} & Z'_{12} \\ Z'_{21} & Z'_{22} \end{vmatrix} \begin{vmatrix} H'_x \\ H'_y \end{vmatrix} \qquad 1:60$$

where primes indicate that the fields are measured along axes x', y' rotated at an angle φ to the x and y axes. The matrix $\tilde{Z}'$, given by

$$\tilde{E}' = \tilde{Z}'\tilde{H}' \qquad 1:61$$

is called the impedance tensor for the rotation angle φ. The fields along axes rotated by an angle θ to the measuring axes are given by

$$\tilde{E}'' = \tilde{P}\tilde{E}'$$

$$\tilde{H}'' = \tilde{P}\tilde{H}'$$

where $\tilde{P} = \begin{vmatrix} \cos\theta & \sin\theta \\ -\sin\theta & \cos\theta \end{vmatrix}$ 1:62

and $\tilde{Z}'' = \frac{\tilde{E}''}{\tilde{H}''}$

so that $\tilde{Z}'' = \tilde{P}\tilde{Z}\tilde{P}^T$ 1:63

where $\tilde{P}^T$ is the transpose of $\tilde{P}$.
When $\theta = -\varphi$, i.e. the rotation angle is such that the tensor is aligned along the x and y axes, the diagonal elements are zero, so that

$$\tilde{Z}''(\theta = -\varphi) = \begin{vmatrix} 0 & Z_{TE} \\ Z_{TM} & 0 \end{vmatrix} \quad 1:64$$

The directions parallel and normal to strike, the x and y axes in this case, are called the principal directions of anisotropy.

1-7 The Telluric Method

Lateral variations in conductivity can be delineated by measuring horizontal electric fields alone. The telluric method eliminates the difficulties sometimes encountered in measuring magnetic fields, but only allows relative conductivities to be calculated. If absolute values are needed, magnetotelluric measurements must be made at one of the telluric stations. Two sets of recording equipment are required, each with two channels for registering orthogonal components together with a means of synchronizing the two records. A typical arrangement is shown in Fig 1/3. One of the recording sets remains in the same position throughout the survey and is referred to as the "Base station"; the "Roving station" is moved so that comparisons may be made between the relative telluric field strengths in different parts of the survey area.

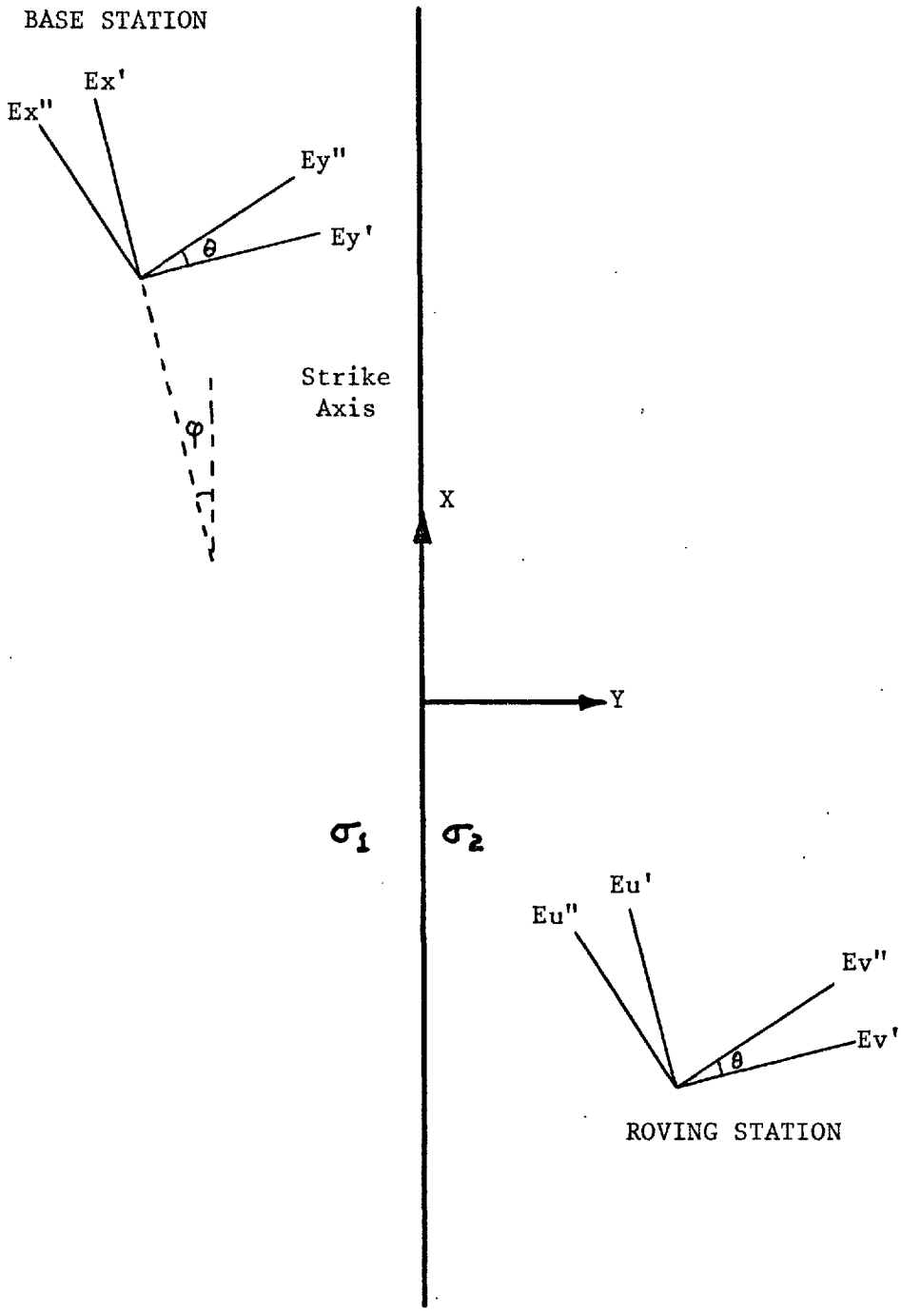


Figure 1/3 Telluric system over a two dimensional configuration

The electric fields at base and roving stations are connected to each other by the linear relation

$$\begin{vmatrix} E_u \\ E_v \end{vmatrix} = \begin{vmatrix} a & b \\ c & d \end{vmatrix} \begin{vmatrix} E_x \\ E_y \end{vmatrix} \qquad 1:65$$

It has long been recognized that the Jacobian of the transformation from the x-y system to the u-v system,

$$j = ad - bc \qquad 1:66$$

depends only on the electrical properties of the subsurface; it is called the relative ellipse area of the roving station with respect to the base station (see Berdichevskii 1960). Iso-j maps are recognised as containing much useful geological information. Traditionally, three assumptions are made in the analysis of telluric data

a) The geological situation approximates to a conducting layer overlying a resistive basement;
b) The conductivity contrast between the two layers is such that most of the current flows in the upper layer;
c) The electromagnetic field penetrates to the basement with little attenuation.

(Keller and Frischknecht, 1966, chapter 5)

If these assumptions hold, the telluric field is independent of frequency over a large range. Analysis then proceeds by the "triangle" or the "vectogram" method; these both involve the graphical calculation of j from strip charts or x-y charts of the electric field components (Yungul, 1968). The sophisticated data analysis techniques used in magnetotellurics do not appear to have been applied to the telluric method, possibly for economic reasons

(Yungul, 1968 and Yungul et al, 1973). The parallel between the two methods is, however, striking.

1.8 The Telluric Tensor

Fig 1/3 depicts two quarter spaces with conductivities σ_1 and σ_2, separated by a vertical interface striking along the x- axis, although the considerations that follow apply to any two-dimensional situation. Generally, the electric fields at roving and base station are related by

$$\begin{vmatrix} E'_u \\ E'_v \end{vmatrix} = \begin{vmatrix} A'_{11} & A'_{12} \\ A'_{21} & A'_{22} \end{vmatrix} \begin{vmatrix} E'_x \\ E'_y \end{vmatrix} \qquad 1:67$$

or in matrix form, with subscript $b \equiv$ base and $r \equiv$ roving.

$$\tilde{E}'_r = \tilde{A}' E'_b \qquad 1:68$$

The matrix $\tilde{A}'$ will be called the "telluric tensor" for a rotation angle φ with respect to the principal x and y axes. The tensor elements are complex numbers, which are functions of frequency, unlike the real constants in 1:65. The field components at an angle θ to the measuring axes are given by

$$\tilde{E}''_r = \tilde{P}\,\tilde{E}'_r \qquad 1:69$$

$$E''_b = \tilde{P}\,E'_b \qquad 1:70$$

where $\tilde{P}$ is as defined in 1:62
in addition,

$$E''_r = \tilde{A}''\,\tilde{E}''_b \qquad 1:71$$

manipulation of the four equations above gives the relationship

$$\tilde{A}'' = \tilde{P}\,\tilde{A}\,\tilde{P}^T \qquad 1:72$$

In component form equation 1:72 becomes

$$A''_{11} = A'_{11}\cos^2\theta + (A'_{12} + A'_{21})\sin\theta\cos\theta + A'_{22}\sin^2\theta \qquad 1:73$$

$$A''_{12} = A'_{12}\cos^2\theta + (A'_{22} - A'_{11})\sin\theta\cos\theta - A'_{21}\sin^2\theta \qquad 1:74$$

$$A''_{21} = A'_{21}\cos^2\theta + (A'_{22} - A'_{11})\sin\theta\cos\theta - A'_{12}\sin^2\theta \qquad 1:75$$

$$A''_{22} = A'_{22}\cos^2\theta - (A'_{12} + A'_{21})\sin\theta\cos\theta + A'_{11}\sin^2\theta \qquad 1:76$$

When $\theta = -\varphi$, the off-diagonal elements of the telluric tensor $\tilde{A}''$ are zero, because of the independence of the horizontal electric field components normal and parallel to the strike. (see equations 1:50 to 1:57). The principal directions of anisotropy can thus be found in practice by computational rotation of the measured tensor $\tilde{A}'$ until the absolute values of the off-diagonal elements are zero. Two necessary conditions are:

a) The line joining the base and roving stations must not be parallel to the strike.
b) The difference between the corresponding off-diagonal elements of the impedance tensors at the base and roving station must be large enough to overcome the errors involved in the measurements.

The second condition will not be satisfied if the base and roving stations are close together, and/or the degree of anisotropy is small.

Real situations are often encountered which are only approximately two-dimensional. In these cases, the off-diagonal tensor elements will pass only through minima (not zero) as the telluric tensor is rotated through the principal directions of anisotropy. In magnetotellurics a skew coefficient is defined in order to indicate whether a two dimensional interpretation is reasonable (Swift 1967).

$$\text{skew} = \frac{|Z_{11} + Z_{22}|}{|Z_{12} - Z_{21}|} \qquad 1:77$$

The skew is invariant under rotation and approaches zero for a one or two dimensional case. By analogy, we may define a telluric skew, such that

$$\text{telluric skew} = \frac{|A_{12} - A_{21}|}{|A_{11} + A_{22}|} \qquad 1:78$$

The principal value of the diagonal element of the telluric tensor normal to the strike, A22, is related simply to the principal impedance tensor elements Z_{TM} (base) and Z_{TM} (roving). The magnetic field parallel to strike at the surface is invariant (see 6.2.1.) so that from equation 1:58

$$\frac{Z_{TM}\,(\text{roving})}{Z_{TM}\,(\text{base})} = \frac{E_v}{E_y} = A_{22} \qquad 1:79$$

The relationship between All and Z_{TE} depends on the nature of the two dimensional structure, because the magnetic field normal to strike is not invariant.

CHAPTER 2

NATURAL FIELD MEASUREMENTS AND TRANSDUCERS

2.1 The Geomagnetic Spectrum

A typical geomagnetic amplitude spectrum is shown by the solid curve in Fig 2/1. The dotted lines indicate the approximate maximum and minimum amplitudes likely to be encountered in northern temperate latitudes. There is a distinct minimum in the amplitude near 1Hz; below this frequency most of the field variations or "micropulsations" are due to magnetohydrodynamic interactions between the main geomagnetic field and the solar particle flux. The main field is of internal origin, and its "secular magnetic variations" are only appreciable at periods too long to be of interest in induction studies. The onset of magnetic storms associated with sunspot activity can cause the mean amplitudes of micropulsations to increase by an order of magnitude or more with simultaneous enhancement of the average level in the VLF part of the spectrum. Micropulsation phenomena are not thought to occur above 20Hz (Vladimirov and Kleimenova, 1962).

Above about 3Hz most of the observed natural electromagnetic field is due to lightning induced guided waves travelling in the earth-ionosphere cavity (Wait, 1962, p 285), and V.L.F. emissions such as "whistlers" (Bleil 1964, p 171). In most parts of the spectrum the mean amplitude changes diurnally and seasonally as well as with latitude and with the onset of magnetic storms. In the 5 to 40Hz frequency band lightning flashes excite Schumann resonances in the spherical shell between the Earth and the ionosphere, with harmonics close to 8, 14, 20, 26, 32 ..... Hz (Schumann, 1954). The combination of continuous global thunderstorm activity with the insensitivity of the

resonances to diurnal variations in the ionosphere ensures a usable signal at virtually all times. (Keller and Frischknecht, 1966, p 204. Sparrow and Ney 1971). Above 40Hz the signal is less reliable, and at times is too small to allow reliable measurements to be made (Ward et al. 1958). The constancy of the Schumann background makes the 5-40Hz band particularly suitable for exploration systems.

2.2 Errors in natural field measurements

Extreme care is always necessary when making measurements of natural low frequency electromagnetic fields. The significance of some of the errors inherent in their detection, and in their use for conductivity determinations will now be considered.

A flow chart of the stages in a magnetotelluric measurement is shown in Fig 2/2. The aim is to find the ground response function G(f) as a function of the frequency f of a source field which is generally assumed to behave like a plane wave. The accuracy of any given estimate of G(f) depends on the precision to which the system response parameters are known, i.e. on the calibration from transducer input to analyser output. Variations in the value of G(f) obtained from several independent measurements can be due to a combination of accidental errors, system noise and external noise, as summarized in Fig 2/2. Accidental errors, such as the misreading of a scale or gross inaccuracy in the alignment of a magnetometer axis will not be considered here. System noise is usually only significant in the input stages of amplifier chains, and is closely connected with the design of the magnetic and electric field pick up devices. External noise is defined as any disturbance in the natural electromagnetic field which does not obey the criteria for source uniformity.

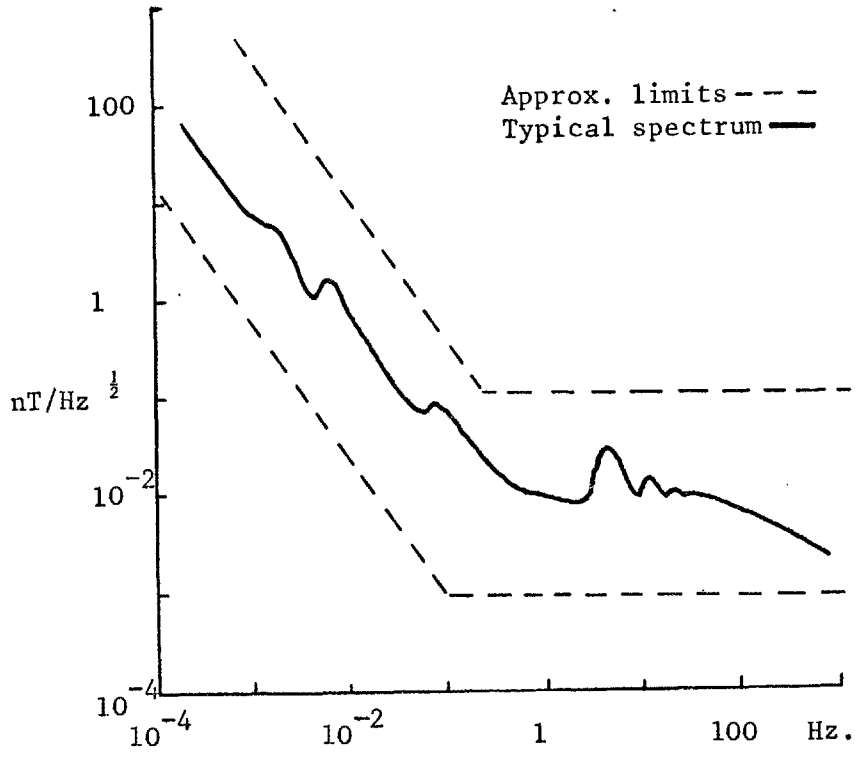


Figure 2/1 The Geomagnetic amplitude spectrum (after Sims and Bostick (1969), Chaize and Lavergne (1970))

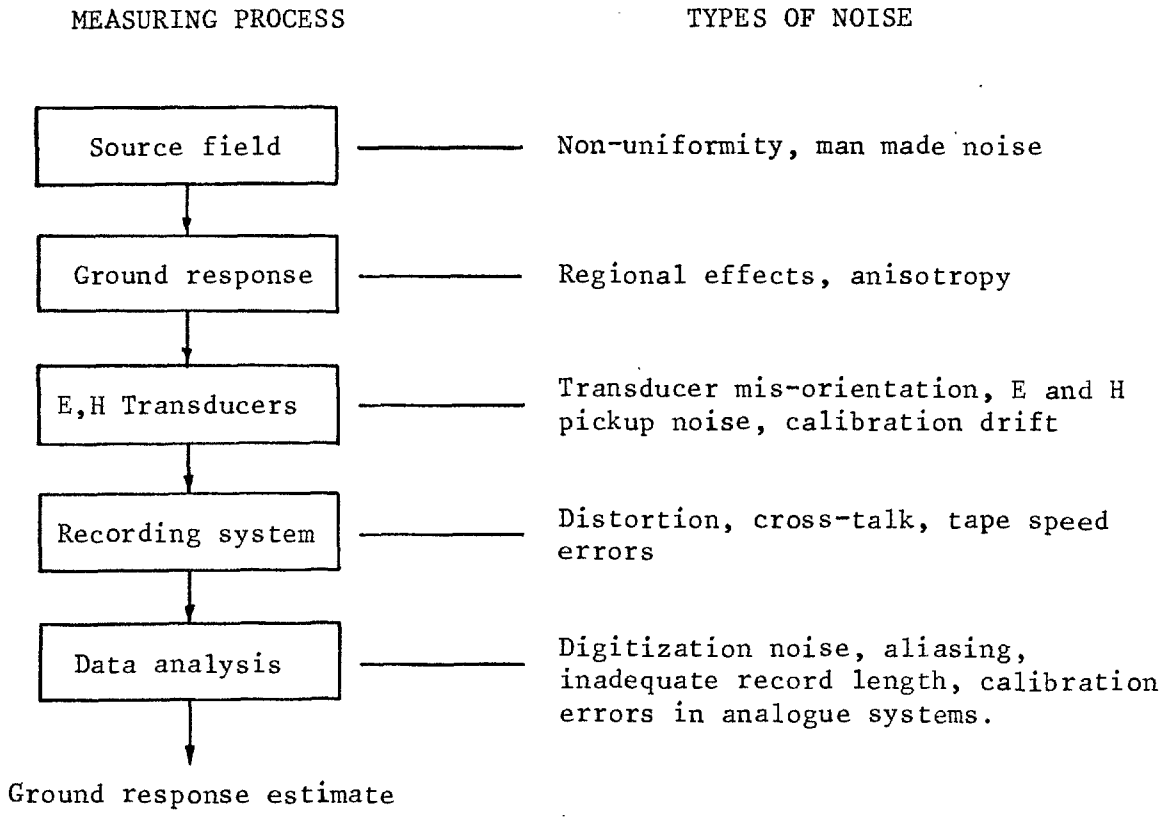


Figure 2/2 Flowchart of magnetotelluric measurement, showing noise

2.3 Uniformity of the Source Field

It was pointed out in Section 1.3 that a source could be considered uniform at a given frequency if the skin depth of the conducting medium below was considerably less than the wavelength of horizontal variations in the field. At 8Hz, for example, the skin depth in a medium of resistivity 10^4 Ohm-metres, the upper end of the range for rocks, is only about 18km, compared with a wavelength of 10,000km. The global nature of the Schumann resonances thus appears to guarantee that the source dimensions can be neglected, a view which is supported by the fact that records from magnetometers thousands of miles apart are often similar (Shand, 1966)

The corollary appears to be that the electromagnetic field behaves as a plane wave incident on a flat earth. This is not strictly true because the strength of the induced currents in a region is not determined solely by the inducing field and ground conductivity in the immediate neighbourhood, but depends on the nature and distribution of the entire inducing field and on the geometry and conductivity of a region of corresponding dimensions. (Forde, 1972, p 14). Several examples of source non-uniformity due to such large scale structures are discussed by Chaize and Lavergne (1970).

In the Schumann resonance band Llanwyn-Jones and Kemp (1970) have demonstrated that it is possible to deduce the azimuth and range of large lightning flashes from power spectral measurements of the radial electric field or tangential magnetic field at a single position. It is therefore possible, in principle, to correct for source non-uniformity in this frequency range, because the form of the source field can be calculated. Strictly speaking, only the radial electric field should be used for this

purpose, as the tangential magnetic field is affected by lateral conductivity variations.

Man made electrical disturbances are an important source of non-uniform fields at frequencies above 0.1Hz. The biggest effects are caused by power line transients, electric railways and harmonics and sub-harmonics of the AC power distribution frequency. Discussions of these effects are to be found in Chaize and Lavergne (1970), Slankis et al. (1972) and Klewe (1958). It is emphasised that measurements made near power lines, electric railways and industrialized areas should be treated with circumspection and examined carefully for signs of non-uniform, man made interference. Other sources of trouble are electric fences, corrosion protection circuits for pipelines, and radio stations.

2.4.1 Choice of magnetometers

Near 1Hz the geomagnetic field has a minimum amplitude approaching .001 nT. It is possible to measure fields of this order using suspended magnet systems (Roy 1963), superconducting quantum devices (Nisenoff 1969), fluxgate magnetometers (Scintrex Ltd., 1972) or induction coils. The first three were rejected on grounds of cost, complexity, inconvenience for field use, insensitivity at high frequencies or a combination of these factors. Induction coil magnetometers have the advantages of high sensitivity and low cost, combined with constructional simplicity and good high frequency response. Their main disadvantages are size and weight. Both can be reduced by using high permeability cores, but cross modulation caused by the inherent non linearity of ferromagnetic materials must be minimized by careful choice of core material.

Consider a coil of wire in which e.m.f.s are induced by flux changes in the core. The induced e.m.f. V is given by

$$V = -n\frac{d\varphi}{dt} \qquad 2:1$$

where n = number of turns in the coil

φ = flux through the coil

the flux φ is given by

$$\varphi = HA\mu_e \qquad 2:2$$

where H = magnetic field strength along coil axis

A = cross sectional area of core

μ_e = effective permeability of core

For an air cored coil $\mu_e = \mu_o$, but it can be much larger ($\mu_e \simeq 10^4 \mu_o$) for a ferromagnetic core. The effective permeability attained with material of true permeability μ in the form of a rod of length l and diameter r increases with l/r. Curves of the effective permeability at the centre of such a rod for different l/r ratios and μ values are given by Brailsford (1966, p 17). μ_e is a maximum at centre of a rod and falls off parabolically towards the ends for high μ values; for low μ, the fall off is sharper at the ends and less in the middle (Bozforth and Chapin, 1942).

High coil sensitivity can be obtained either by using a large diameter air cored coil or a small diameter coil on a long high permeability rod. The equivalent circuit of a coil with distributed capacitance C, self inductance L and resistance R is given in Fig 2/3. This is a reasonable approximation to a real coil and behaves as a tuned circuit with output voltage Vo given by

$$Vo = \frac{V}{j\omega C(R + j\omega L + 1/j\omega C)} \qquad 2:3$$

where $\omega = 2\pi f$ radians per sec

f = frequency

C is a function of the physical dimensions of the coil (see Terman, 1942, p 101). R is composed of the resistance of the winding, and a frequency dependent term due to the losses in the core. If an $e^{j\omega t}$ time dependency is assumed for the field H in equation 2:2, equation 2:1 becomes:

$$V = j\omega nHA\mu_e e^{j\omega t} \qquad 2:4$$

Combining 2:3 and 2:4 gives equation 2:5, the overall frequency response:

$$Vo = \frac{-Hk}{C(R+j\omega L+1/j\omega C)} \qquad 2:5$$

where $k = nA\mu_e e^{j\omega t}$

Vo is a maximum when $j\omega L = -1/j\omega C$, giving

$$\omega_{max} = 1/(LC)^{1/2} \qquad 2:6$$

where ω_{max} is the frequency for maximum output. Considerably above and below ω_{max},

$$Vo \triangleq -jHk\omega \qquad \omega \ll \omega_{max} \qquad 2:7$$

$$Vo \triangleq jHk/\omega LC \qquad \omega \gg \omega_{max} \qquad 2:8$$

In practice equation 2:8 does not hold at high frequencies for a coil with a high permeability core, because in reality μ is a complex quantity. The inductance L decreases and the core loss contribution to R increases rapidly towards high frequencies. The resulting loss of sensitivity can be reduced by using a core constructed of insulated laminations, thin compared with the skin depth of the core material at the highest frequency of interest.

2.4.2 Design Considerations for Induction Magnetometers

The resonant response of the induction coil makes frequency compensation desirable if a wide frequency range is to be covered. The perfect compensation network has a response which is the inverse of equation 2:5, but useful results can be obtained with much simpler networks. If the coil is operated at well below its resonant frequency (see equation 2:7) a simple first order low pass filter (equation 2:9) will give a flat response over a wide bandwith.

$$g(\omega) = 1/(1 + j\omega\tau) \qquad 2:9$$

where g(w) is the gain at frequency ω

τ is the time constant of the filter

Multiplying 2:7 by g(ω) defined in 2:9, we obtain

$$V_o = Hk/\tau \qquad \omega_{max} >> \omega >> 1/\tau$$

i.e. Vo is independent of frequency in the specified range.

Fig 2/3 shows an operational amplifier with feedback components C2 and R2 to give a time constant τ = R2 C2 but without the insertion loss implied by equation 2:9. In practice a buffer stage is necessary to prevent loading of the coil by R1.

2.4.3 Noise

The maximum sensitivity of a coil is limited by the Johnson noise developed in the impedance of the winding. Below the resonant frequency, the noise in the resistive part R of the impedance is dominant; the resistance of the winding should therefore be kept as low as possible (see equation 2:5). Small diameter coils with permeable cores meet this requirement best; they also have a significant size and weight advantage over air cored coils. Descriptions of the design of

air cored coils are given in Becker (1967) and Rankin and Burke(1972) and of permeable cored coils in Llanwyn-Jones and Kemp (1970), Jolivet (1969), Chaize and Lavergne (1970) and Vozoff (1972). A general discussion of both types can be found in Keller and Frischknecht (1966, p 236-238).

An important source of noise in induction magnetometers is wind induced motion of the coil, relative to the earth's static magnetic field. Such noise can be largely eliminated by burying the coil in a shallow trench, but this may be difficult or impossible with a large air cored coil. Slankis, et al. (1972) report that their air cored coils could only be used in very calm conditions. In the author's opinion it is best to use air cored coils for vertical field measurements, when the coil can be laid flat on the ground, and high permeability cored coils for horizontal field measurements. Experience has shown that the latter need not necessarily be buried provided they are shielded from wind and rain.

The preamplifier input noise decides the maximum sensitivity attainable with a given coil. It is usually inversely proportional to frequency below about 10Hz (1/f noise see Zepler and Punnet, 1963, Ch.7), whereas the output from the coil below resonance is directly proportional to frequency. Below a certain frequency ω_{min} the output of the coil for a maximum probable signal falls below the amplifier noise, and it is not worth trying to increase the amplifier gain any further at lower frequencies. The feedback circuit in Fig 2/3 automatically fulfills this requirement with a D.C. gain of R2/R1 , and a cutoff frequency ω_c given by

$$\omega_c = 1/R2C2$$

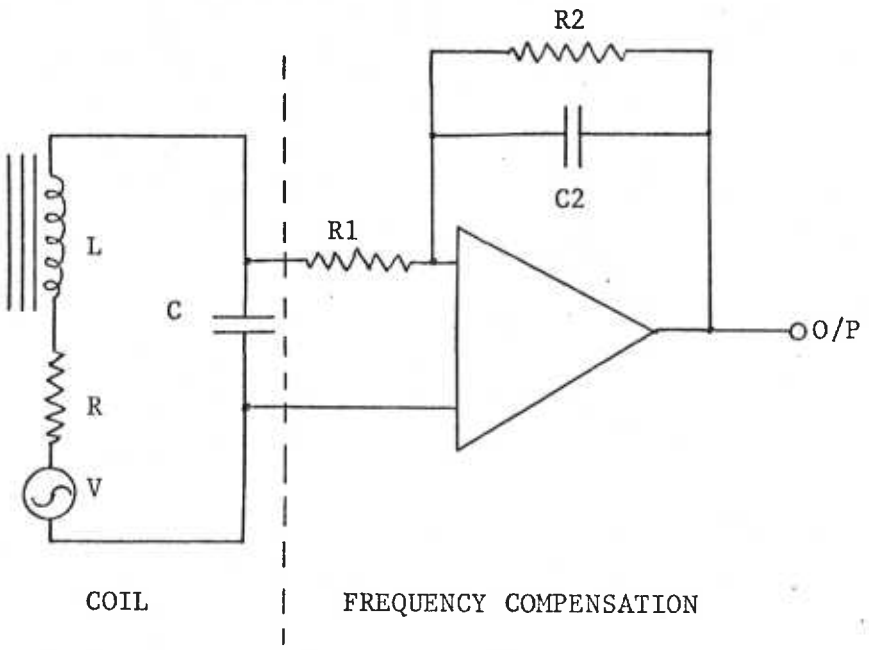


Figure 2/3 Equivalent circuit of an induction magnetometer

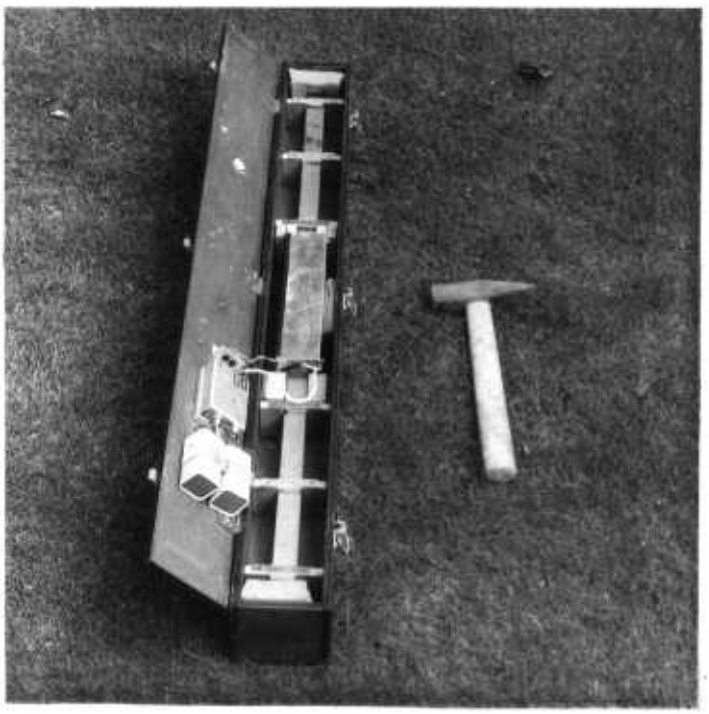


Figure 2/4 Construction of Magnetometer

2.4.4. The Magnetometer design

Constructional details of the final design are shown in Figs 2/4 and 2/5.

CORE:

Core material	Radiometal 50 (Telcon Metals Ltd)
Core length	1 m.
Core cross section	25 x 25 mm.
Laminations	60
Effective permeability	≐ 200

COIL:

No. of bobbins	up to 10
Turns per bobbin	17,000
outside diam.	50 mm.
Bobbin length	48 mm.
Wire	42 S.W.G.
Resistance per bobbin	3500 ohms
Calibration winding	20 turns

ELECTRICAL: (For a coil with 6 bobbins)

Resistance	21kohms
Capacitance	3800 pF
Inductance	300 H
Sensitivity at 8Hz	≐ 0.25 mV/nT/Hz
Resonant frequency	150Hz

Figure 2/5 Constructional details of Magnetometer

Preamplification and frequency compensation are performed by a single non-inverting feedback amplifier (circuit Fig A/23) which has a response given by equation 2:10 below. This circuit was chosen because it has a higher input impedance than the inverting configuration giving the response in equation 2:9.

$$g(\omega) = \frac{A_o(R_1+Z_2)}{Z_2+R_1(1+A_o)} \qquad 2:10$$

where Ao = open loop gain of Amplifier

$Z_2 = 1/(1 + j\omega C_2 R_2)$, feedback impedance

R1 = Input resistor value (see Fig A/23)

$g(\omega)$ = gain at angular frequency ω

If $A_0 \gg |Z_2/R_1|$ equation 2:10 simplifies to

$$g(\omega) \triangleq \frac{(R_1 + Z_2)}{R_1} \qquad 2:11$$

The right hand side of 2:5 is multiplied by $g(\omega)$ in 2:11 to obtain equation 2:12, the overall response, which is plotted in Fig 2/6 with component values.

$$V_{out} = \frac{-Hk(R_1+Z_2)}{R_1C(R+j\omega L+1/j\omega C)} \qquad 2:12$$

(The variation of μ_e with frequency is not taken into account as it is negligible below 50Hz for a Radiometal core). The uncompensated response, equation 2:5 (dashed curve) and the measured response (triangular symbols), corrected to the calculated level at 8Hz are also shown. The discrepancy at high frequencies is probably due to the fall off in $|\mu_e|$.

2.5.1 Horizontal Electric Field Pickup

The expected range of amplitudes of the horizontal electric field can be calculated by substituting maximum and minimum values for the amplitude of H, the frequency f and the ground resistivity ρ into equation 1:30

for H = .001 nT)
f = .1 Hz)E $\triangleq 2\times10^{-4}$ microvolt/m
= 3 mho/m.)

for H = .1 nT)
f = 100 Hz)E $\triangleq$ 200 microvolt/m
= .0001 mho/m)

These values are for extreme cases; in practice the range is about .02 to 20 microvolt/m in Northern temperate latitudes, on land.

Pickup of the electric field is accomplished by amplifying the potential difference which appears between two electrodes placed in the ground a distance X apart. If the component of the electric field along the line joining the two electrodes is Ex, the potential difference V between them is given by

$$V = \int_0^X Ex\,dx \qquad 2:13$$

Ex is usually assumed to be constant over the distance X to give a linear relationship between potential difference and electrode separation :

$$V = XEx \qquad 2:14$$

For this relationship to hold, a small separation X is necessary in regions where Ex varies rapidly with distance.

The equivalent circuit for a pair of grounded electrodes connected to a differential amplifier is shown in Fig 2/8. The signal V_S appears as a voltage generator in series with a source impedance Z_S and the signal pickup noise V_N. The amplifier has a differential input impedance Z_{IN} and the amplifier input noise is equivalent to a current generator, Ia and a voltage generator Va. A common mode voltage, Vcom, has also been included to represent the effects of other grounded equipment connected to the amplifier common terminal. Neglecting all noise generators, the signal voltage Vi across the amplifier input terminals is given by

$$Vi = \frac{V_S Z_{IN}}{Z_S + Z_{IN}}$$

$$\text{i.e. } Vi \simeq V_S \quad \text{if } Z_{IN} \gg Z_S \qquad 2:15$$

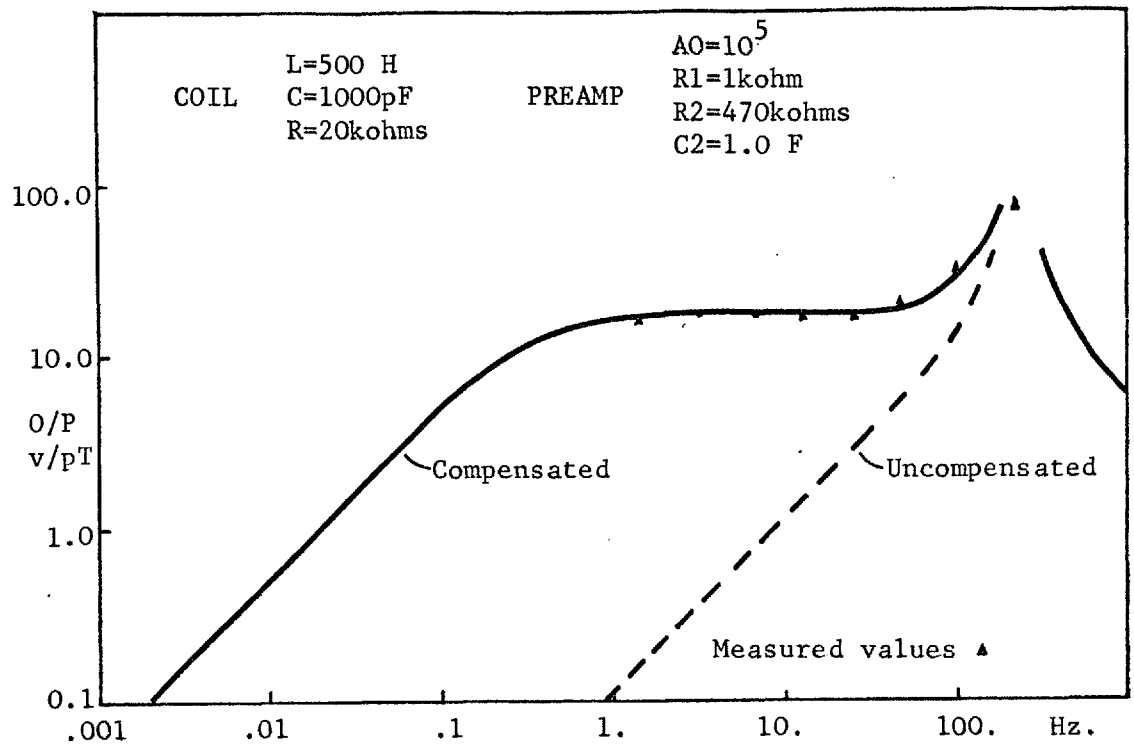


Figure 2/6 Magnetometer frequency response

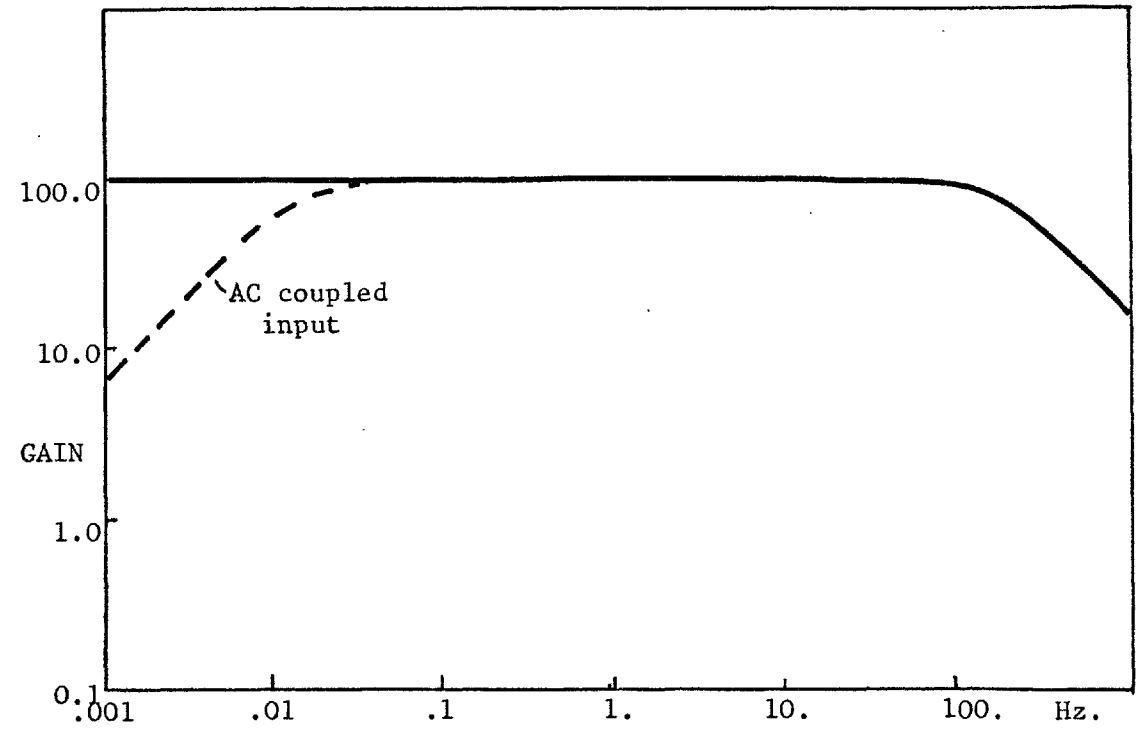


Figure 2/7 Electric preamplifier frequency response

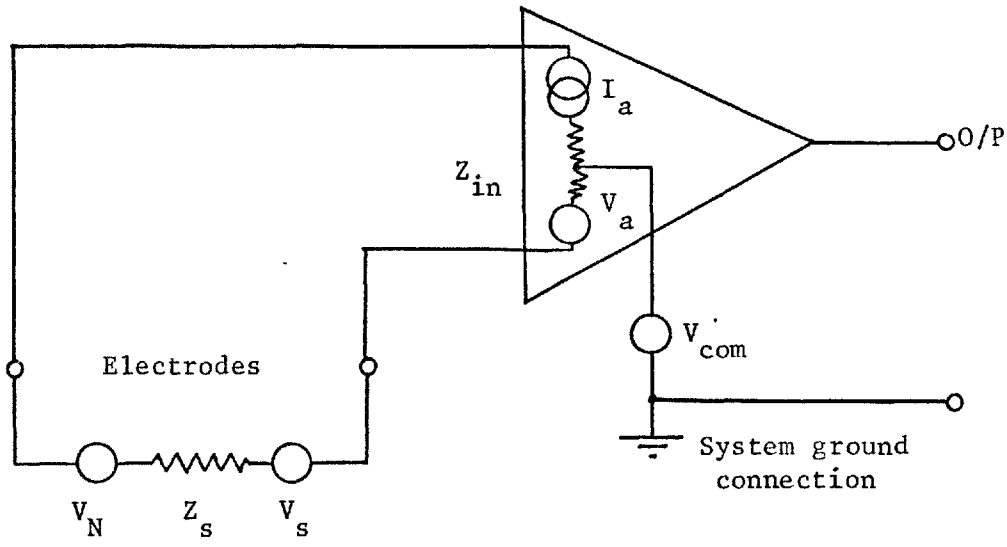


Figure 2/8 Equivalent circuit for electric field pickup

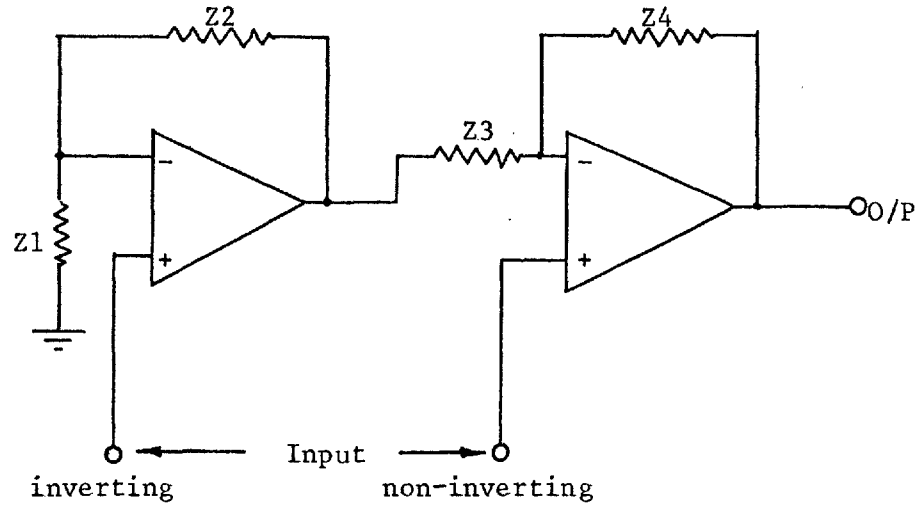


Figure 2/9 Electric preamplifier schematic diagram

The source impedance Z_S is equal to the ground impedance plus the electrode contact resistance; the latter is the dominant part, and can vary from a few ohms in damp soil to several megohms in frozen ground. If the amplifier input impedance Z_{IN} is made large compared with 1 megohm, the effect of variable Z_S is negligible. Field Effect transistor input stages fulfil this requirement with an input resistance of about 10^8 megohms and a parallel capacitance of about 5 pF giving an impedance of about 300 Megohms at 100Hz.

2.5.2 Signal Pickup Noise

The equivalent noise generator V_N in Fig 2/7 has three components; Johnson noise of the source impedance Z_S, e.m.f.s caused by the wind induced motion of electrode wires in the earth's static magnetic field, and contact effects at the electrodes. The Johnson noise may readily be estimated by applying the formula (Bleaney and Bleaney 1959, p.271)

$$V_J = (4kTRdF)^{1/2} \qquad 2:16$$

where V_J is the r.m.s. noise voltage
dF is the bandwidth
R is the resistance
T is absolute temperature of the source resistance in equilibrium
k is Boltzmann's constant, 1.38×10^{-23} J/°K

The r.m.s. noise per root Hz bandwith is less than 100 nV for a 10 kohm source resistance at 300°K.

The effect of allowing electrode wires to move in the wind can be illustrated by considering the simplified case of a small element of wire x moving sinusoidally with frequency ω and amplitude a normal to a magnetic induction B. The amplitude of the induced e.m.f. Vx is given by

$$Vx = \omega a x B \qquad 2:17$$

For $x = 0.1m$, $\omega = 8Hz$, $a = .01m$ and $B = 4 \times 10^{-2} W/m^2$,

$$Vx \simeq 2 \text{ microvolts.}$$

This is almost of the same order of magnitude as the signal voltage of 15 microvolts expected in the typical case of an electrode separation of 30m and an electric field of 0.5 microvolt/m. Electrode wires should therefore be weighed down to prevent them moving in the wind. This problem is confined to frequencies above about 1Hz, because wires are unlikely to vibrate appreciably at lower frequencies and the amplitude of the induced e.m.f. decreases towards lower frequencies.

Metal electrodes pushed into damp ground are subject to electrochemical e.m.f.s which depend on the type and concentration of ions in the surrounding soil. These e.m.f.s vary slowly as conditions at the electrode surface change with temperature, moisture content etc. and are generally serious only at frequencies below .001 Hz for an arrangement such as a lead plate buried and moistened with salt water (Keller and Frischknecht, 1966, p 229). This type of electrode, however, is unsuitable for rapid profiling. When measurements are to begin as soon as the electrode is in position it is advisable to use non-polarizing electrodes, consisting of a metal immersed in a saturated solution of one of its salts (Parasnis, 1966, p 80). Slankis and Becker (1969) report that at 8Hz they found no difference between the results obtained with nonpolarizing electrodes and those with brass rods driven into the ground. It seems desirable in all cases to keep the contact resistance of each electrode below about 5 kohms, otherwise effects due to static electricity can be troublesome.

In addition to the signal and the pickup noise, there is usually a static potential difference between the electrodes due to the Self Potential (S.P.) effect. (See Parasnis, 1966, p 76). This sometimes causes trouble by exceeding the dynamic range of the amplifiers but can be removed by a.c. coupling the amplifier input, or by cancellation with a potentiometer in the input circuit to maintain the d.c.level. If care is taken to keep electrode contact resistance low and to minimize movement of connecting wires, the signal pickup noise need only be of the order of 0.1 microvolts.

2.5.3 The Electric Preamplifier Design

The electric preamplifier acts as a buffer between the electrodes and the main amplifiers. The performance of the final design is summarized in Fig 2/7 and a schematic circuit is shown in Fig 2/9 (NS Linear Handbook, AN31-11). This design has the advantage that the following features can all be incorporated into it simultaneously:

Low drift and noise
High differential input impedance
Stable gain
Moderate power consumption
Passband d.c. to 200Hz

Restriction of the passband to 200Hz was found to be necessary to reduce V.L.F. interference which can cause complete saturation of the amplifier output, giving severe cross modulation and swamping the low frequency telluric signals. Each operational amplifier in Fig 2/9 is a hybrid, comprising a differential monolithic FET pair followed by an integrated bipolar main amplifier (see Fig A/20). The response of the amplifier is given by

$$\text{GAIN} = 1 + \frac{Z4}{Z3}, \quad (Z4 = Z1, Z2 = Z3) \qquad 2:18$$

The common mode rejection ratio is determined by the accuracy of the matching of Z1, Z2, Z3 and Z4. Optional AC input coupling is provided for removing the S.P. voltage between the electrodes and reducing unwanted low frequency signals. The time constant is 10 seconds, but can easily be altered.

2.6 Calibration

Calibration is necessary to ensure that the response of the complete recording system is known accurately and that it does not vary with time. An electric field channel is calibrated simply by applying a signal of known amplitude to the input and plotting the output amplitude as a function of frequency. When two or more channels are involved the relative phases of the outputs should also be plotted.

Absolute calibration of a magnetometer can be achieved by placing it on the axis of a small rotating bar magnet, parallel to the plane of rotation (see Fig 2/10). If the distance from the magnet is large compared with its dimensions, it can be considered as an oscillating dipole with field components given by

$$H_r = \frac{2\mu_0 m \cos\theta}{r^3} \qquad 2:19$$

$$H_\theta = \frac{\mu_0 m \sin\theta}{r^3} \qquad 2:20$$

Where m is the dipole moment, H_r and H_θ are the radial and tangential components of the field at r,θ. An $e^{j\omega t}$ time dependency is assumed. If the effective length of the magnetometer is l and its distance from the magnet is x, the variation of the field over the length of the magnetometer is calculated as follows : When the angle subtended at the magnet by the magnetometer is 2φ, the axial field H_a at one end of the magnetometer is given by 2:21,

$$H_a = \frac{\mu_0 m}{x^3}(\sin(90-\varphi)\cos\varphi + 2\cos(90-\varphi)\sin\varphi) \quad 2:21$$

and the field in the centre of the magnetometer, H_b, by

$$H_b = \frac{\mu_0 m}{x^3} \quad 2:22$$

Combining these two equations, we can derive an expression for the percentage variation, P_H, of the field over the length of the magnetometer

$$P_H = 100\left(1 - \frac{1}{\cos^2\varphi + 2\sin^2\varphi}\right) \quad 2:23$$

P_H is less than 1% for angles φ up to about 5°.

The effective length l of the magnetometer is the distance over which the core produces appreciable disturbance of the primary magnetic field. For a long, high permeability core the effective length is up to ten times the physical length. To keep φ small the distance x should be as large as possible, consistent with maintaining adequate calibration field strength against the natural field background. The magnetic moment of the bar magnet is determined by measuring its field at a known distance with an absolute instrument such as a proton precession magnetometer.

Magnetotelluric measurements of apparent resistivity depend on the ratio E/H, so that the consistency of the results depends on the ratio of electric and magnetic channel responses. Absolute apparent resistivity values require a knowledge of the magnetometer sensitivity (in volt/nT), the electric field sensitivity (in volt/microvolt) and the electrode spacing (in metres). Absolute calibration of induction magnetometers is difficult under field

conditions, but the response relative to an electric channel can be checked in the following way. An alternating current is passed through a small extra winding on the magnetometer coil (see Fig 2/11) and also through a high stability resistor R connected across the input of the electric preamplifier. Providing the dimensions and position of the coil are stable, the amplitude of the field in the magnetometer core is given by

$$H = ik \qquad 2:24$$

Where k is a constant depending on the magnetometer and coil dimensions and i is the amplitude of the current. The input to the electric preamplifier is given simply by Ohms law

$$V = iR \qquad 2:25$$

Where V is the amplitude of the voltage at the preamplifier input. If the electric and magnetic channel overall sensitivities are A and B respectively and their outputs V_e and V_h

$$V_e = iRA$$

$$V_h = ikB$$

The ratio of the outputs is independent of i, so that

$$A/B = kV_e / RV_h \qquad 2:26$$

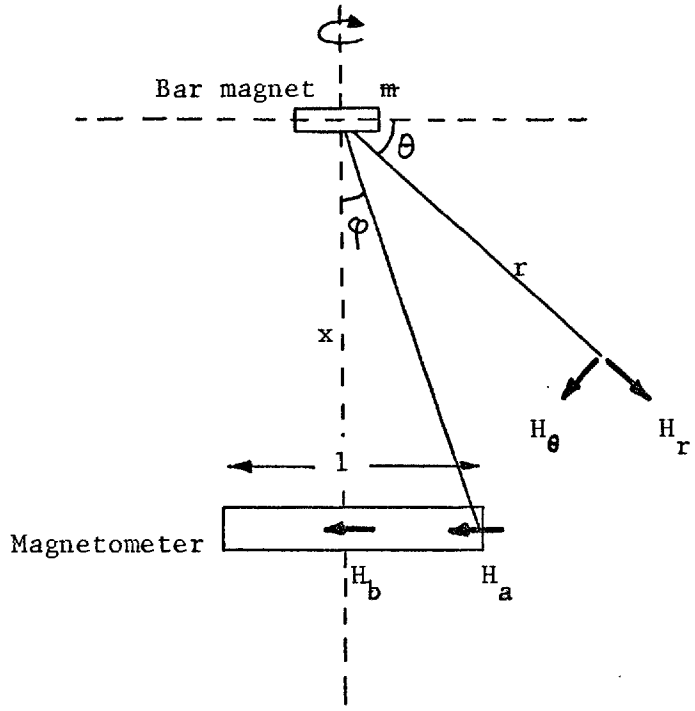


Figure 2/10 Absolute calibration of Magnetometer

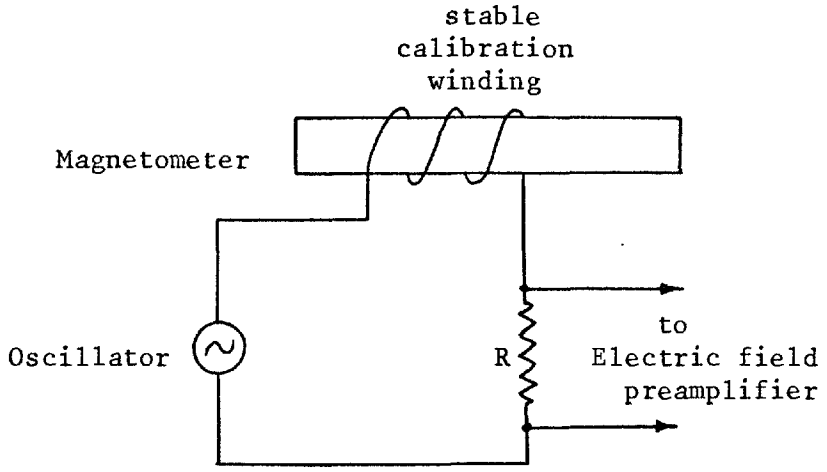


Figure 2/11 Relative calibration Electric/Magnetic

CHAPTER 3

PORTABLE RECORDING AND TELEMETRY EQUIPMENT

3.1 General Description of Equipment

Magnetotelluric and Telluric methods require that at least two components of the natural electromagnetic field are measured simultaneously. The field equipment described here is designed to amplify up to six preamplifier outputs at a time for recording or direct measurement. An FM frequency division multiplex system is used for recording and telemetry, with carrier frequencies corresponding to those used by the commercial Lennartz 7032/7002 system (Fig 3/1). The advantages of this type of system are its simplicity, cheapness and low power consumption and the fact that it enables multi-channel recordings to be made on a straightforward 'domestic' audio tape recorder. The dynamic range of about 50dB per channel and frequency response from d.c. to 200Hz are adequate for our purposes.

The equipment can be divided into two parts, A and B, which act as 'base' and 'roving' stations for Telluric measurements. Station A comprises two identical main amplifier channels whose outputs frequency modulate a pair of audio frequency carrier waves (see Figs 3/1 and 3/2). These are multiplexed and passed via a radiotelephone link to station B. There they are separated and demodulated so that the observer can monitor signals from the two stations simultaneously. Station B can accommodate up to four main amplifiers, each modulating separate carriers; these are mixed with the composite carrier from station A for recording on a battery tape recorder. An unmodulated pilot tone is added to the multiplexed carriers to provide timing and tape speed compensation on playback.

Channel	Centre Frequency	Deviation	Station	
	KHz	%		
1	.86	±15	A	
2	2.1	±15	A	
3	4.4	±7.5	B	
Pilot tone	6.4	0	B	
4	9.5	±7.5	B	
5	13.0	±7.5	B	Only used when recording 6 channels
6	17.5	±7.5	B	

Figure 3/1 Carrier frequencies for FM recording and telemetry

3.2 Construction

Although the apparatus is experimental, attempts have been made to adhere to the principles of good field equipment design, by aiming for low power consumption, reliability and ease of operation, combined with good performance in outdoor conditions. Owing to limitations in time and resources, however, there is still room for future improvements.

The equipment is constructed on the modular rack principle to allow design changes to be incorporated with the minimum of reconstruction (Fig 3/3). Each 'module' consists of a plug-in printed circuit card or 'Veroboard' (a perforated plastic board with copper strip connections) with a front panel carrying the controls (Fig 3/4). Interconnections between modules are effected at the back of the module rack by linking the appropriate pins on the 24 way edge connectors. The functions of the various modules are summarized in Fig 3/5. Station A comprises a Battery pack, Power Stabilizer, two Main Amplifiers and a dual Voltage Controlled Oscillator (VCO), which fit into an 8" wide rack, as shown in Fig 3/3. Station B can accommodate several combinations of

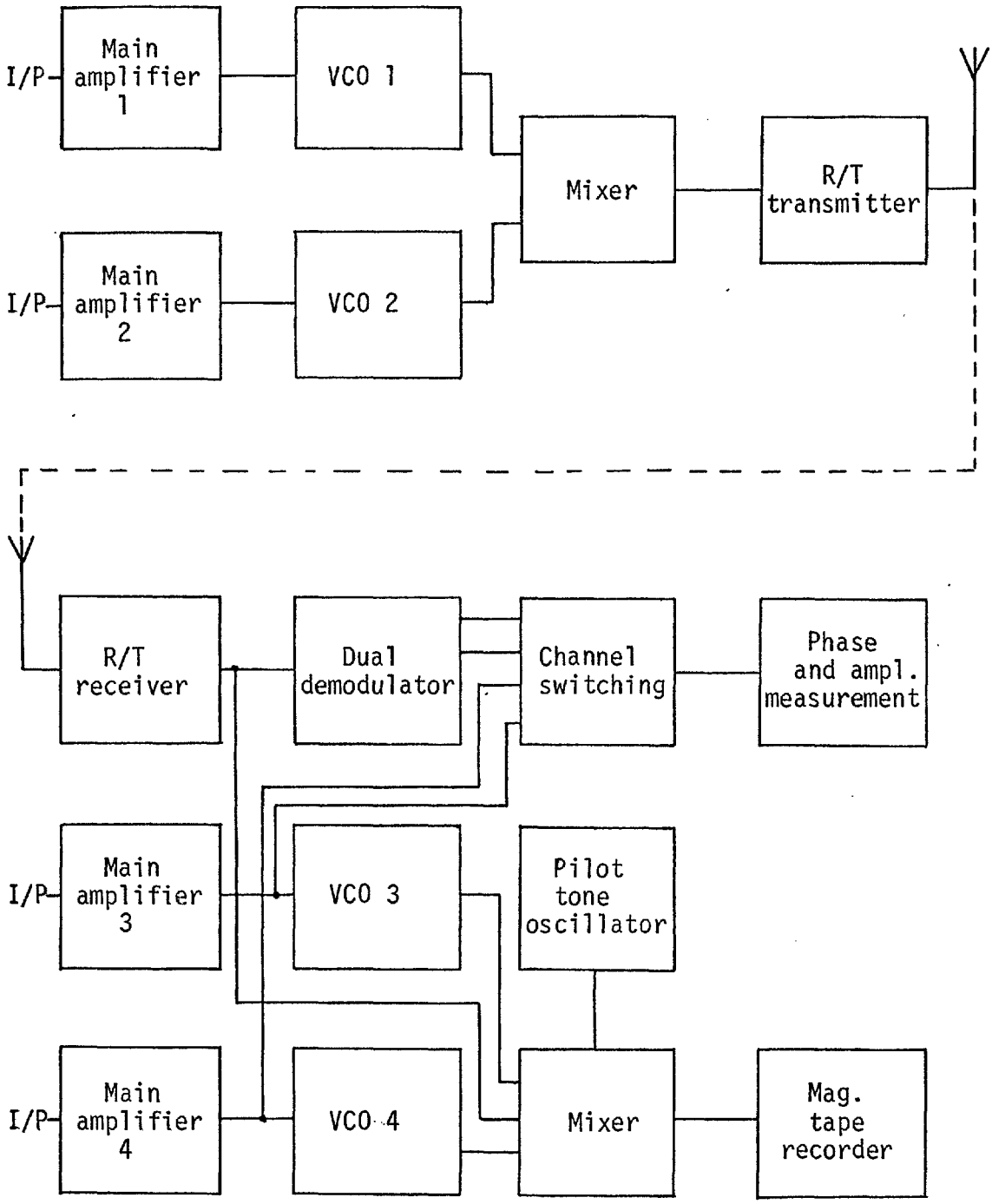


Figure 3/2 Block diagram of field recording and telemetry system (4 channel configuration)

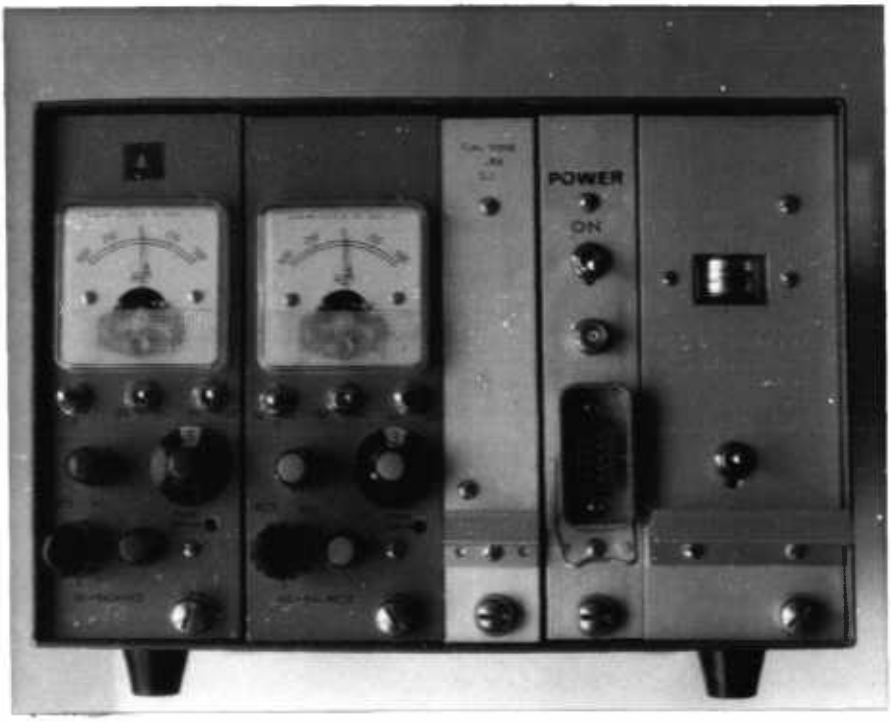


Figure 3/3 Station A Rack & Modules

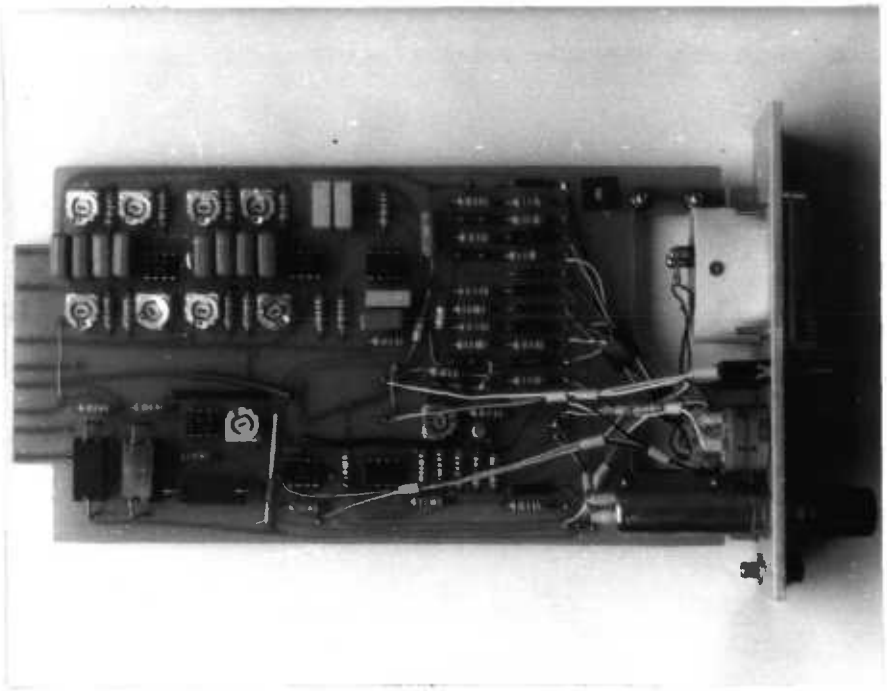


Figure 3/4 A Main Amplifier Module

MODULE	FUNCTION	NO.BUILT
Main Amplifier†	Amplifies, filters and monitors outputs from pre-amplifiers	6
Dual V.C.O.†	Connected to outputs of main amplifiers to produce F.M. carriers for recording, telemetry	3
Pilot tone and Mixer†	Produces unmodulated pilot tone as a reference signal for recording. Mixes and monitors V.C.O. outputs	1
Dual Demodulator†	Separates and demodulates 2 F.M. carriers produced by dual V.C.O. module and transmitted over telemetry link	1
Power Stabilizer†	Produces stabilized +5v and -5v supply for other modules. "Raw" D.C. input from battery module or external source	2
Battery Pack†	Contains 12 dry cells producing +9 volt and -9 volt to supply power stabilizer	2
Input connector†	Input connectors for Main amplifiers are mounted on the panel of this module	1
Filter and Phasemeter*	2 band pass filters and phase meter for analysis of signals in field or lab.	1
R.M.S. Meter*	2 full wave rectifier circuits, with smoothing, for amplitude measurements.	1
Timer*	Produces time marker pulses from pilot tone when tapes are replayed	1

† described in Chapter 3. Circuit and setting up in Appendix A

* described in Chapter 4. Circuit and setting up in Appendix A

Figure 3/5 Plug-in Modules and their functions

modules to give 4 channel recording (2 channels from each station) with direct phase and amplitude measurement, 4 channel recording alone (no station A) or 6 channel recording (2 channels from Station A, 4 from Station B). The positioning of the modules in the Station B rack for these configurations is shown in Fig 3/7 and the modules for amplification, telemetry, recording and power supply are described in sections 3.3 to 3.8 below. The Filter/phasemeter and RMS voltmeter modules, for the direct amplitude and phase measurement, are described in Chapter 4.

3.3 The Main Amplifier Modules

The purpose of the main amplifiers is to increase signals from the magnetic or electric preamplifiers to a level suitable for recording, filtering and display, and to limit the pass band. Freedom from drift and cross-talk is obtained by using operational amplifier feedback circuits (Clayton 1969) to keep impedances as low as possible and maintain adequate immunity from coupling via the power supplies. The elements making up a main amplifier are shown in Fig 3/8 and the specifications and frequency response in Fig 3/9.

3.3.1 Notch Filter

One of the most troublesome forms of interference in the E.L.F. band is noise from A.C. power distribution systems, which operate at frequencies of about 50 or 60Hz (see section 2.4). In extreme cases, complete saturation of the amplifier output occurs if these frequencies are not heavily attenuated. The first stage of the main amplifier circuit is a notch rejection filter which can be preset between 45Hz and 60Hz, according to the local interference frequency.

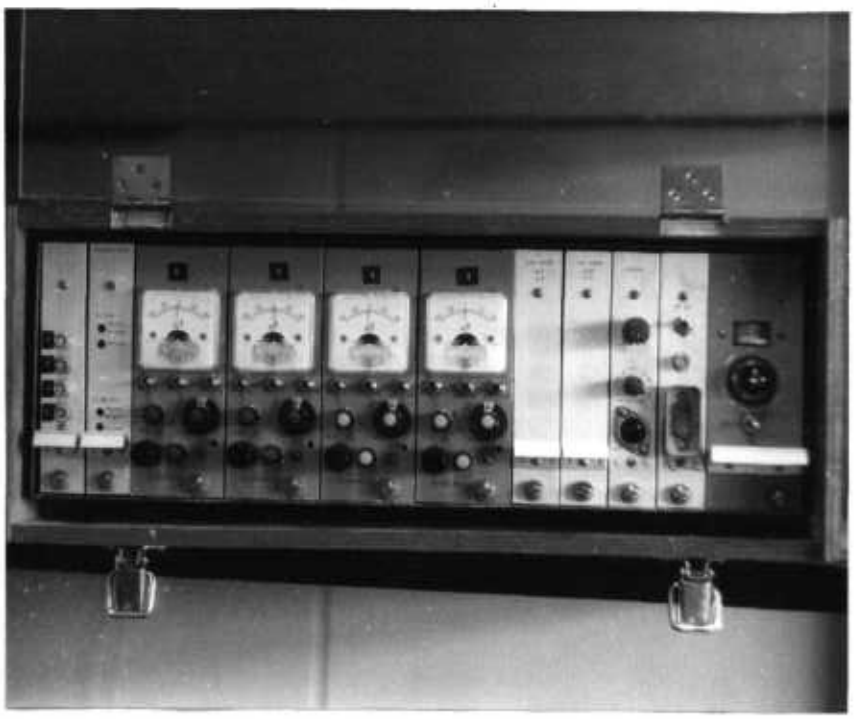


Figure 3/6 Station B, Rack & Modules

(A)

I/P Connectors	Demodulator	Main amp. 3	Main amp. 4	Filter/Phase	RMS meters	Dual VCO 3/4	Dual VCO 5/6	Pilot tone/mix	Power stab.	Batteries

(B)

I/P Connectors	Demodulator	Main amp. 3	Main amp. 4	Main amp. 5	Main amp. 6	Dual VCO 3/4	Dual VCO 5/6	Pilot tone/mix	Power stab.	Batteries

Figure 3/7 Station B rack (a) 4 channel configuration
(b) 6 channel configuration

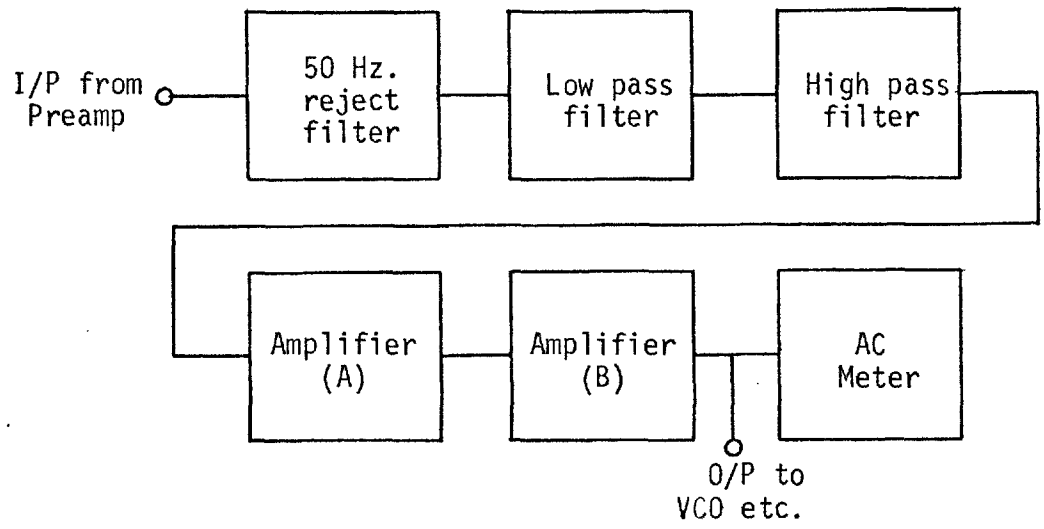
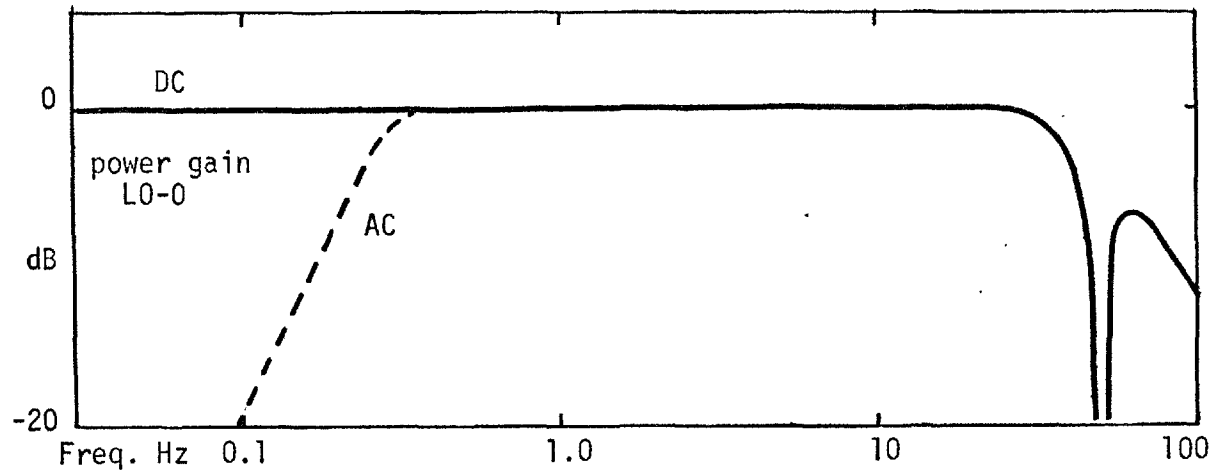


Figure 3/8 Main Amplifier block diagram



Brief specification:

GAIN 0-80 dB(power) in 4dB steps
RESPONSE DC-40Hz or 0.255Hz-40Hz
I/P impedance 30kohm
O/P impedance 1 ohm
O/P swing ±4 volts
SUPPLY ±5 volts
50Hz reject 40dB, 49-51Hz

Figure 3/9 Main Amplifier frequency response and specifications

A single twin T feedback circuit (Girling and Good 1969) was tried but did not give adequate rejection over a sufficiently wide bandwidth to allow for variations in the interference frequency and component drift. A double stagger-tuned filter was therefore designed, giving the notch at 50Hz shown in Fig 3/9. This circuit has proved to be very satisfactory.

3.3.2 Low Pass Filter

The high frequency response of the main amplifier is limited by the low pass filter to below 45Hz in order to reduce high frequency interference at harmonics of the power line frequency. The low pass response also helps to avoid aliasing if the output is digitized. The active filter is a conventional multiple feedback circuit (Burr Brown, 1968, p.74), using an integrated operational amplifier. The -3dB frequency is 45Hz and the roll off is 12dB per octave. These parameters can easily be altered, if necessary, by substituting new values for the components in the feedback network.

3.3.3 High Pass Filter

The amplitudes of fluctuations due to preamplifier drift, electrode instability or long period signals at frequences below 0.1Hz (see 2.2) may be sufficiently large to saturate the output stage of the main amplifier if steps are not taken to limit its low frequency response prior to the gain stages. An optional high pass filter is therefore included to reduce these effects and to discriminate against the low frequency "1/f" noise from the integrating preamplifiers used in the induction coil magnetometers (see section 2.4.4)

The multiple feedback high pass circuit (Burr Brown, 1968, p.76) uses a type 741 integrated operational amplifier. It has unity gain in the pass band, with the -3dB point at 0.1Hz and a roll off of -12dB per octave. As with most active filter circuits, the cut-off frequency can easily be altered by substituting new values for the feedback components. The effect of the filter on the low frequency response of the main amplifier is shown by the dashed curve in Fig 3/9.

3.3.4 Gain Stages

The maximum output swing of the amplifier is determined by the power supply voltage of $\pm$5 volts and is limited to about $\pm$4.4 volts. This limiting action is exploited by designing the recording and meter circuitry for a full scale input level of $\pm$4 volts, so that serious overdriving cannot take place. In order to maximize the signal to noise ratio of the recording equipment, the peak output signal from the amplifier must be $\pm$4 volts even though the mean input level may be anywhere between 100 microvolts rms and 1 volt rms, according to the prevailing signal strength. This range is accommodated by including two variable gain stages. (see circuit, Appendix A, Fig A/4). The first, amplifier A5, has a power gain of 0db or 40dB and consists of an operational amplifier circuit with two alternative feedback resistors selected by a coarse gain switch. The second gain stage, amplifier A6, has ten alternative feedback resistors which give a gain range of 0 to 40dB in 10 steps of 4dB. These two stages, used in conjunction, give a range of 0 to 80dB in 4dB steps.

3.3.5 Meter and Balance circuits

A meter is provided to monitor the signal at the amplifier output and to check the D.C. balance of

the gain stages. The meter function selector switch has three positions :

AC - Meter reads 0-5 v r.m.s. at output of amplifier
DC1 - Meter reads 5-0-5 v D.C. at input of amplifier
DC2 - Meter reads 5-0-5 v D.C. at output of amplifier

"Coarse" and "fine" D.C. balance potentiometers on the front panel are used for setting the output of the amplifier to zero volts in the presence of a D.C. signal at the input.

The time constant of the meter in the A.C. mode may be set to long (10 secs), medium (2 secs) or short (natural time constant of meter $\simeq \frac{1}{2}$ sec) so that the approximate level of the signal can be observed. The gain is then adjusted until the peak signal level is just below the point at which the amplifier starts to limit ($\pm$4 volts). This ensures that the full dynamic range of the recording system is used, and hence that maximum signal to noise ratio is achieved.

3.4 Dual Voltage Controlled Oscillator Module

The F.M. carriers for telemetry and recording are produced by voltage controlled oscillators driven by the main amplifier outputs. Each module contains two complete circuits, which comprise an astable multivibrator and a low pass filter. The input voltage determines the discharge current of the multivibrator capacitors through a pair of current sources and hence controls the frequency of oscillation. Each square wave multivibrator output is passed through a two stage active low pass filter to attenuate higher harmonics, leaving a sinewave which can be mixed with other carriers for multi-channel recording. An offset is applied to the current sources so that with the input voltage zero, the circuit oscillates at a constant frequency fo

corresponding to the carrier centre frequency. When an input voltage V is applied, the output frequency is given by f = fo + aV, where a is the VCO conversion constant, which determines the deviation of the carrier at full modulation (see Fig 3/1). The circuit is temperature compensated to keep centre frequency drift below 1% in the range of $0^{o}C$ to $30^{o}C$ and the linearity is better than $\pm$1% over the operating range.

3.5 Pilot tone/mixer module

The pilot tone, for tape speed compensation and timing, is generated by dividing the output from a 100kHz crystal oscillator by 16 to give a frequency of 6.250kHz. The divider, a 4 bit integrated circuit binary counter, has a square wave output which is band pass filtered to produce the sinusoidal pilot tone (see Fig A/10). This is summed with the 6 F.M. carriers by an operational amplifier prior to recording on a battery portable tape recorder. A Uher 4200 "Report" tape recorder was found to give good results. A selector switch allows the carriers to be monitored individually for testing and level adjustment.

3.6 Telemetry link

The simplest way of transferring the F.M. carrier from station A to station B is by cable, but this restricts freedom of movement and introduces the danger of interaction between the stations due to common mode effects. A radio link is used instead. It consists of a Bradley sonobouy Tx 27/1 Transmitter working at 27 MHz, and a Heathkit "Mohican" general purpose receiver. This arrangement works satisfactorily over a range of about 1 mile, but the receiver is cumbersome and insufficiently weatherproof.

3.7 Dual Demodulator Module

The dual demodulator module at station B reproduces the outputs of the two station A main amplifiers. Its input is a mixed pair of F.M. carriers from the output of the telemetry receiver. These are separated prior to demodulation by band pass filters tuned to the carrier centre frequencies of 860Hz and 2.1kHz (see Fig 3/10). Each filter has two active multiple feedback bandpass sections, stagger tuned to ensure adequate bandwidth and good rejection of the unwanted carrier. The output from each filter, a frequency modulated sinewave, is converted to a squarewave by a limiter consisting of a saturating operational amplifier. Leading edges of the square-wave trigger a monostable circuit to produce a train of pulses, which have width τ repetition rate f and amplitude Vo. f is the instantaneous carrier frequency, and Vo and τ are constants. Following the monostable is a low pass filter, with a time constant long compared with τ , so that its average output V is given by $V = Vof\tau$. The first stage of the filter has a variable input offset circuit (see Fig A/13). The input offset is adjusted to give zero DC output level when the frequency at the demodulator input corresponds to the correct carrier centre frequency. The output voltage is then given by $V=r(f-fo)$, where r is a constant. The cut-off frequency of the low pass filter is 100Hz and the rolloff is 80dB/decade so that the carrier level at the output is about 70dB below the monostable pulse amplitude, i.e. about 1mV for an 850Hz carrier. This is a compromise to give a signal frequency response up to 100Hz with reasonable carrier rejection. The pulse width of the monostable is adjustable so that the value of the conversion constant r can be varied. If $r = 1/a$, where a is the VCO, conversion constant (see section 3.4), the output from the demodulator is equal to the input of the corresponding VCO.

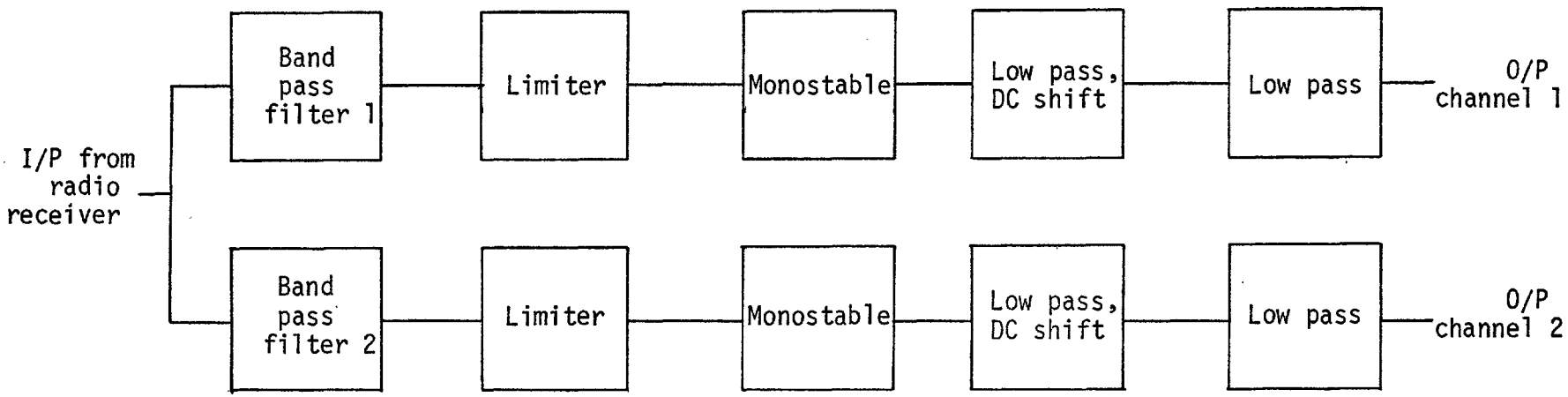


Figure 3/10 Dual Demodulator block diagram

3.8 Power stabilizer and batteries

All the modules are designed for dual positive and negative 5 volt power supplies. These are provided by series regulator transistors and a feedback circuit controlled by a zener diode, which holds the module power rails constant to $\pm$ 5mV, provided that the supply voltages remain between 7.5 volts and 16 volts. Twelve HP11 dry cells in a battery module provide +9 and -9 volts for portable operation of the equipment. An indicator is provided to check the condition of the batteries, which should be changed when the voltage falls to 7.5 volts (1.25 volts per cell). For long periods of continuous operation an external supply, such as nickel-cadmium accumulators, is recommended.

CHAPTER 4

DATA REDUCTION

4.1 Data reduction is the process in which values of impedance or telluric tensor elements are produced from field recordings, or from the direct outputs of the field equipment. The principles involved in obtaining telluric tensors and impedance tensors are very similar; the discussion which follows is equally applicable to the magnetotelluric and telluric methods.

The tensor elements are complex, slowly varying functions of frequency, whereas the fields which they relate are real functions of time. Frequency analysis, making use of the Fourier transform, is thus the core of the data reduction procedure.

4.1.1 Frequency analysis

Consider a function of time f(t) which is to be represented as a function of frequency F(ω). The relationships between f(t) and F(ω) are expressed as the Fourier transform pair

$$f(t) = \frac{1}{2\pi}\int_{-\infty}^{\infty} F(\omega)\, e^{j\omega t}\, d\omega \qquad 4:1$$

$$F(\omega) = \int_{-\infty}^{\infty} f(t)\, e^{-j\omega t}\, dt \qquad 4:2$$

The integral in equation 4:2 will be referred to as the "-j transform" to distinguish it from 4:1. The transforms are to be used to manipulate finite length sections of functions which exist for all time. Truncation of functions with constant mean power, such as stationary random processes, is necessary because the transforms are only valid

for functions with finite energy. The simplest estimate of power spectral density $P(\omega)$ is the periodogram, given by

$$P(\omega) = \frac{|F_T(\omega)|^2}{2T} \quad \lim \text{ as } T \to \infty \qquad 4:3$$

where $f_T(t) = f_\infty(t)b(t)$

$f_T(t)$ is a section of length $2T$ from a function
$f(t)$ which exists between $t = \pm\infty$
$F_T(\omega)$ is the -j transform of $f_T(t)$
$b(t)$ is a "block window" in the time domain such that

$b(t) = 1 \quad |t| \leq T \quad , \quad b(t) = 0 \quad |t| > T$ (see Fig 4/1a)

and

$$F_T(\omega) = \int_{-\infty}^{\infty} f(t)\,b(t)\,e^{-j\omega t}\,dt \qquad 4:4$$

In the frequency domain this is equivalent to the convolution integral

$$F_T(\omega) = \int_{-\infty}^{\infty} F(\omega)\,B(\omega-\omega_0)\,d\omega \qquad 4:5$$

where $B(\omega)$ is the -j transform of the block window $b(t)$, and $\omega_0 = \pi/T$

$$B(\omega) = \frac{2\pi}{\omega_0}\,\frac{\sin(\pi\omega/\omega_0)}{(\pi\omega/\omega_0)} \qquad 4:6$$

As T increases, the total energy of the section $f_T(t)$ rises, but the width of the window $B(\omega)$ decreases. The net result is that the bandwidth over which $F_T(\omega)$ is averaged by the convolution 4:5 decreases in such a way as to keep the mean energy used in forming each estimate of $P_T(\omega)$ constant. The variance of a set of independent estimates of $P_T(\omega)$ does not therefore decrease as T is increased. A further limitation of the block time window is that the amplitudes of the side lobes of its Fourier transform fall off only as $1/\omega$, so

that each spectral estimate contains appreciable power from other parts of the spectrum (see Fig 4/1 f). These drawbacks can be overcome by averaging adjacent spectral estimates to reduce variance at the expense of resolution, and by using special windows in the time domain. The Hanning window H(t), given by

$$H(t) = 0.5(1 - \cos \pi t/T) \quad |t| \leq T$$
$$H(t) = 0 \quad |t| > T$$

has side lobes in the frequency domain which fall of as $1/(\omega-\omega_0)^3$, although the central lobe is twice as wide as that of the block window (see Fig 4/1 and Sims and Bostick 1969). The shape of a window in the frequency domain is important because spectral estimates can sometimes be seriously distorted by nearby peaks in the spectrum which coincide with side lobes. This problem can be overcome by "pre-whitening" data at the recording stage with an analogue filter having a relative response inversely proportional to the expected relative power spectral density at each frequency. (Blackman and Tukey, 1959 p 28). One of the advantages of induction magnetometers at frequencies below 1Hz is that they automatically provide pre-whitening of the geomagnetic power spectrum, which rises at almost the same rate as the magnetometer sensitivity falls with frequency. (see Figs 2/2 and 2/6). In the Schumann band, the complexity of the spectrum makes pre-whitening difficult, but the relatively low quality factor (Q) of the resonances ($Q \simeq 5$. Bleil, 1964, p 237) allows reasonable spectral estimates to be made without it.

It is apparent that large transient events, selected from a record with a small, approximately constant background level, should not be treated in the same way as sections of record containing no events. Consider the truncated cosine wave in Fig 4/1(c), which has a -j transform as in Fig 4/1(h). If it

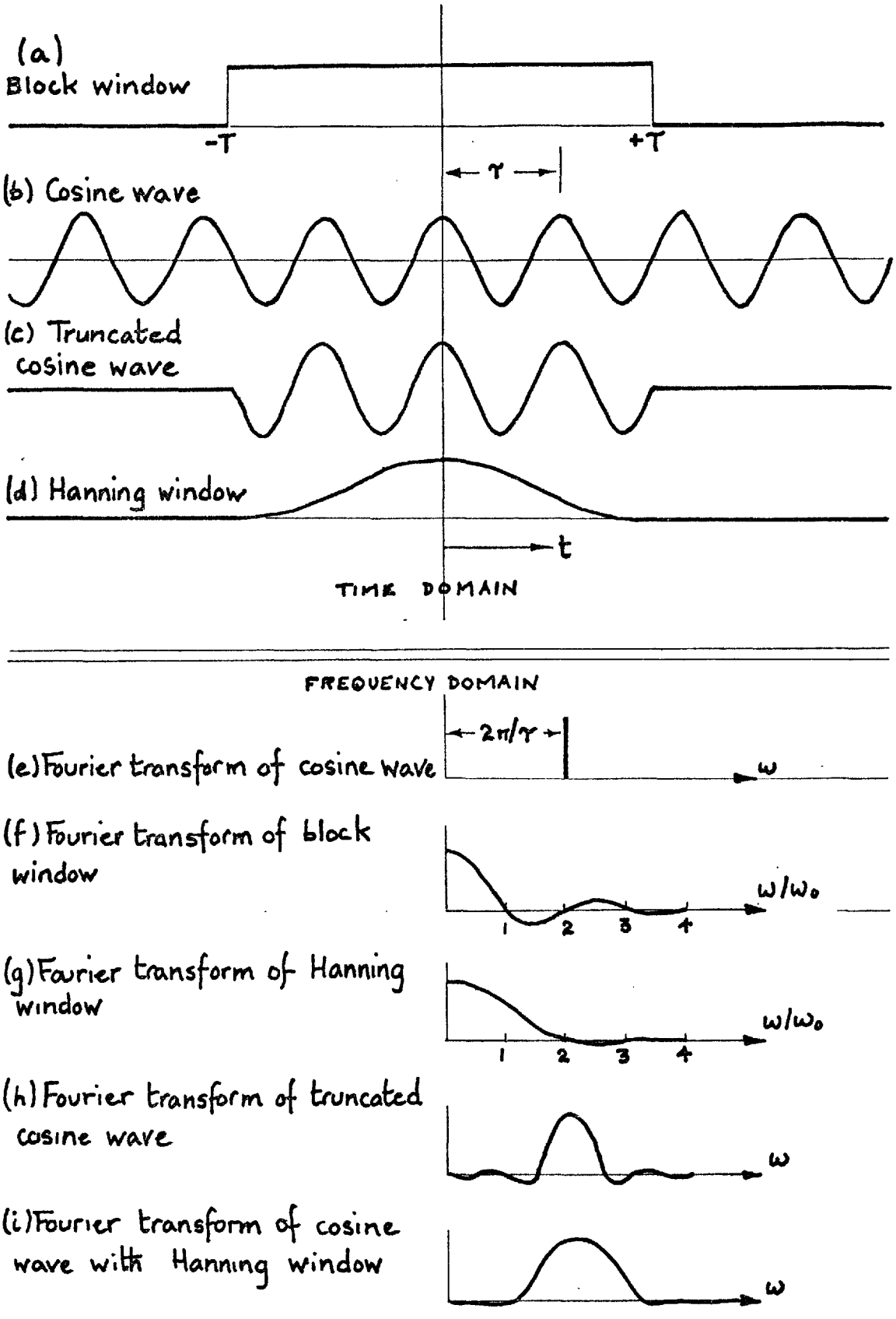


Figure 4/1 Some functions and Fourier transforms

was treated as part of a continuous cosine wave (Fig 4/1(b)) and a Hanning window applied, the side lobes of the -j transform would be reduced and the transient character of the original function masked (Fig 4/1(e)). Large events are often chosen for analysis, because they use most of the dynamic range of the recording system, and contain a lower percentage of pickup noise than small signals. When such events are Fourier transformed directly, without prior application of special windows, the process is known as "Fourier transient analysis".

4.1.2 Cross spectra and coherency, cross correlation

When two or more functions of time are considered, their cross power spectra P_{ij} are defined by

$$P_{ij}(\omega) = |F_i(\omega) F_j^*(\omega)| \qquad 4:7$$

where * indicates complex conjugation,

F_i and F_j are -j transforms of the i^{th} and j^{th} time series, and $|\ |$ signifies the modulus of a complex quantity. The cross phase spectrum, $\Phi(\omega)$, is given by

$$\Phi_{ij}(\omega) = \arg(F_i(\omega) F_j^*(\omega)) \qquad 4:8$$

where arg signifies "complex argument of". Another useful quantity is the coherency, Kij, a measure of the similarity of two functions given by

$$Kij = \frac{P_{ij}(\omega)}{(P_{ii}(\omega) \cdot P_{jj}(\omega))^{1/2}} \qquad 4:9$$

The modulus of the coherency varies between zero (uncorrelated signals) and one (identically shaped signals).

The cross correlation (or cross covariance) function of two time seris is defined by the convolution integral :

$$C_{ij}(\tau) = \int_{-\infty}^{\infty} f_i(t) f_j(t-\tau) dt \qquad 4:10$$

where $C_{ij}(\tau)$ is the cross correlation for a lag τ between functions f_i and f_j. The power spectrum Pij can be obtained from the -j transform of $C_{ij}(\tau)$, a process which forms the basis of the method known as "power spectral analysis". Blackman and Tukey (1959) can be consulted for details of this technique, which is sometimes used in magnetotellurics in preference to the Fourier transient method.

4.2 Determination of Tensor Elements

Impedance tensor elements can be determined from amplitude spectra in several ways. The simplest is the method of simultaneous equations, proposed by Cantwell (1960). Complex spectral amplitudes are obtained for Ex, Ey, Hx and Hy at each desired frequency, for two different record sections I and II. The two equations

$$Ex^{I} = Z11\,Hx^{I} + Z12\,Hy^{I} \qquad 4:11$$

$$Ex^{II} = Z11\,Hx^{II} + Z12\,Hy^{II} \qquad 4:12$$

can then be solved for Z11 and Z12. The other two tensor elements are obtained in a similar manner (see for example Tammemagi and Lilley, 1972).

Another method, in the form described by Sims et al (1969) achieves least mean square estimates of the tensor elements from time averages of cross and auto-power spectra. One may define

$$\psi = \sum_{i=1}^{n} (Ex_i - Z11_i Hx_i - Z12_i Hy_i) \cdot (E^*x_i - Z11_i H^*x_i - Z12_i H^*y_i) \qquad 4:13$$

if there are n measurements of Ex etc. The values

of Z11 and Z12 can then be found such that ψ is minimized. Setting the derivatives of ψ with respect to the real and imaginary parts of Z12 to zero gives

$$\sum_{i=1}^{n} Ex_i H\dot{y}_i^* = Z_{11}\sum_{i=1}^{n} Hx_i H\dot{y}_i^* + Z_{12}\sum_{i=1}^{n} Hy_i H\dot{y}_i^* \qquad 4:14$$

A similar distinct equation in Z11 and Z12 can be obtained by setting to zero the derivatives of ψ with respect to Z11. Note that the summations represent averages of auto and cross power spectra over a finite bandwith.

$$\sum_{i=1}^{n} Ex_i H\dot{x}_i^* = Z_{11}\sum_{i=1}^{n} Hx_i H\dot{x}_i^* + Z_{12}\sum_{i=1}^{n} Hy_i H\dot{x}_i^* \qquad 4:15$$

These two equations can be solved for Z11 and Z12 to obtain estimates in which errors due to noise on Ex are minimized. Two more equations in Z11 and Z12 can be obtained using the relationship

$$\psi = \sum_{i=1}^{n} \left(Hx_i - \frac{Ex_i}{Z_{11}} + \frac{Z_{12}}{Z_{11}} Hy_i \right)$$

$$\cdot \left(H\dot{x}_i^* - \frac{E\dot{x}_i^*}{Z_{11}} + \frac{Z_{12}}{Z_{11}} H\dot{y}_i^* \right) \qquad 4:16$$

which minimize the effects of noise in Hy. There are then four simultaneous equations containing Z11 and Z12 which may be solved to give six distinct solutions both for Z11 and Z12. For further details of this technique, see Sims et al. (1969). Expressions for the telluric tensor elements in terms of auto and cross power spectra of electric field components can be obtained in a similar manner. The resulting equations are listed in Fig 4/2. Two of the six expressions for each tensor element are unstable for a one dimensional situation with

$$1\quad A11 = \frac{(EU \cdot EX^*)(EY \cdot EY^*) - (EY \cdot EX^*)(EU \cdot EY^*)}{(EX \cdot EX^*)(EY \cdot EY^*) - (EY \cdot EX^*)(EX \cdot EY^*)}$$

$$2\quad A11 = \frac{(EU \cdot EX^*)(EY \cdot EU^*) - (EY \cdot EX^*)(EU \cdot EU^*)}{(EX \cdot EX^*)(EY \cdot EU^*) - (EY \cdot EX^*)(EX \cdot EU^*)}$$ Unstable

$$3\quad A11 = \frac{(EU \cdot EX^*)(EY \cdot EV^*) - (EY \cdot EX^*)(EU \cdot EV^*)}{(EX \cdot EX^*)(EY \cdot EV^*) - (EY \cdot EX^*)(EX \cdot EV^*)}$$

$$4\quad A11 = \frac{(EU \cdot EY^*)(EY \cdot EU^*) - (EY \cdot EY^*)(EU \cdot EU^*)}{(EX \cdot EY^*)(EY \cdot EU^*) - (EY \cdot EY^*)(EX \cdot EU^*)}$$

$$5\quad A11 = \frac{(EU \cdot EY^*)(EY \cdot EV^*) - (EY \cdot EY^*)(EU \cdot EV^*)}{(EX \cdot EY^*)(EY \cdot EV^*) - (EY \cdot EY^*)(EX \cdot EV^*)}$$ Unstable

$$6\quad A11 = \frac{(EU \cdot EU^*)(EY \cdot EV^*) - (EY \cdot EU^*)(EU \cdot EV^*)}{(EX \cdot EU^*)(EY \cdot EV^*) - (EY \cdot EU^*)(EX \cdot EV^*)}$$

$$1\quad A22 = \frac{(EV \cdot EX^*)(EX \cdot EY^*) - (EX \cdot EX^*)(EV \cdot EY^*)}{(EY \cdot EX^*)(EX \cdot EY^*) - (EX \cdot EX^*)(EY \cdot EY^*)}$$

$$2\quad A22 = \frac{(EV \cdot EX^*)(EX \cdot EU^*) - (EX \cdot EX^*)(EV \cdot EU^*)}{(EY \cdot EX^*)(EX \cdot EU^*) - (EX \cdot EX^*)(EY \cdot EU^*)}$$ Unstable

$$3\quad A22 = \frac{(EV \cdot EX^*)(EX \cdot EV^*) - (EX \cdot EX^*)(EV \cdot EV^*)}{(EY \cdot EX^*)(EX \cdot EV^*) - (EX \cdot EX^*)(EY \cdot EV^*)}$$

$$4\quad A22 = \frac{(EV \cdot EY^*)(EX \cdot EU^*) - (EX \cdot EY^*)(EV \cdot EU^*)}{(EY \cdot EY^*)(EX \cdot EU^*) - (EX \cdot EY^*)(EY \cdot EU^*)}$$

$$5\quad A22 = \frac{(EV \cdot EY^*)(EX \cdot EV^*) - (EX \cdot EY^*)(EV \cdot EV^*)}{(EY \cdot EY^*)(EX \cdot EV^*) - (EX \cdot EY^*)(EY \cdot EV^*)}$$ Unstable

$$6\quad A22 = \frac{(EV \cdot EU^*)(EX \cdot EV^*) - (EX \cdot EU^*)(EV \cdot EV^*)}{(EY \cdot EU^*)(EX \cdot EV^*) - (EX \cdot EU^*)(EY \cdot EV^*)}$$

Figure 4/2 (a) Telluric tensor equations for diagonal elements

$$1\quad A12 = \frac{(EX \cdot EX^*)(EU \cdot EY^*) - (EU \cdot EX^*)(EX \cdot EY^*)}{(EX \cdot EX^*)(EY \cdot EY^*) - (EY \cdot EX^*)(EX \cdot EY^*)}$$

$$2\quad A12 = \frac{(EX \cdot EX^*)(EU \cdot EU^*) - (EU \cdot EX^*)(EX \cdot EU^*)}{(EX \cdot EX^*)(EY \cdot EU^*) - (EY \cdot EX^*)(EX \cdot EU^*)}$$ Unstable

$$3\quad A12 = \frac{(EX \cdot EX^*)(EU \cdot EV^*) - (EU \cdot EX^*)(EX \cdot EV^*)}{(EX \cdot EX^*)(EY \cdot EV^*) - (EY \cdot EX^*)(EX \cdot EV^*)}$$

$$4\quad A12 = \frac{(EX \cdot EY^*)(EU \cdot EU^*) - (EU \cdot EY^*)(EX \cdot EU^*)}{(EX \cdot EY^*)(EY \cdot EU^*) - (EY \cdot EY^*)(EX \cdot EU^*)}$$

$$5\quad A12 = \frac{(EX \cdot EY^*)(EU \cdot EV^*) - (EU \cdot EY^*)(EX \cdot EV^*)}{(EX \cdot EY^*)(EY \cdot EV^*) - (EY \cdot EY^*)(EX \cdot EV^*)}$$ Unstable

$$6\quad A12 = \frac{(EX \cdot EU^*)(EU \cdot EV^*) - (EU \cdot EU^*)(EX \cdot EV^*)}{(EX \cdot EU^*)(EY \cdot EV^*) - (EY \cdot EU^*)(EX \cdot EV^*)}$$

$$1\quad A21 = \frac{(EY \cdot EX^*)(EV \cdot EY^*) - (EV \cdot EX^*)(EY \cdot EY^*)}{(EY \cdot EX^*)(EX \cdot EY^*) - (EX \cdot EX^*)(EY \cdot EY^*)}$$

$$2\quad A21 = \frac{(EY \cdot EX^*)(EV \cdot EU^*) - (EV \cdot EX^*)(EY \cdot EU^*)}{(EY \cdot EX^*)(EX \cdot EU^*) - (EX \cdot EX^*)(EY \cdot EU^*)}$$ Unstable

$$3\quad A21 = \frac{(EY \cdot EX^*)(EV \cdot EV^*) - (EV \cdot EX^*)(EY \cdot EV^*)}{(EY \cdot EX^*)(EX \cdot EV^*) - (EX \cdot EX^*)(EY \cdot EV^*)}$$

$$4\quad A21 = \frac{(EY \cdot EY^*)(EV \cdot EU^*) - (EV \cdot EY^*)(EY \cdot EU^*)}{(EY \cdot EY^*)(EX \cdot EU^*) - (EX \cdot EY^*)(EY \cdot EU^*)}$$

$$5\quad A21 = \frac{(EY \cdot EY^*)(EV \cdot EV^*) - (EV \cdot EY^*)(EY \cdot EV^*)}{(EY \cdot EY^*)(EX \cdot EV^*) - (EX \cdot EY^*)(EY \cdot EV^*)}$$ Unstable

$$6\quad A21 = \frac{(EY \cdot EU^*)(EV \cdot EV^*) - (EV \cdot EU^*)(EY \cdot EV^*)}{(EY \cdot EU^*)(EX \cdot EV^*) - (EX \cdot EU^*)(EY \cdot EV^*)}$$

Figure 4/2 (b) Telluric tensor equations for off-diagonal elements

randomly polarized source fields. In such cases the spectral averages (ExEy*), (ExEv*), (EuEv*) and (EuEy*) tend to zero so that the equations marked unstable in Fig 4/2 are indeterminate. Random noise on any of the four signals will increase the variance of the cross power spectral estimates. Auto power estimates will always be increased if noise is present and will bias the tensor element estimates accordingly. In equation 1 for All, in Fig 4/2(a), the estimate will be biased downwards by noise on Ex, which appears in an autopower term in the denominator. The differences between the four stable estimates can be used to decide on the reliability of the measurement.

4.3 Practical Considerations

Practical approaches to data reduction can be divided into three main categories :

a) Hand calculation
b) Digital computer methods
c) Electronic analogue methods

Hand calculations from chart recordings are used extensively in the telluric method for the calculation of $\int$-values (see section 1.8, and Yungul, 1968)

In magnetotellurics they are sometimes used for approximate preliminary calculations of apparent resistivity (see, for example, Hermance and Grillot, 1970). In all cases, hand calculations are tedious and not as comprehensive or accurate as either of the other two methods. The two references given above may be consulted for details.

Magnetotelluric data analysis is usually carried out digitally, using field recordings made on magnetic tape, punched paper tape, ink charts or photographic paper. The recording time is determined by the need

to obtain several periods at least of the lowest frequency components of interest. Recordings can therefore last for hours or even days in crust and upper mantle studies. Ideally, the ratio of recording time to period should be roughly constant over the whole frequency range to be considered. In practice, this condition can be met approximately by dividing up the frequency range into several bands and recording each for a time equivalent to several periods of the lowest frequency defining the band. The high dynamic range required for satisfactory recording of the geomagnetic field fluctuations between, say, .0001Hz and 1Hz can also be reduced in this way.

At the comparatively high frequencies of interest in mineral prospecting, i.e. above about 0.1Hz, recording times of only a few minutes are necessary. Above about 1Hz, electronic circuitry can provide effective analogue data reduction from magnetic tape recordings or directly in the field from the outputs of electric and magnetic field amplifiers. An analogue computer capable of performing in the field the complete tensor analysis described in the previous sections would, however, be unnecessarily complicated. Fairly simple analogue circuitry allows the number of amplifier channels in the telluric or magnetotelluric mode to be reduced from four to two. Providing that the measuring axes are aligned along the principal directions of anisotropy, the diagonal elements of the impedance tensor are theoretically zero; a two channel system can then be used to make separate determinations of the off diagonal elements. Alignment with the principal axes can be achieved by taking readings at several azimuths; when the measurement axes are correctly aligned, the apparent resistivity is a maximum or minimum and the correlation of the two signals a maximum. This technique should work equally well for the telluric method, although in both cases the source field must be randomly polarized.

Analogue correlation techniques have been used extensively at frequencies of 50-1000Hz in the AFMAG dip angle method (Ward et al., 1958 and Lutsenko and Pushnoi, 1965). Slankis and Becker (1969) mention an integrating voltmeter for 8Hz magnetotelluric measurements; this was later abandoned in favour of hand calculations from chart recordings. More recently, a two channel system has been described for direct magnetotelluric soundings in the frequency range 8-1700Hz (Jolivet, 1969 and Benderitter et al. 1973).

4.4 Implementation of digital frequency analysis

The first step in preparing data for processing on a digital computer is digitization. An absolute requirement is that signals in the data with periods shorter than twice the sampling interval have negligible strength. This frequency is the Nyquist, or folding frequency. The Sampling Theorem states that if negligible power exists in the spectrum of a function f(t) above a frequency $1/(2\Delta t)$, where Δt is the sampling interval, then the function f(t) can be uniquely determined from its values at $t = i\Delta t$, i being an integer. The resultant set of sampled data points is called the time series.

The digitization process best suited to the equipment described in Chapter 3, is as follows; field tapes are played back through a demodulator to reproduce the analogue data signals; each signal is passed in turn into a sample/hold circuit, followed by an analogue to digital converter which produces a digital output, for recording in computer compatible format on magnetic tape. Suitable equipment was not, however, available and digitization had to be carried out manually from U.V. oscillograph charts of selected sections of recordings, using an Oscar-J chart measurer. This obsolescent machine records the

vertical position of a cursor as a 3 digit number on a punched card. The U.V. charts are produced with timing lines at the required sampling frequency, so that the cursor can be set and its height recorded at equispaced intervals along the record. The method is unsatisfactory because of the errors introduced in setting the cursor, which limit the dynamic range, and its extreme slowness. Tape and chart speed errors are minimized by deriving the timing lines for digitization from the 6.4 kHz pilot tone on the F.M. tape. The output from the pilot tone filter in the Lennartz demodulator (see Fig 4/3) is divided by 64 to produce 100Hz triggering pulses for the oscillograph timing line generator. An accuracy of better than $\pm$1 millisecond in the time positioning of each sample can be achieved in this way.

A typical program for obtaining the power spectrum of a digitized trace is outlined below:

a) Read in trace samples
b) Apply calibration
c) Remove DC level and linear trend
d) Apply time window (if necessary)
e) Fourier transform trace
f) Form $|\text{Fourier transform}|^2$
g) Apply further smoothing in frequency domain (if necessary)
h) Read out results

The removal of linear trend and DC level in operation c) is necessary to avoid distortion of the low frequency spectral estimates by a large spike at zero frequency. For the Fourier transform in e) a fast algorithm is often used (Cooley and Tukey 1965) which can save a lot of computer time. This method produces 2^n points in the frequency domain from an original data length of 2^n points where n must be an integer. Data with lengths differing from an integral power of two points are truncated, or

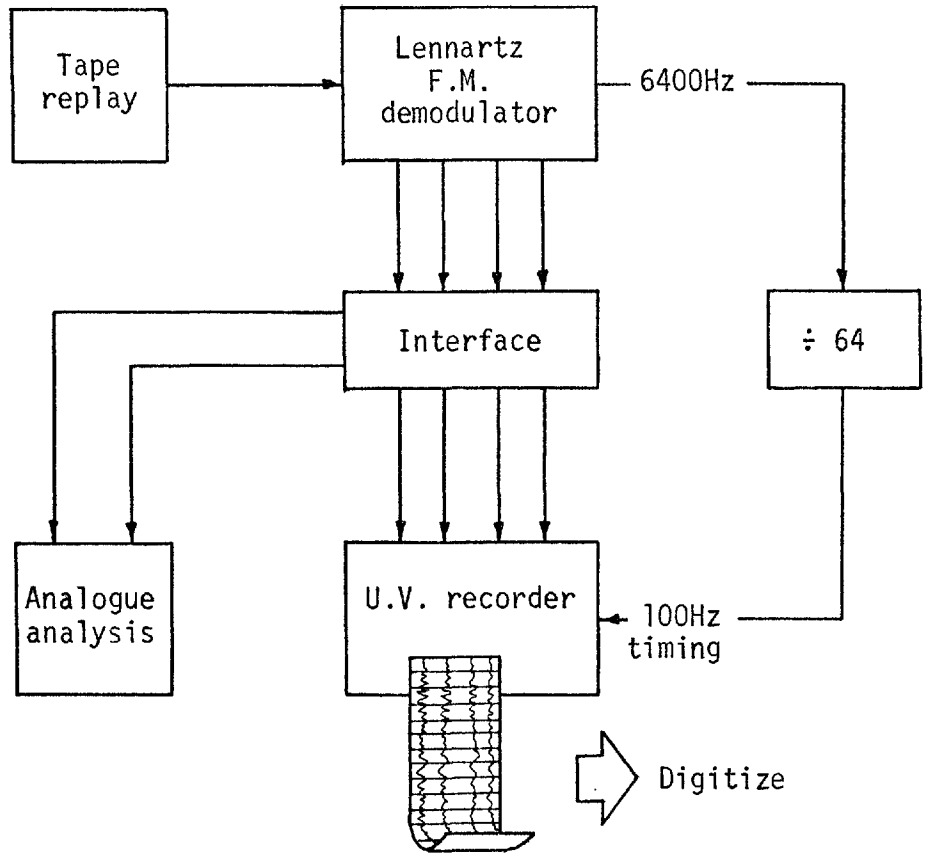


Figure 4/3 F.M. Tape replay. Schematic diagram

increased to the next higher power of two by adding zeros. If a few frequencies only are required, it is quicker to use an ordinary numerical summation to represent the Fourier integral. Spectral estimates having unacceptably high scatter can be bandwidth averaged with nearby values to produce a smoother spectrum with less resolution (operation g)).

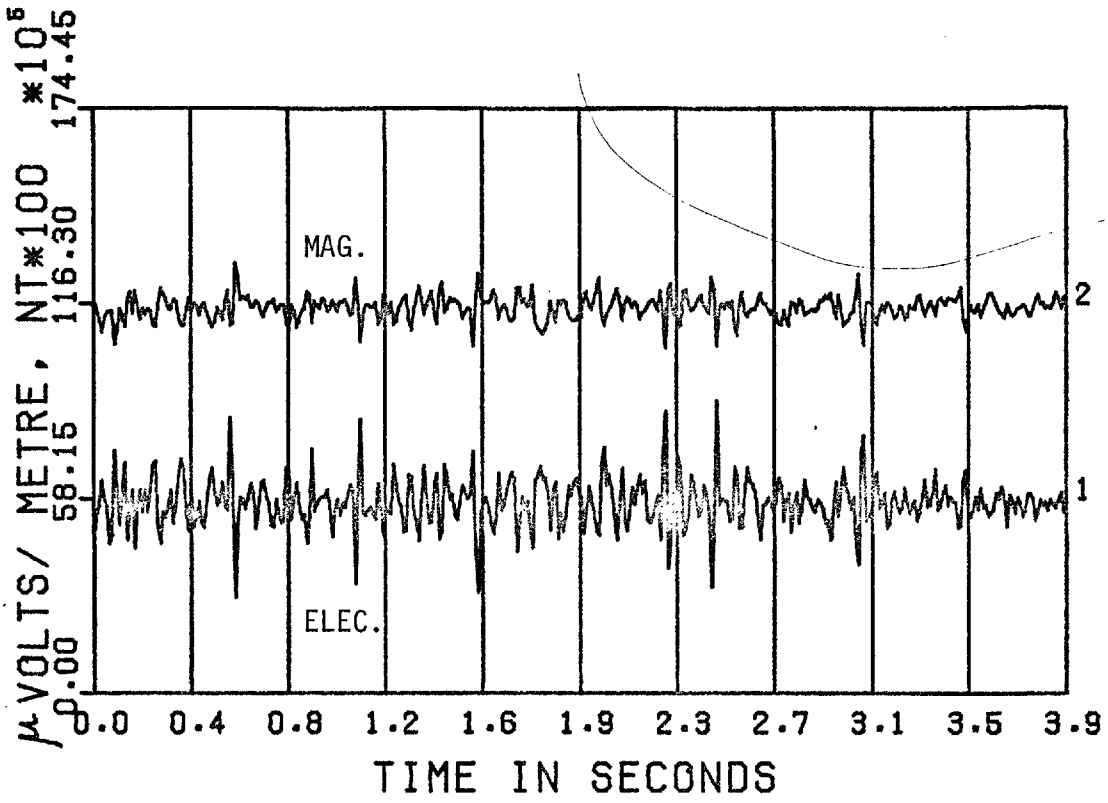
A FORTRAN program was developed to perform the above operations. A typical power spectrum is shown in Fig 4/4. The data were obtained during tests of the induction magnetometers at Keel, Co. Longford in S. Ireland in 1971. The 8Hz Schumann resonance stands out quite clearly, and correlation between the electric and magnetic orthogonal fields is excellent. This data sample was recorded with the magnetometer placed on the surface of the ground in a grassy meadow. The results demonstrate the successful performance of the magnetometer, even without burial to avoid wind noise (see Fig 6/1 for apparent resistivity and coherency calculated from these data).

4.5 Implementation of Analogue frequency analysis

In this section, analogue circuitry for amplitude and phase measurement is described. The circuits are contained in the RMS meter and Filter/Phasemeter modules which fit into the station B frame for operation in the field (see Fig 3/3(a)). The modules can equally well be used to analyze recorded data, in which case they make up the "Analogue analysis" block in Fig 4/3. A block diagram of the two modules is shown in Fig 4/5.

4.5.1 Power Spectral Estimation

The signals for comparison are first band pass filtered by a pair of active multiple feedback filters (Burr-Brown, 1968, p78), each of which has a response similar to a single series tuned LCR circuit, with a transfer function $R(\omega)$ given by



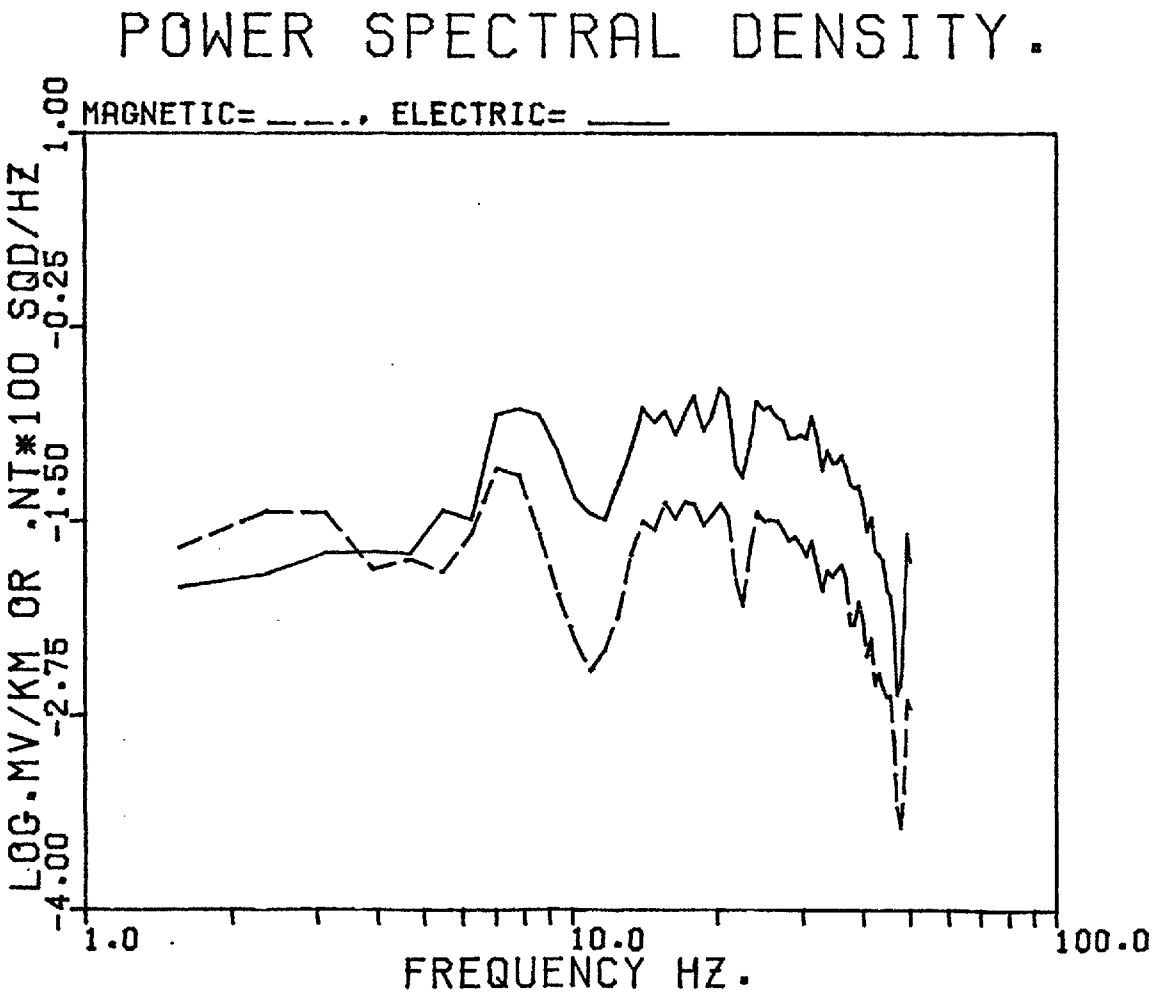


Figure 4/4 Digitized traces and power spectra for magnetotelluric data from Keel, Co.Longford (S. Ireland)

$$R(\omega) = A \left\{1 + \frac{+Q^2(\omega-\omega_o)^2}{\omega_o^2}\right\}^{1/2} \qquad 4:17$$

The Q, centre frequency ω_o and the gain A are all adjustable by changing components in the feedback network.

The full wave rectifier circuits incorporate feedback amplifiers to eliminate the small signal non linearity inherent in junction diode forward conductance (Fairchild, 1967 p 90). The rectifiers are followed by low pass filters with adjustable time constants of up to 20 seconds which can drive either a moving coil meter or an oscillograph galvanometer, to produce r.m.s. readings. Constructional details and initial setting up procedure are given in Appendix A. Readings can be taken directly from the moving coil meters, using a low pass filter time constant sufficiently long to damp out rapid fluctuations, or by measurement from chart recordings. If the signal to noise ratio is poor, the latter method can be used with a short filter time constant to allow portions of the record with high signal level to be selected.

The spectral window for this type of system is determined by the band pass filter and low pass filter characteristics. The spectral window width is inversely proportional to the Q of the band pass filter, and in the time domain the filter output, at any moment, is mainly affected by a length of input signal equal to about $\omega_o/2Q$. The effect of the output low pass filter is to average together adjacent estimates from overlapping time windows without decreasing the width of the spectral window.

4.5.2 Phase Measurement

The inputs to the phasemeter are taken from the outputs of the bandpass filters (Fig 4/5). Each

limiter consists of an integrated circuit amplifier with a gain of about 10^5, which produces a constant output of +V volts for any appreciable positive input, and -V volts for a negative input (see Figs 4/5 and 4/6). The limiter outputs drive an edge triggered bistable circuit which has an output determined by the signs of the time derivatives of the inputs. If either input is positive-going, the output stays the same, if input 1 is negative-going the output goes to (or stays at) zero volts; if input 2 is negative-going the output goes to (or stays at) +V volts. This behaviour is shown in Fig 4/6 for two sinewave inputs of period T, one with a delay τ, which produce an output consisting of a series of pulses of width τ, height V and repetition rate 1/T. These are smoothed with a low pass filter with unity DC gain and a time constant long compared with T, to produce a steady output voltage $+V\,\tau/T$. The output is thus a linear function of the delay τ over the range $T > \tau > 0$. (see Fig 4/7) and hence the phase difference ϕ is given by

$$\phi = \frac{2\pi\tau}{T} \qquad 4:18$$

The sinewaves have a cross correlation function $c(\tau)$ as shown by Fig 4/7 and given, normalized to one, by

$$c(\tau) = \cos\frac{2\pi\tau}{T} \qquad 4:19$$

The phasemeter output, normalized to the same maximum and minimum values of +1 and -1 is

$$o(\tau) = \frac{2\tau}{T} - 1 \qquad \text{for} \quad t > \tau > 0 \qquad 4:20$$

so that

$$c(\tau) = -\cos(\pi\, o(\tau)) \qquad 4:21$$

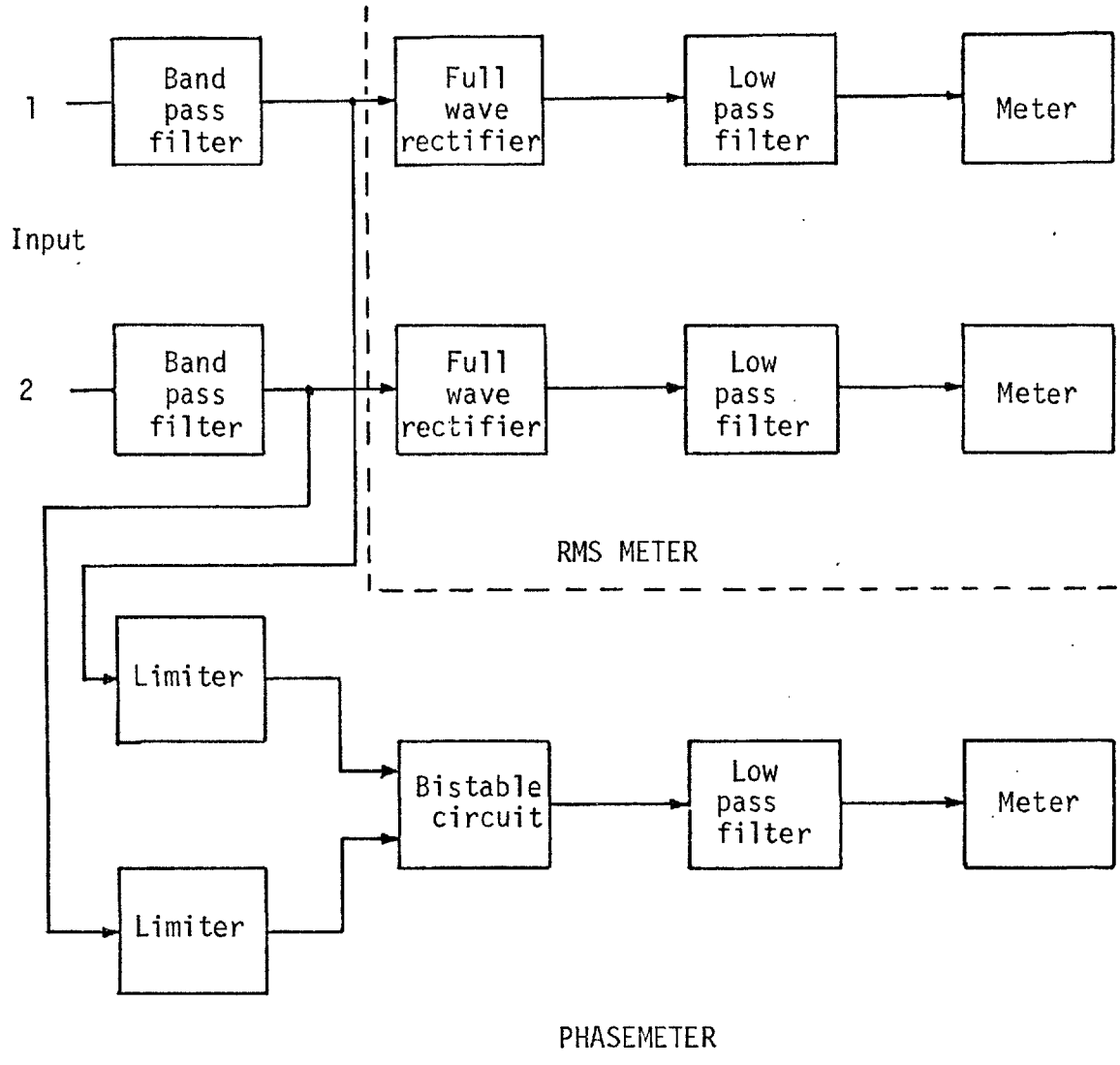


Figure 4/5 Block diagram of RMS meter and Phasemeter modules

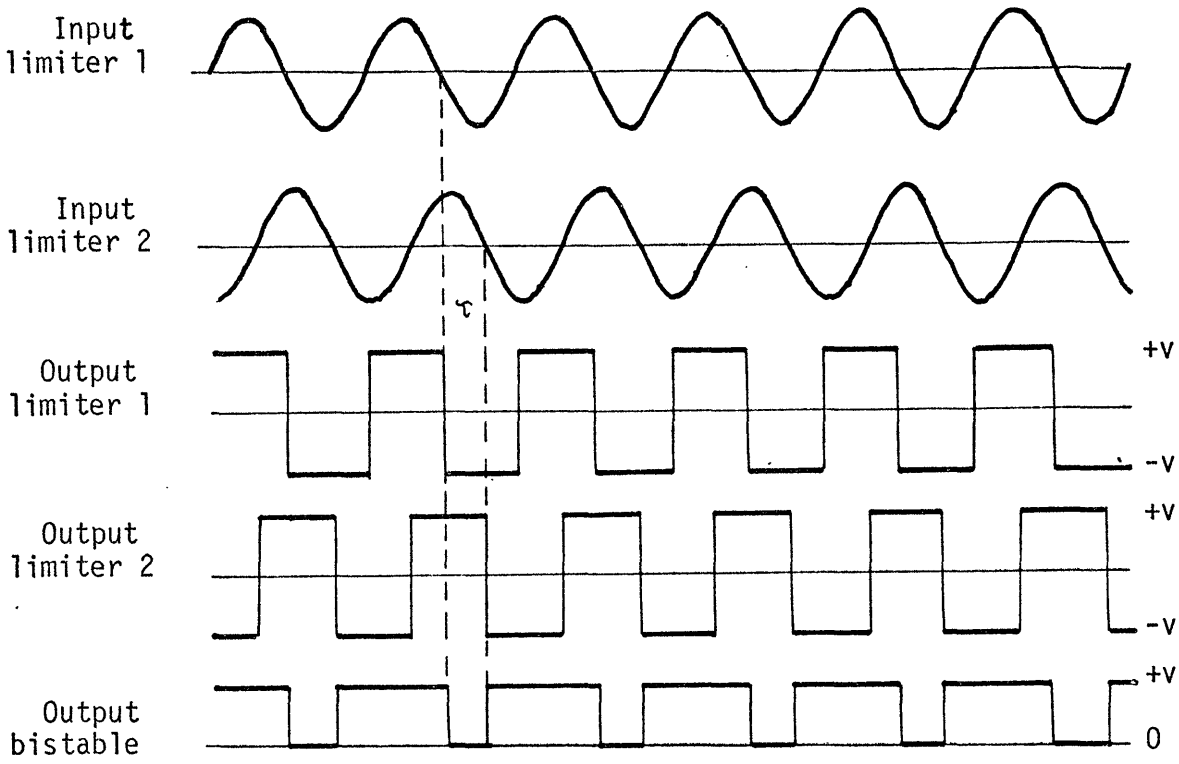


Figure 4/6 Phasemeter waveforms for sinusoidal inputs with delay τ

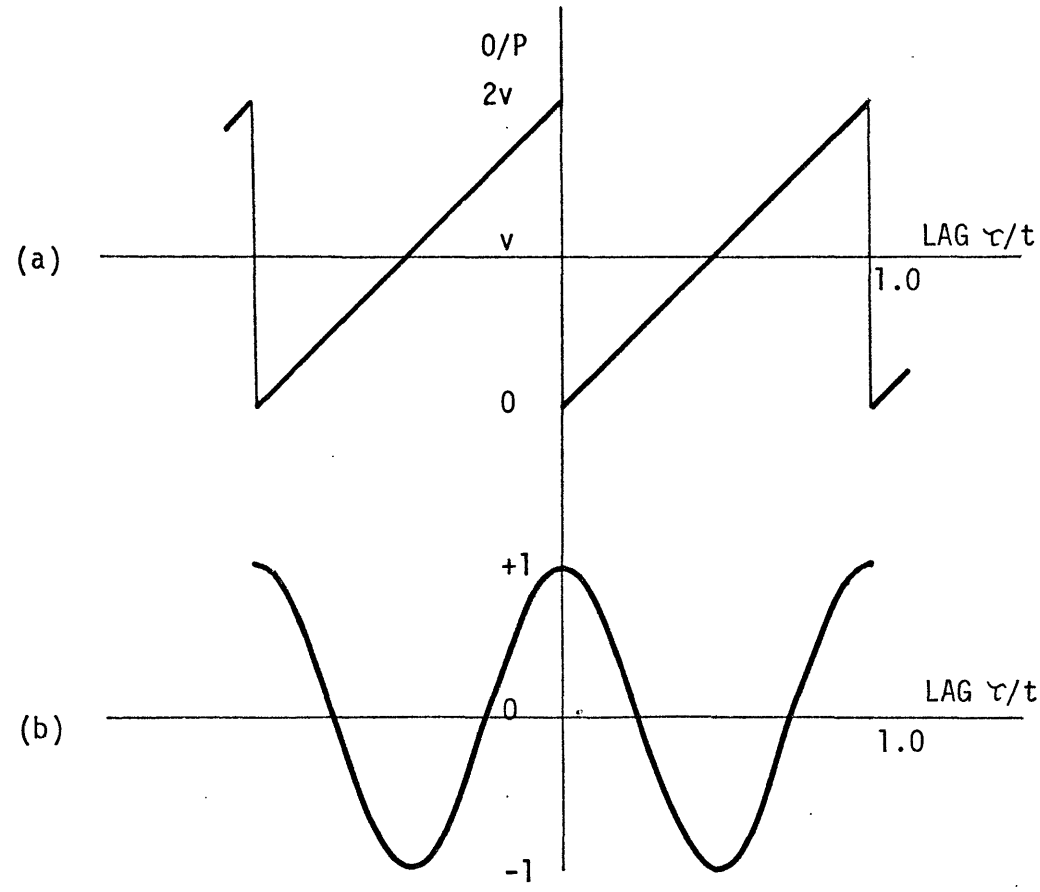


Figure 4/7 (a) Phasemeter output against lag between sinewave inputs of period t
(b) Normalized correlation function for sinewaves of period t

The normalized cross correlation function of any input waveforms can therefore be calculated from the phasemeter output provided their frequency components all have the same ratio of delay to period, τ/t, i.e. their cross phase spectrum is flat. This situation is approached if wide band waveforms are band limited so that their phase difference does not change appreciably over the pass band. The presence of uncorrelated noise at the inputs of the system will modify the output of the phase meter. The effects of such noise will be deduced (non-rigorously) in the next subsection.

4.5.3 Effects of noise on the Phasemeter

Consider two correlated random signals $s_1(t)$ and $s_2(t)$ containing uncorrelated noise $n_1(t)$ and $n_2(t)$ so that

$$F_1(\omega) = S_1(\omega) + N_1(\omega) \qquad 4:22$$

$$F_2(\omega) = S_2(\omega) + N_2(\omega)$$

where S, F and N represent Fourier transforms of the signals, filter inputs and noise respectively. The outputs $B(\omega)$ from the filters are obtained by multiplication by the filter transfer function $R(\omega)$ so that

$$B_1(\omega) = F_1(\omega)R(\omega) \qquad 4:23$$

$$B_2(\omega) = F_2(\omega)R(\omega)$$

The cross correlation function $C(\tau)$ of the output of the filters is obtained from the -j transform of the cross power spectral density

$$C(\tau) = \overline{F_1 F_2^* R R^*} \qquad 4:24$$

where the line superscript indicates -j Fourier transformation, the asterisk complex conjugation,

and the dependence on ω has been omitted for brevity. We may therefore write

$$C(\tau) = \overline{RR^*(S_1S_2^* + S_1N_2^* + N_1S_2^* + N_1S_2^*)} \qquad 4:25$$

where the cross spectral terms are estimates from finite length samples of the inputs. The bistable circuit output is affected only by the ratios of S to N at each input and not by the absolute magnitude of F_1 and F_2. In addition, the mean power output from each limiter is constant, by definition, so that if the absolute signal powers at the outputs of limiers 1 and 2 are a and b respectively, the noise powers are 1-a and 1-b respectively and the terms on the right hand side of 4:25 are present at the bistable output in the proportions shown below :

$$|RR^* S_1S_2^*| \propto ab \qquad 4:26$$

$$|RR^* S_1N_2^*| \propto a(1-b) \qquad 4:27$$

$$|RR^* N_1S_2^*| \propto b(1-a) \qquad 4:28$$

$$|RR^* N_1N_2^*| \propto (1-a)(1-b) \qquad 4:29$$

The resonant band pass response of the filters ensures that noise present in only one channel biases the phasemeter towards zero and not towards +1 or -1, because the average number of zero crossings per unit time is independent of the signal to noise ratio if signal and noise have similar statistical properties. The terms in 4:27, 4:28 and 4:29 always bias the bistable output towards zero, irrespective of the relative values of a and b. This is not the case if the statistics of the two inputs differ; in the extreme case of a sinusoidal input to limiter (1) and a white noise input to limiter (2), the bistable would be almost permanently triggered to the +1 condition because of the disparity in zero crossing rates at the limiter outputs. The effect of the signal term 4:26 on the bistable output depends on its cross

correlation function, $C_s(\tau)$, which is given by

$$C_s(\tau) = S_1 S_2^* \frac{\omega_o}{2Q} e^{-\omega_o|\tau|/2Q} \cos \omega_o \tau$$

so that with $\omega_o|\tau| \ll 2Q$

$$C_s(\tau) = \frac{\omega_o}{2Q} S_1 S_2^* \cos \omega_o \tau \qquad 4:30$$

If the cross phase spectrum of F_1 and F_2 is flat in the region of ω_o and equal to $\Phi(\omega_o)$, equation 4:30 reduces to

$$C_s(\tau) = \omega_o S_1 S_2^* \cos(\omega_o \tau + \Phi(\omega_o)) \qquad 4:31$$

Comparing this with 4:20 and applying a correction for the noise in accordance with 4:26, the output of the bistable is given by

$$O(\tau) = ab \left\{ \frac{2\tau\omega_o + \Phi}{2\pi} - 1 \right\} \qquad 4:32$$

where $$\frac{2\tau\omega_o + \Phi}{2\pi} < 2$$

With no delay τ between the inputs we have

$$O_1 = O(0) = ab \left\{ \frac{\Phi}{2\pi} - 1 \right\} \qquad 4:33$$

Inverting one input simply introduces π phase shift at all frequencies so that

$$O_2 = O(1/(2\omega_o)) = ab \left\{ \frac{\Phi}{2\pi} \right\} \qquad 4:34$$

O_1 and O_2 , the bistable outputs with zero and π shift, can be measured with a suitable output filter

time constant and equations 4:33 and 4:34 solved for ab and ϕ, giving

$$\phi = \frac{2\pi O_2}{O_1 - O_2} \qquad 4:35$$

$$ab = O_1 - O_2 \qquad 4:36$$

4.5.4 Phasemeter tests

For well correlated inputs, ab ≈ 1, so that the modulus of $O_1 - O_2$ should be close to 1 for all phase shifts, if the filter Q is sufficiently large. Fig 4/8 shows the results of measuring $|O_1 - O_2|$ at different phase shifts. The minima at $0, \pi$ and 2π phase shift are due to spurious triggering of the bistable by slight zero crossing errors, which have a disproportionate effect at small phase shifts. The dead regions are decreased in width as the Q increases. Experiments were performed with noise introduced into the inputs, to produce curves as in Fig 4/9. It was found that reliable phase estimates could be obtained for $ab > 0.4$ if the phase shift lay within $\pm \pi/4$ of $\pi/2$ or $3\pi/2$ (see dotted lines on Fig 4/9). This limitation is not as serious as it sounds, because a known (artificial) phase shift can always be introduced to bring the total phase shift into one of these ranges. The overall accuracy depends on the time constant of the low pass output filter and the precision of the output meter (or U.V. Galvonometer).

Tests with sinusoidal inputs indicated that the maximum accuracy for high signal to noise ratios was about $\pm 3.6^\circ$ (1% of full scale meter deflection). The standard deviations for random inputs with high signal to noise ratio were also of this order.

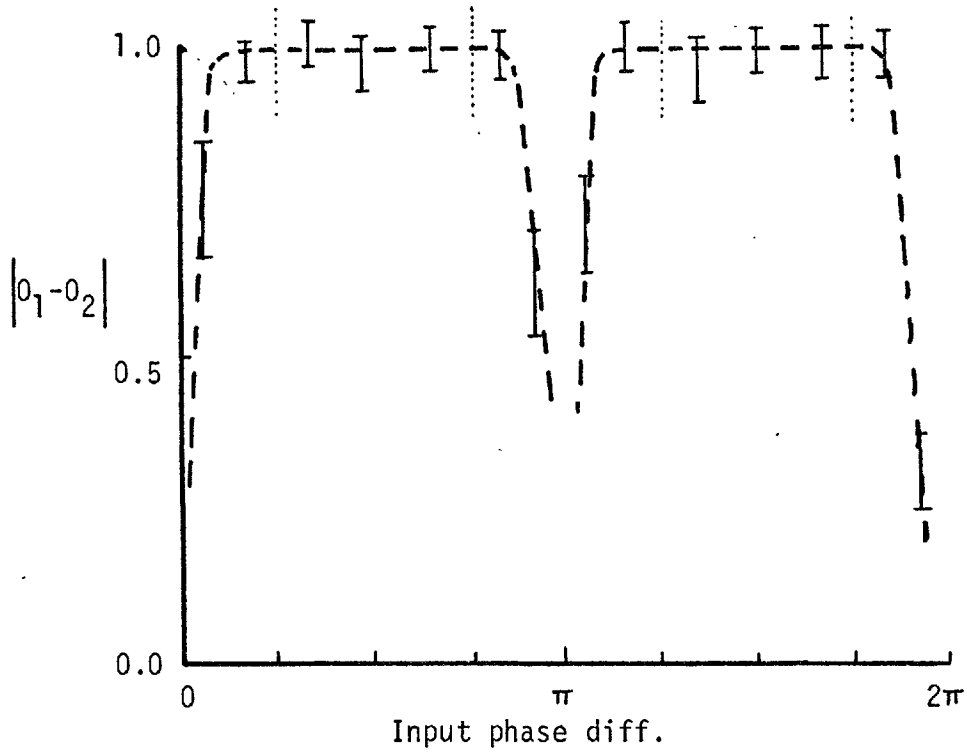


Figure 4/8 Difference between zero and π shifted phasemeter readings for correlated random inputs

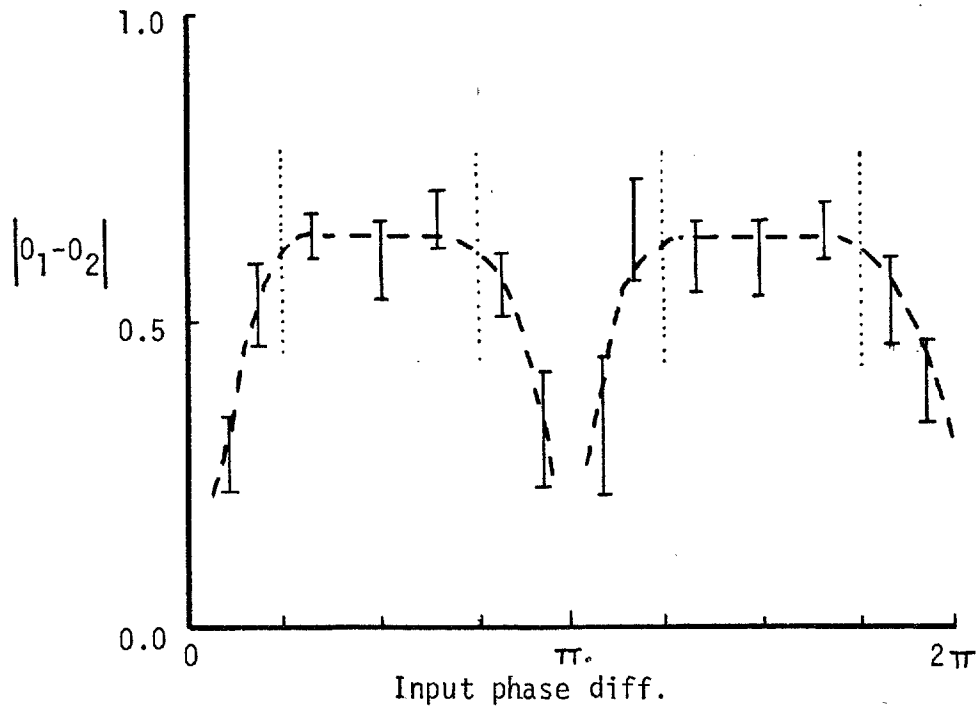


Figure 4/9 Difference between zero and π shifted phasemeter readings for noisy correlated random inputs

CHAPTER 5

TELLURIC TRAVERSES AT SOURTON TOR

5.1 Sourton Tor test site

A test site was selected for equipment trials at Sourton Tor, on the north-western boundary of the Dartmoor Granite in SW England (National Grid reference SX 543898). A strong magnetic anomaly near the tor was investigated by the Institute of Geological Sciences in 1963, using horizontal loop electromagnetic, Self Potential and induced polarization methods (Fenning 1964). These revealed a zone of anomalously high conductivity striking NE-SW, approximately parallel to the granite contact. A test borehole at the peak of the EM anomaly (about halfway along line A12a in Fig 5/1) and several others to the NE (see Fig 5/3) disclosed that the high conductivity was due to pyrrhotite, present as an interlacing network of fracture fillings, notably in the Crakington Formation mudstones. (Beer, 1966). Uneconomic traces of chalcopyrite and sphalerite were also present. The deepest borehole, ST-1, reached a depth of about 60m (200'), where the mineralization was beginning to die out; it is possible, however, that mineralization is present at much greater depths, as is often the case with mineral deposits in the metamorphic aureoles of the granites of SW England (Edmonds et al. 1969, p 89).

Three traverses were marked out with bamboo canes at 30.48m (100') intervals. Each traverse comprised two rows of canes, which marked the positions of the porous pot electrodes for the different stations. Traverses A12 and A2 corresponded with those used by IGS in 1963 but were extended 183m (600') and 91m (300') towards the SE respectively (see Fig 5/1). The third traverse A12a, was 91m (300') to the SW of A12. The base station (station A) was invariably

set up at station 1 on traverse A12, with an electrode 30.5m (100') to the NW (channel 1) and an electrode 30.5m (100') to the SW (channel 2), a common electrode being at the apex of the "L". The roving station (station B) had a similar configuration with NW and SW electrodes connected to channels 3 and 4 respectively (see Fig 5/2).

The field components are designated as follows :

Ex	Channel 1	Base	NW	component
Ey	Channel 2	Base	SW	component
Eu	Channel 3	Roving	NW	component
Ev	Channel 4	Roving	SW	component

5.2 Analogue Measurements

At the roving station, simultaneous readings were taken of the r.m.s. amplitudes of Ex and Eu, and of Ey and Ev, using the circuitry described in section 4.5 Phase measurements were also attempted, but abandoned because they made progress very slow and caused problems with excessive battery drain. (This fault has since been remedied). A 1 to 2 minute recording of all four components was made at each position, so that the phases could be determined later. The poor weather and the vulnerability of the electronics to moisture made measurements difficult but, under the circumstances, the amplifying and recording part of the equipment functioned satisfactorily. An unexpected problem arose with high frequency interference saturating the roving station preamplifiers. These were an earlier design than those described in subsection 2.5.3. and had a flat response up to about 30kHz. The problem was solved, at the expense of gain accuracy, by fitting low pass filters to the inputs of the preamplifiers.

The results of the readings taken in the field are shown in Fig 5/4, in which the ratios of Eu/Ex and

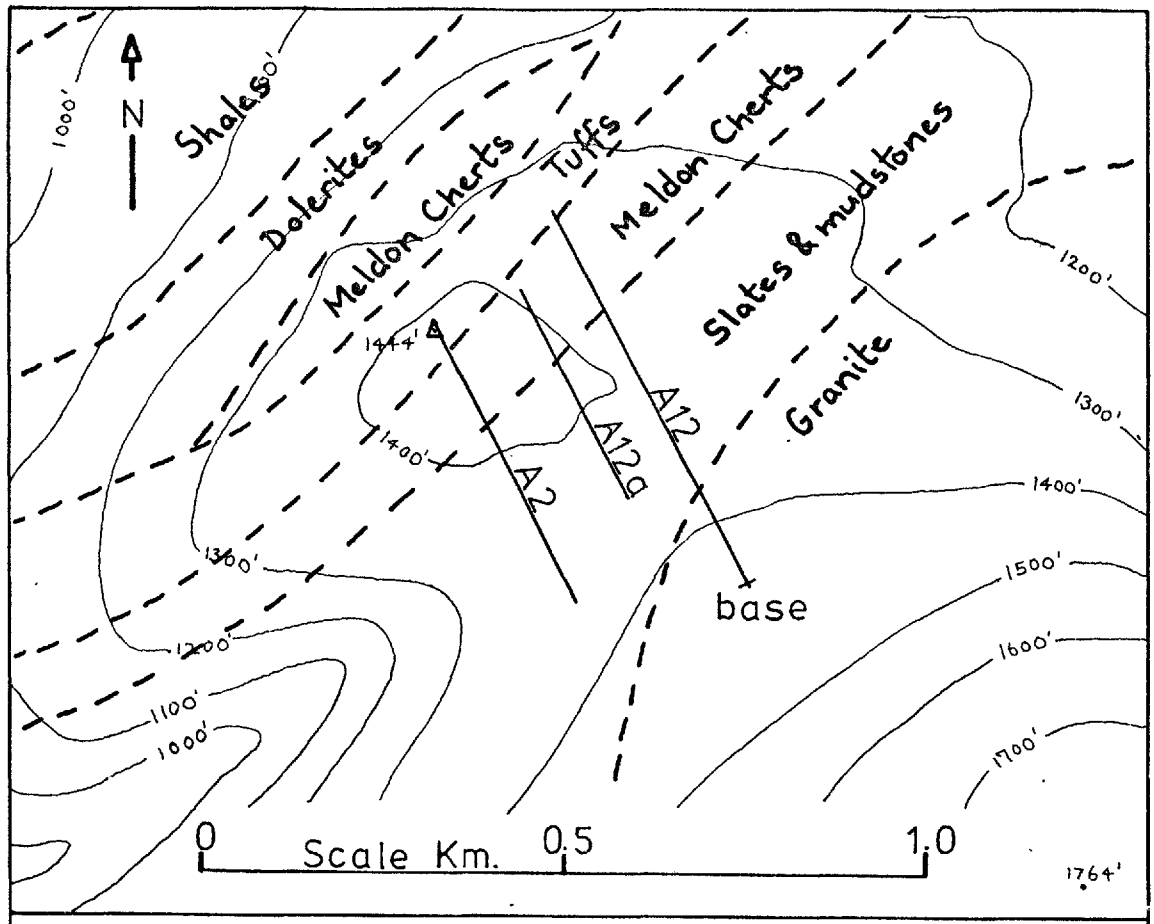


Figure 5/1 The area around Sourton Tor triangulation point, showing geology and traverse lines.

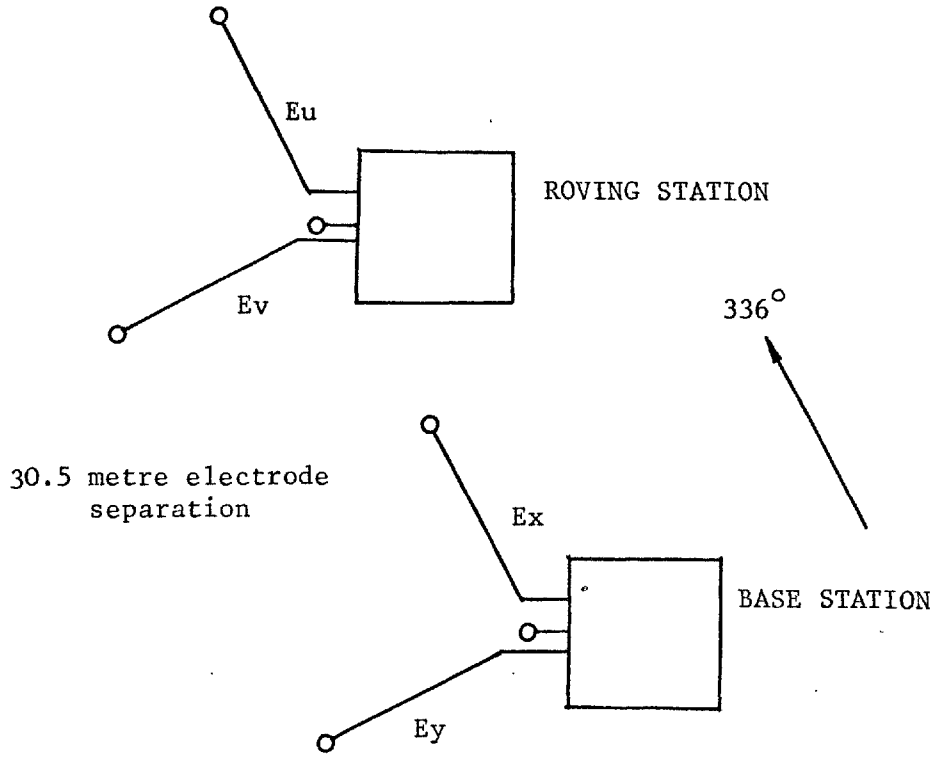


Figure 5/2 Electrode configuration

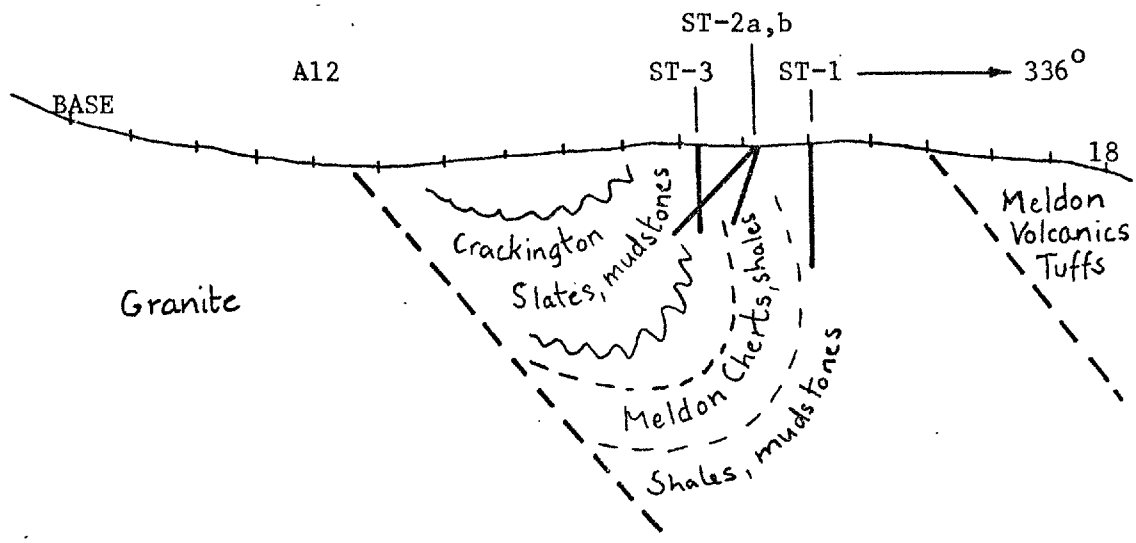


Figure 5/3 Sketched section through line A12, looking SW, showing IGS boreholes St-1, 2a, 2b, 3.

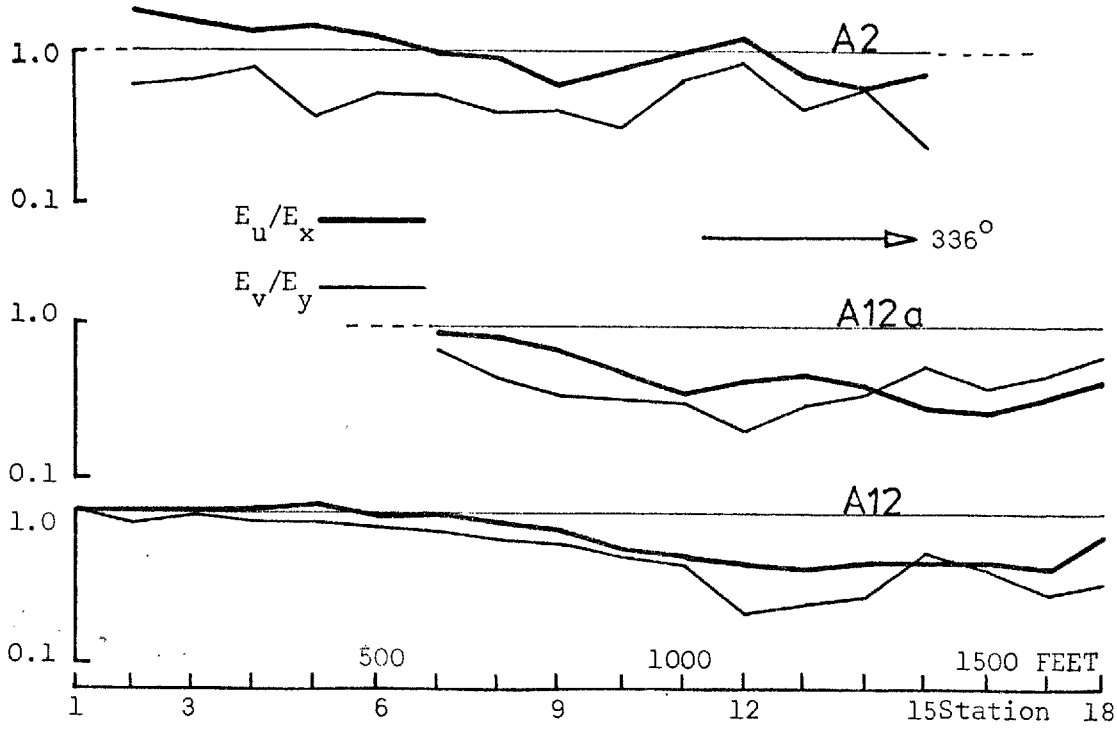


Figure 5/4 8Hz amplitude ratios, measured in the field

Ev/Ey at 8Hz are plotted for the 3 traverses. Readings were taken with the roving station at the base position before and after each traverse so that allowances could be made for differences in gain between the channels and their responses normalized to the base station. The minima in the amplitude ratio Ev/Ey at 1100' on traverses A12 and A12a correspond with the positions of test boreholes sunk by IGS over the maxima in their horizontal loop EM and SP profiles. The ratio Eu/Ex shows a less well defined minimum, again in the region of stations 12-17.

These results are best illustrated by Figs 5/9 and 5/10 which show the appearance of the electric field components at stations 7 and 12 compared with simultaneous base fields. The marked reduction of the amplitude of the roving components from stations 7 to 12 can clearly be seen.

The field recordings made along A12, the longest line, were analyzed in the laboratory using the analogue equipment described in section 4.5. The outputs from the RMS meters and the phasemeter for both parallel pairs of fields were recorded on U.V. oscillograph charts using filter frequencies of 8, 14 and 32Hz. A second chart was made at each frequency with the phasemeter at the π shift setting. The time constant of the low pass filters on the phasemeter and RMS meter outputs were set to 2.5 seconds so that only the longer bursts of signal were resolved. The amplitude of each trace was measured over the last 20 seconds of the recording, at 1 second intervals to give 20 estimates of the amplitude ratio and phase at each frequency for each station along the line. The averages for each set of 20 measurements are plotted in Figs 5/5 5/6, 5/7 and 5/8, with error bars representing standard deviations.

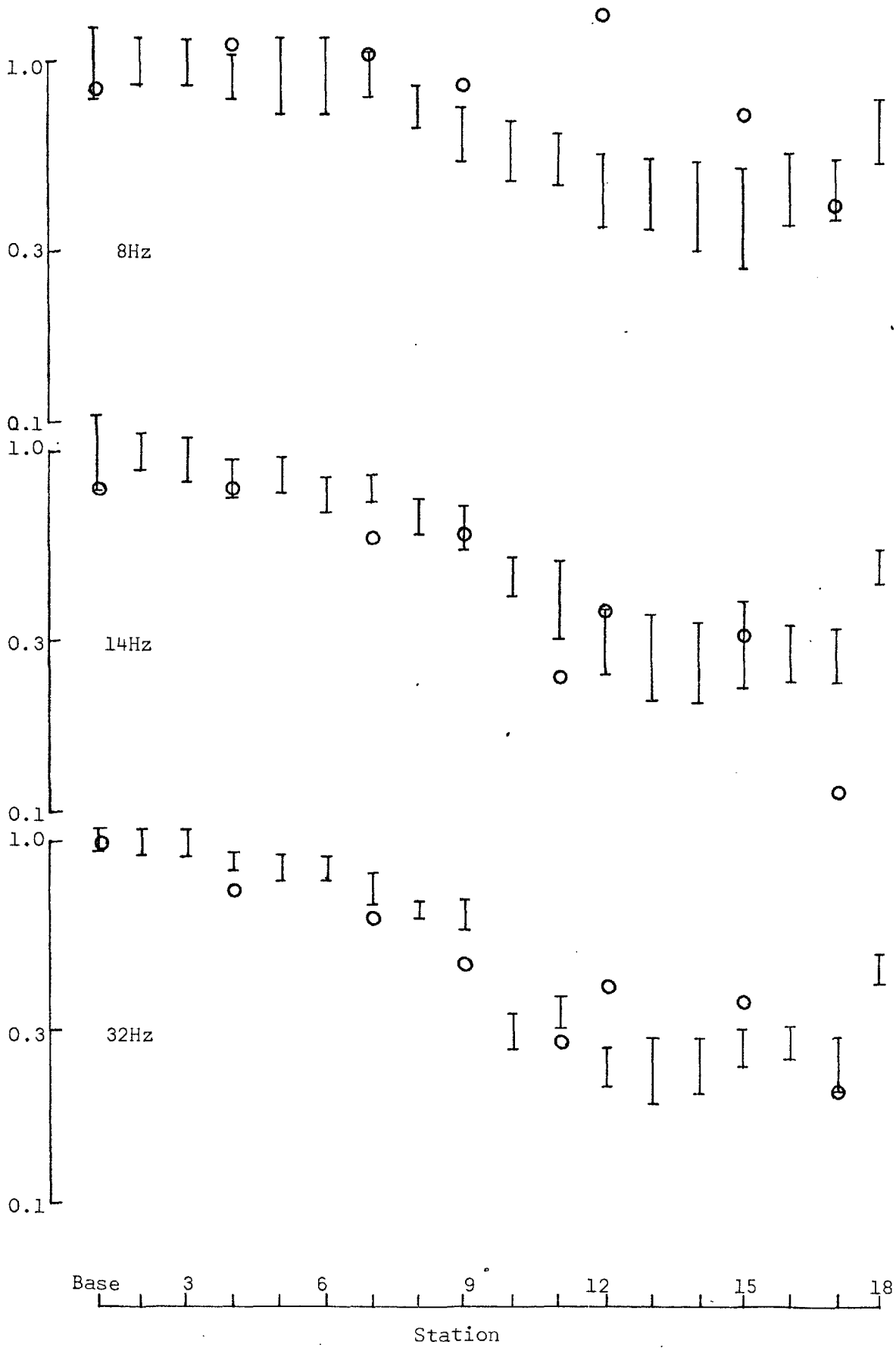


Figure 5/5 Line A12 Amplitude ratio, NW component

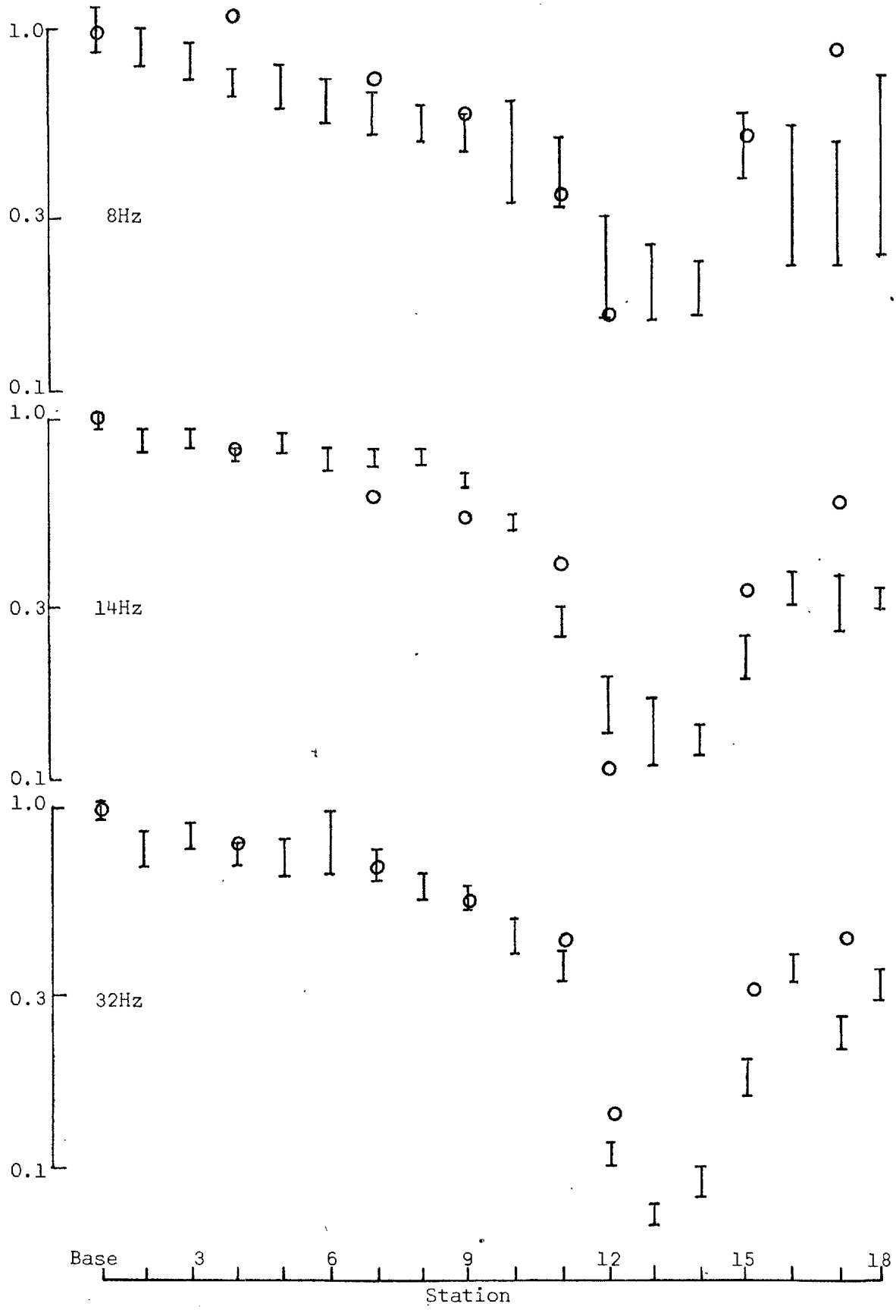


Figure 5/6 Line A/12 Amplitude ratio, SW component

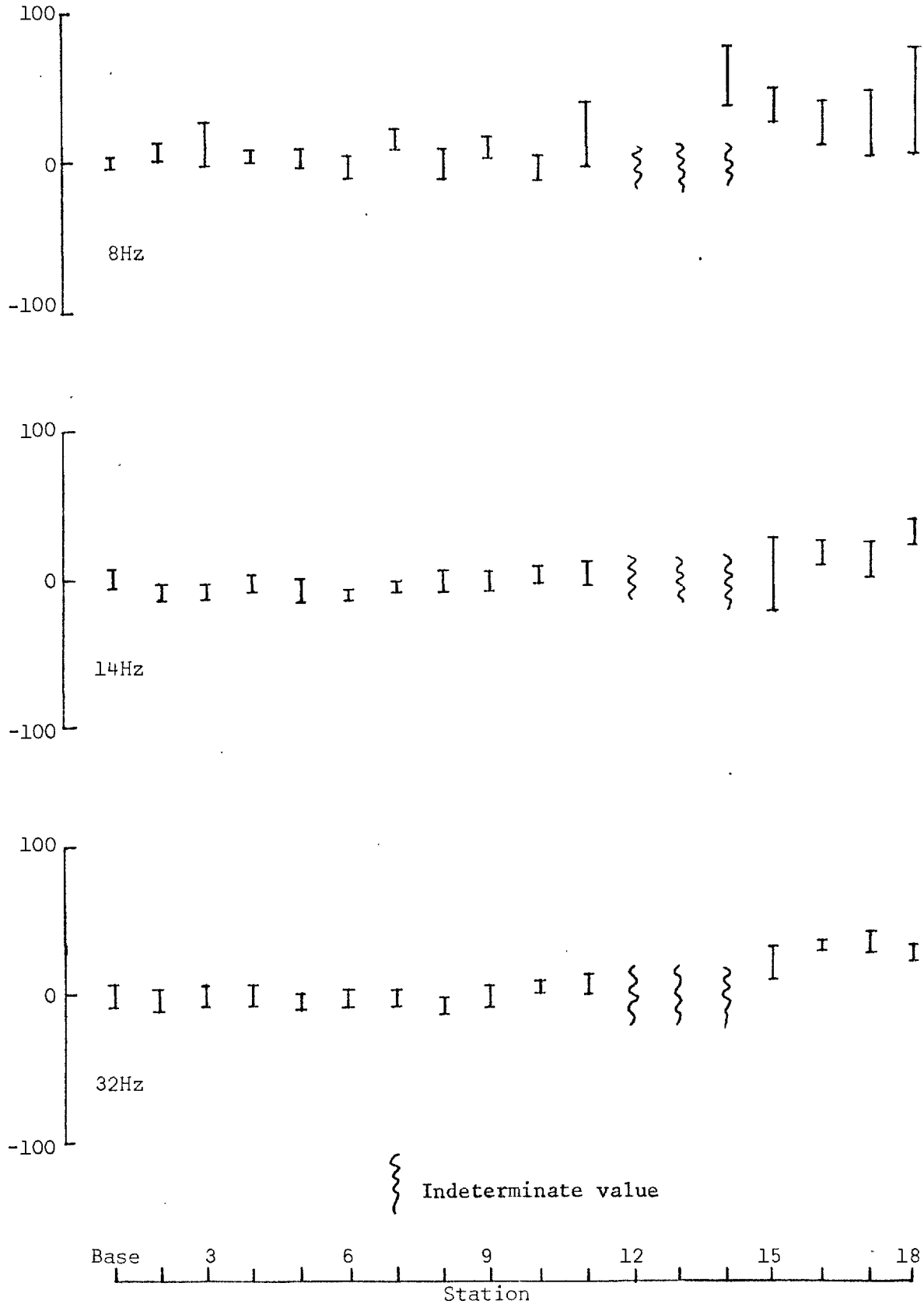


Figure 5/7 Line A12 Phase NW components

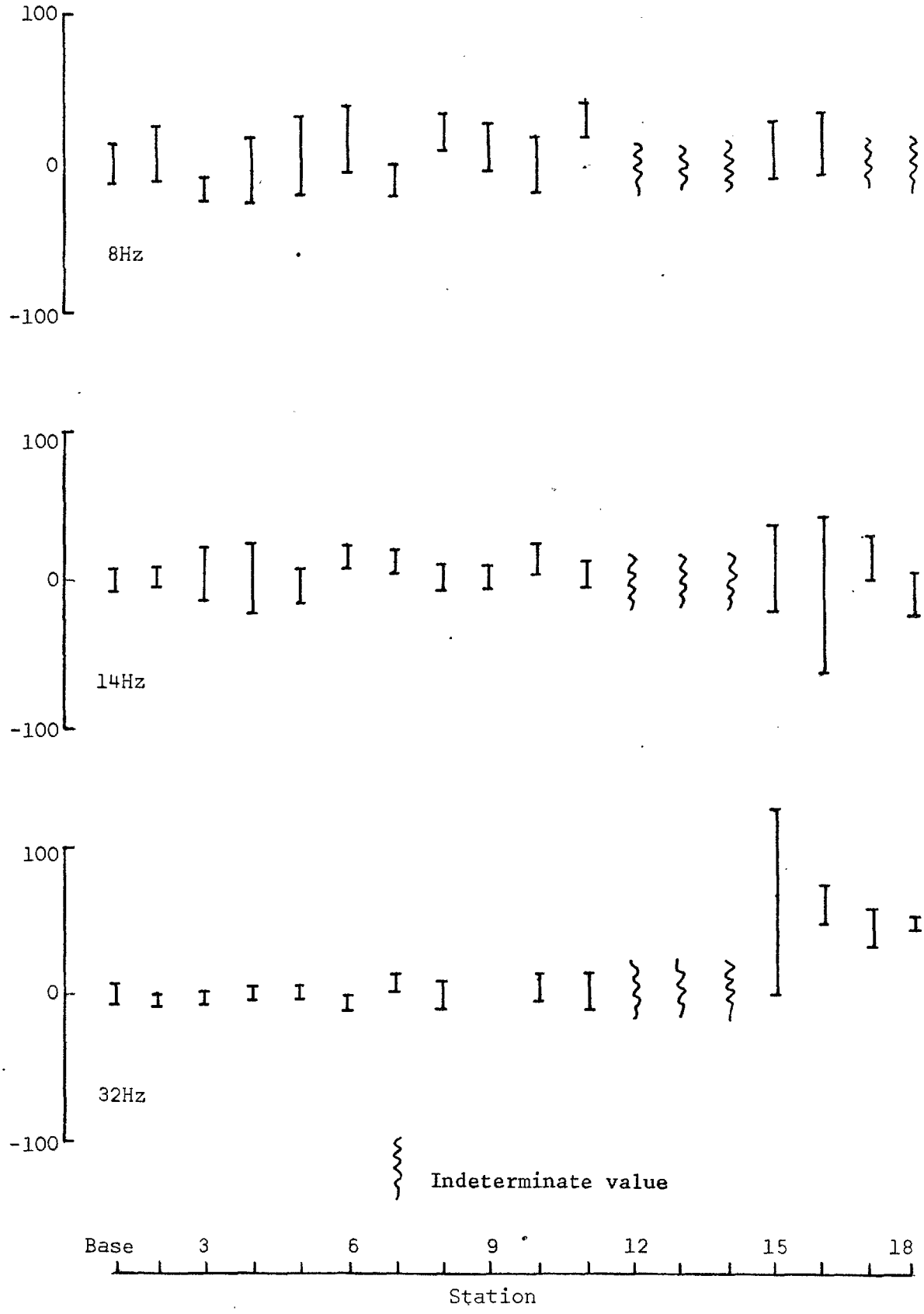


Figure 5/8 Phase SW components

The 8Hz amplitude ratios agree quite well with those obtained in the field by direct measurement and show a minimum in the region of station 12. In both cases the anomaly is most marked for Ev/Ey and the general shapes of the profiles agree. At the higher frequencies, the anomaly is enhanced, with a minimum ratio of .06 for Ev/Ey at 32Hz.

The phase measurements are scattered, and show little evidence of significant phase shifts between stations 1-11, and the signal to noise ratio was generally too low to obtain useable estimates for stations 12, 13 and 14. At stations 15, 16, 17 and 18, however, there is a consistent but scattered lag of both Eu and Ev relative to the base station.

One feature of the results is that the reduction in amplitude of Eu at stations 12-15 is less than that for Ev (see Fig 5/10). This is due to an abnormally high Eu preamplifier noise level caused by the modifications mentioned at the beginning of this section. Measurements on the noise showed it to be inversely proportional to frequency, so that the 8Hz results are more in error than those at 32Hz. The noise probably also accounts for the large scatter of the Ex-Eu phase (Fig 5/8).

5.3 Digital Analysis

The lack of proper digitizing equipment severely curtailed the length of record that could be processed by digital methods. Two second sections were chosen for digitization from the recordings made at stations 1, 4, 7, 9, 11, 12, 15 and 17. Typical sections are shown in Figs 5/9 and 5/10 and their corresponding power and phase spectra in Figs 5/11, 5/12, 5/13 and 5/14. The amplitude ratios of the parallel components, calculated by taking the square root of their power ratios at the

appropriate frequency, are plotted on Figs 5/5 and 5/6, for comparison with the analogue results. The scatter of the digital results is large because of the brevity of the digitized sections, to the extent that the enhancement of the anomaly at the higher frequencies is not as obvious as in the analogue results. The plotted points were chosen from the print-outs on the basis of their power content. At each frequency the plotted value corresponds to the highest cross power spectral density in the region of that frequency. It is difficult to assign errors to these values, but it is fairly certain that the accuracy is less than that for the analogue method, and that the results would be considerably improved if longer digitized sections were available. The scatter in the phase results is large enough to mask any trends; the phases have not, therefore, been plotted. A typical computer print-out of digital results is shown in Fig 5/15. The high cross power values in the region of 8, 14 and 32Hz are underlined.

Attempts were also made to produce telluric tensor estimates from the digitized sections, using the equations shown in Figs 4/2(a) and 4/2(b). The scatter on the estimates was very high, for three main reasons :

a) Insufficient record length
b) Insufficiently random polarization over the records
c) Excessive noise on the Eu amplifier channel

A small portion of a typical print-out is shown in Fig 5/16. When the tensors were rotated, the principal directions varied randomly from one frequency to the next.

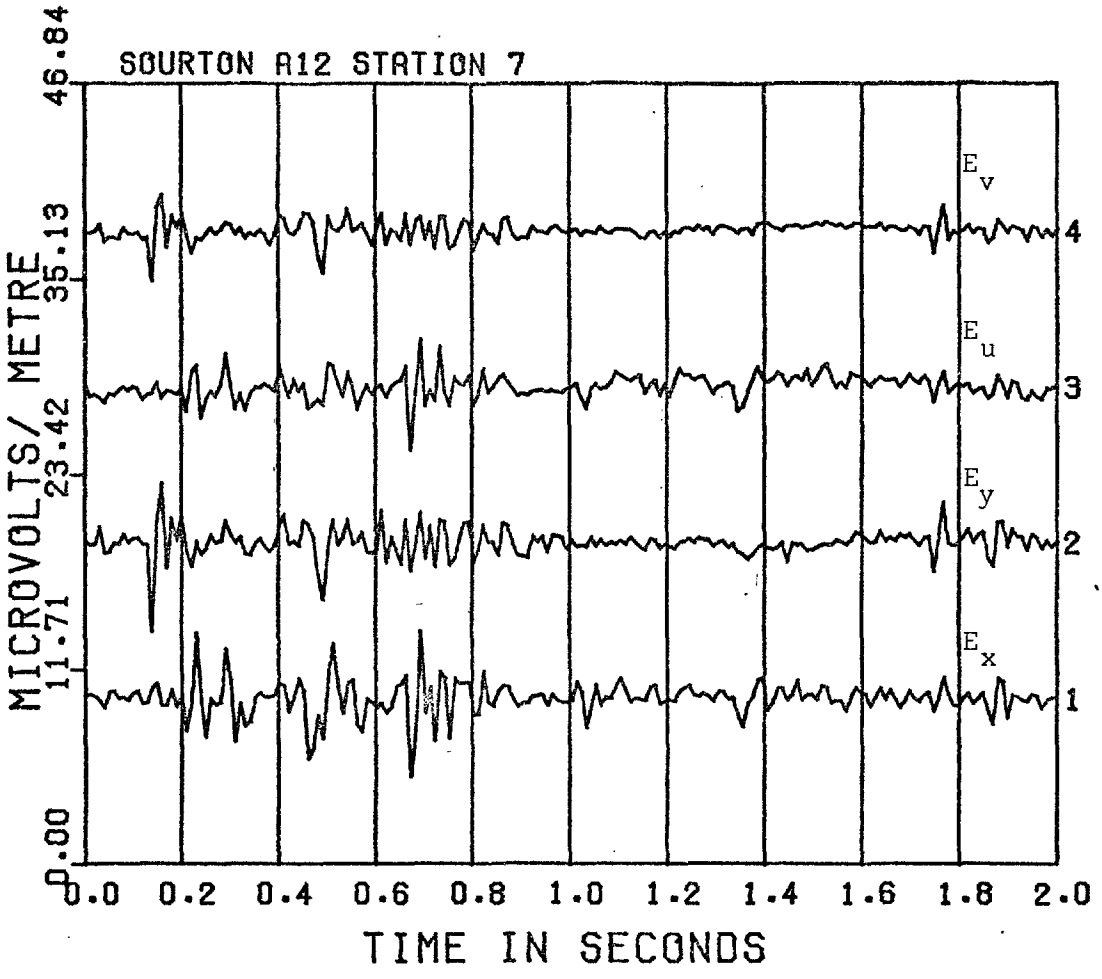


Figure 5/9 Digitized section of recording at Station 7

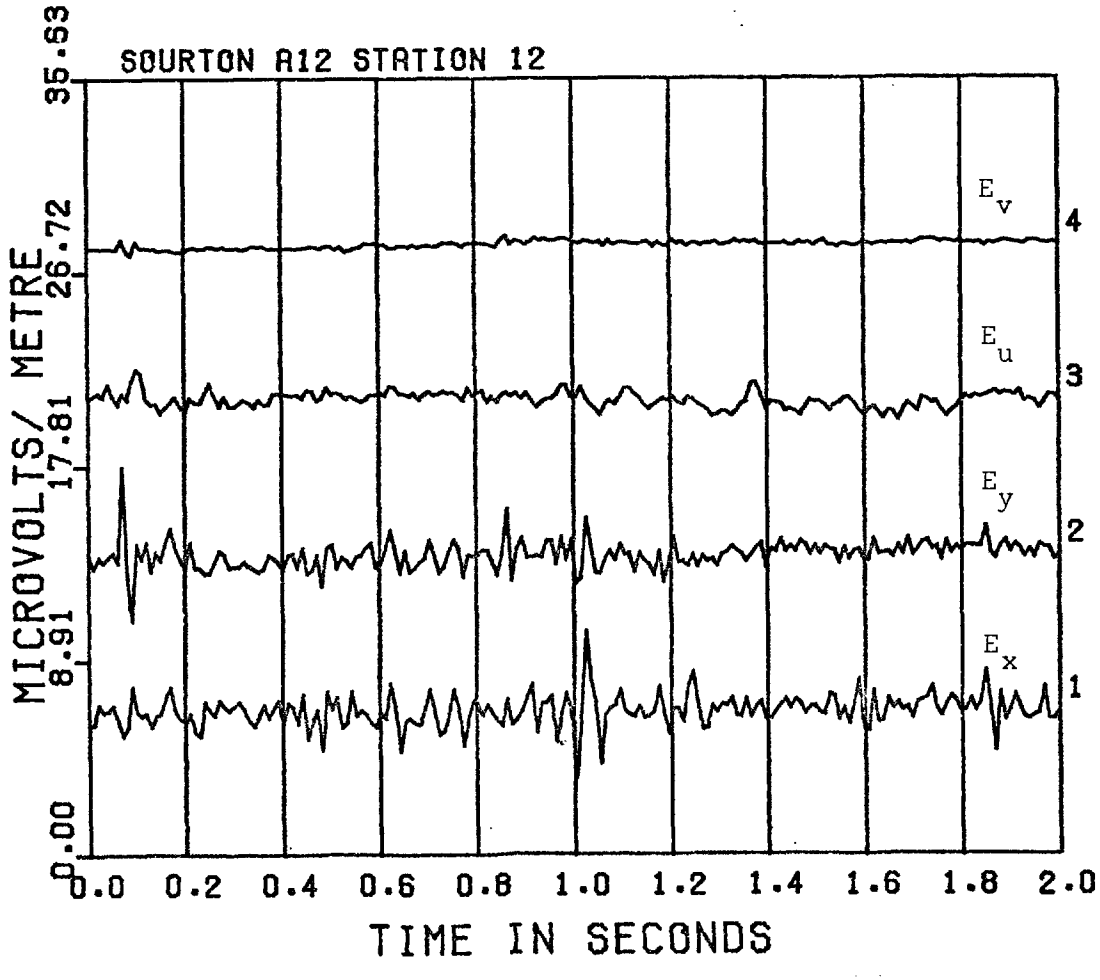
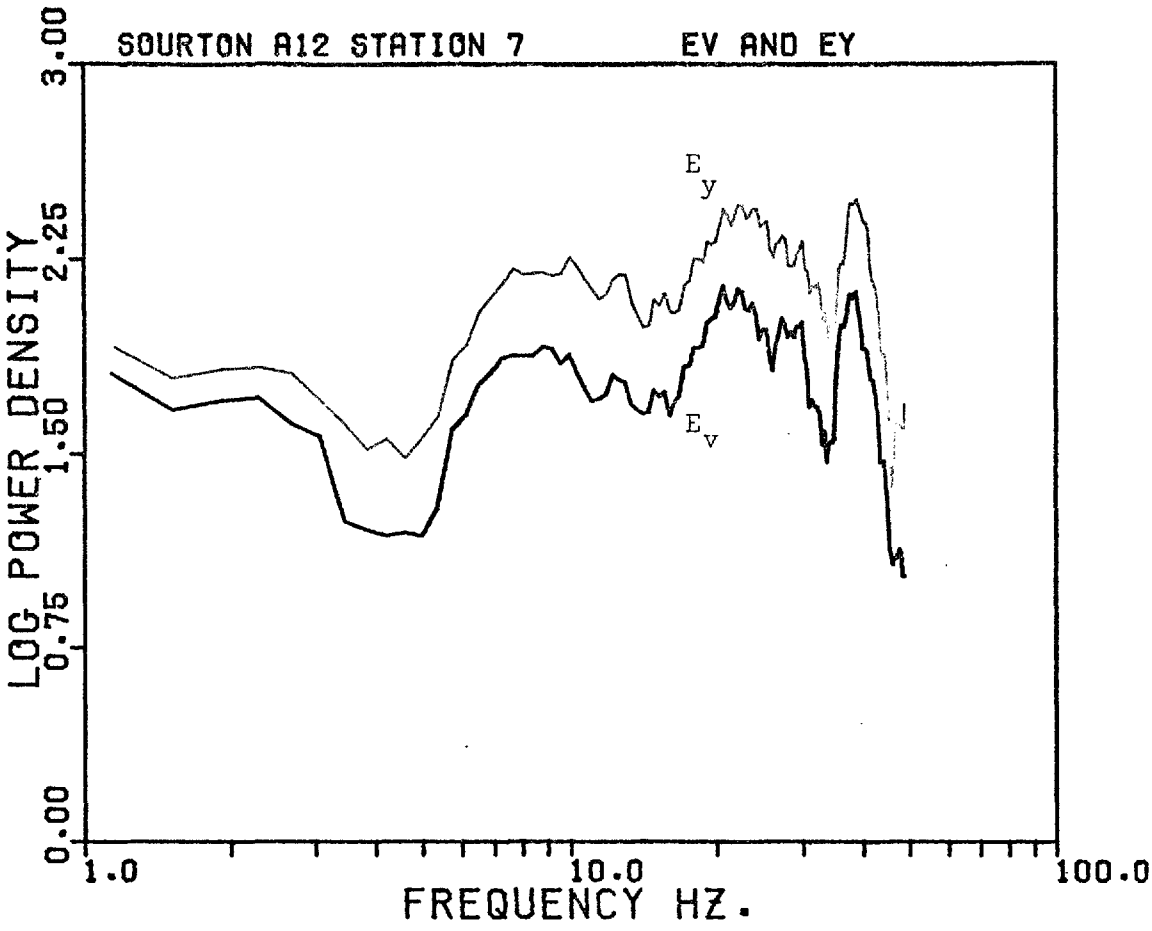


Figure 5/10 Digitized section of recording at Station 12

POWER SPECTRAL DENSITY.



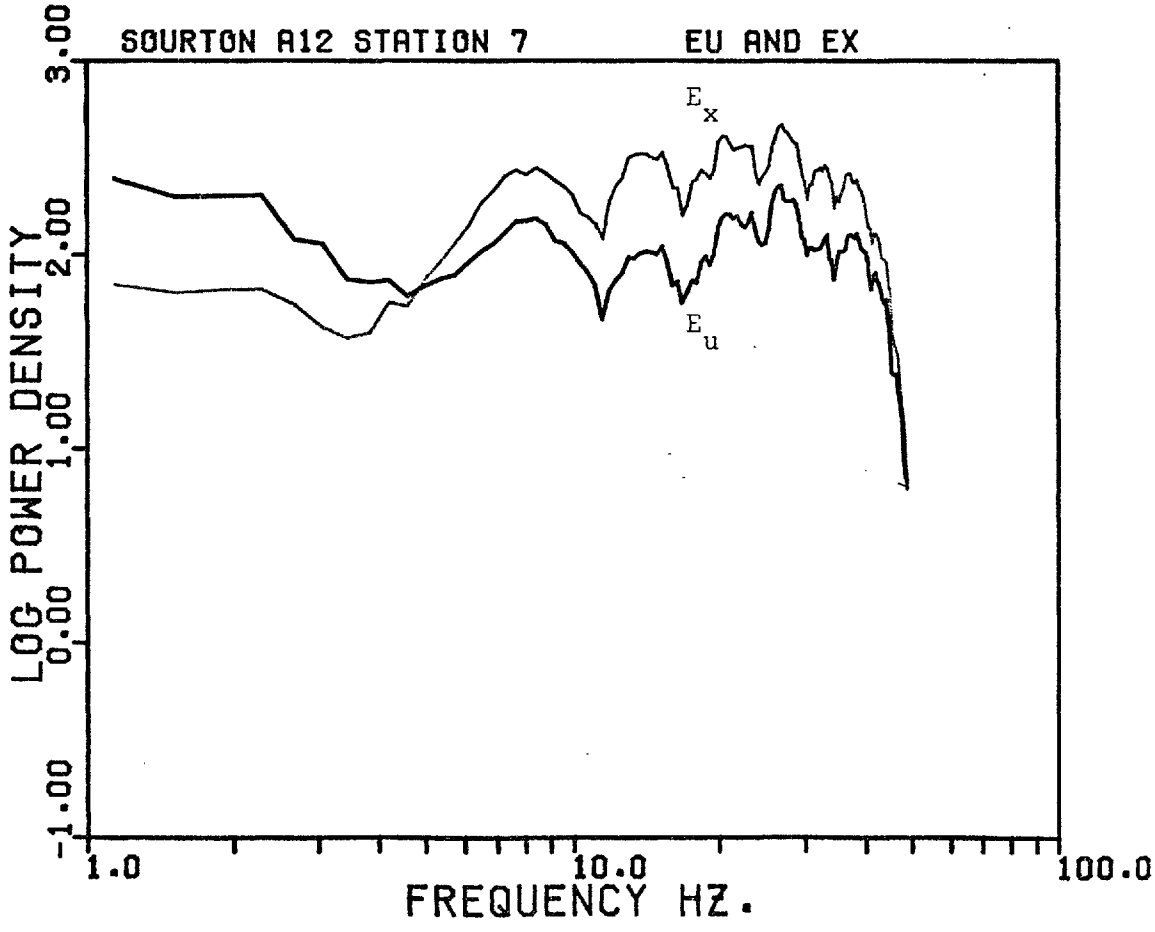


Figure 5/11 Station 7 Power Spectral densities

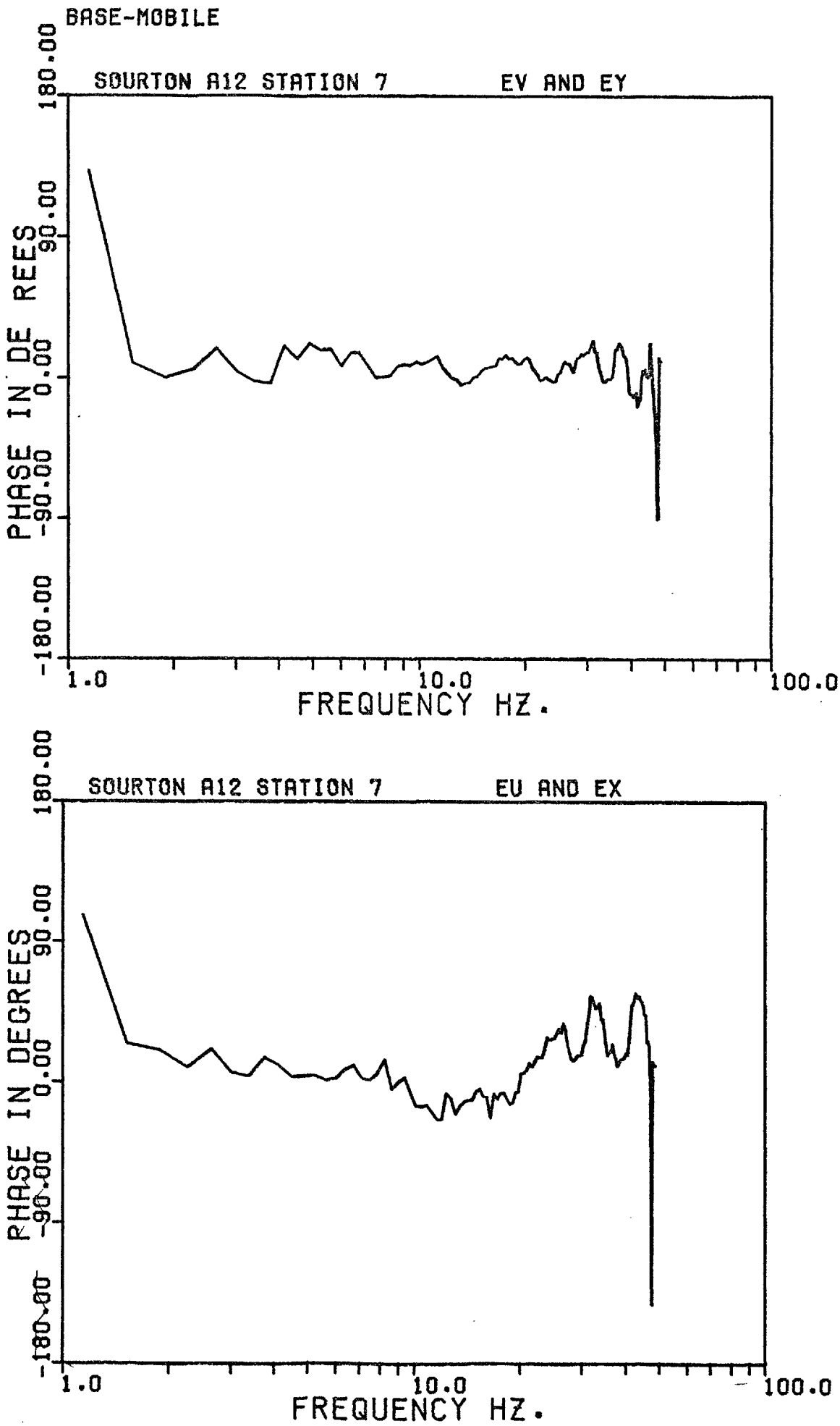
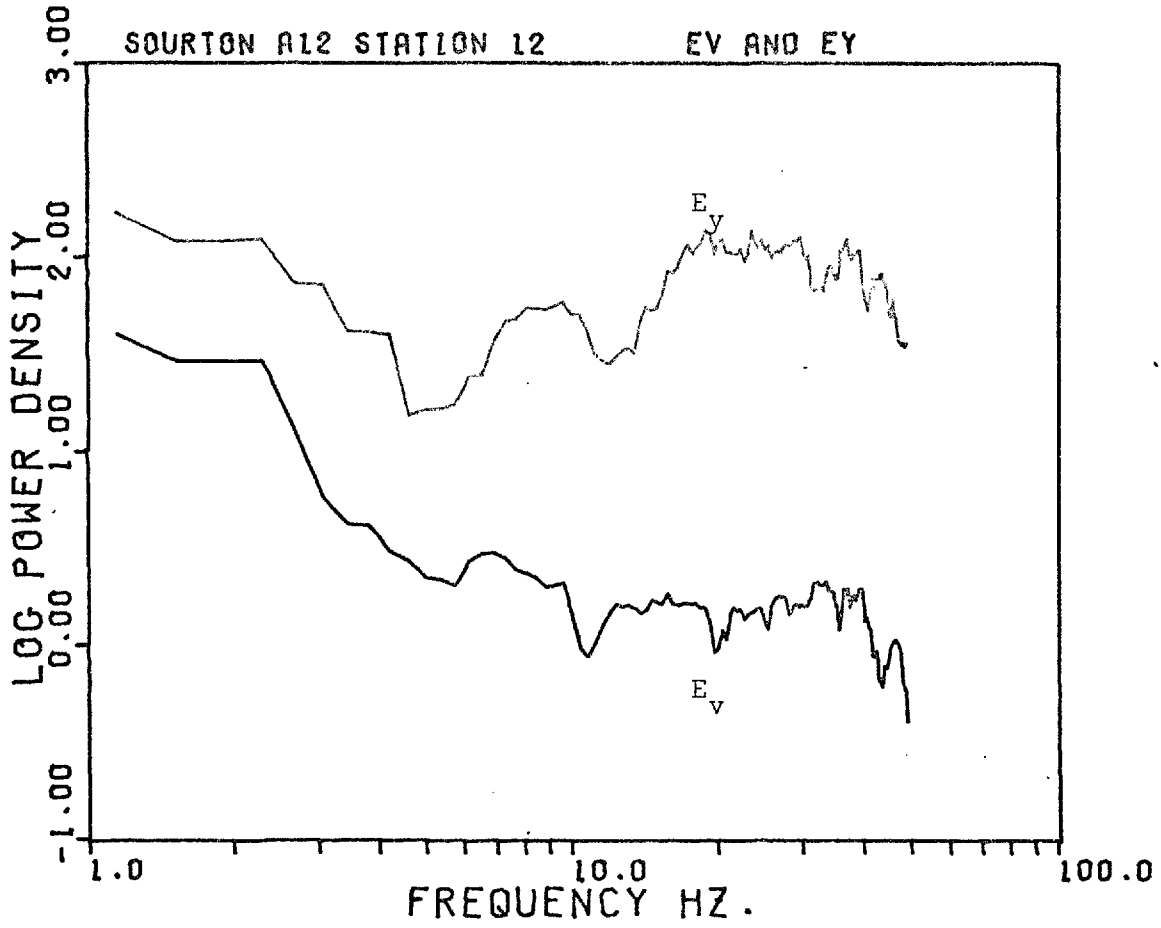


Figure 5/12 Station 7 cross phase spectra

POWER SPECTRAL DENSITY.



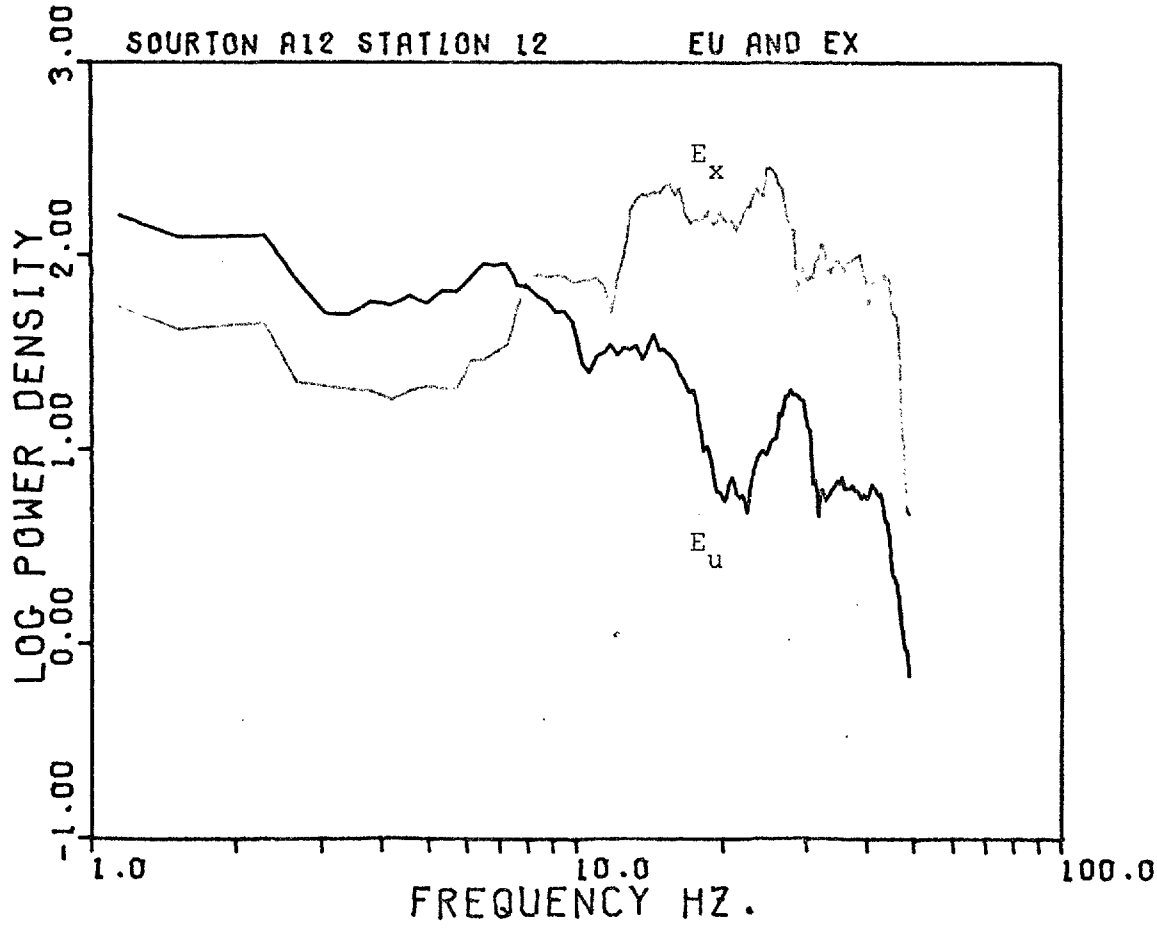


Figure 5/13 Station 12 Power spectral densities

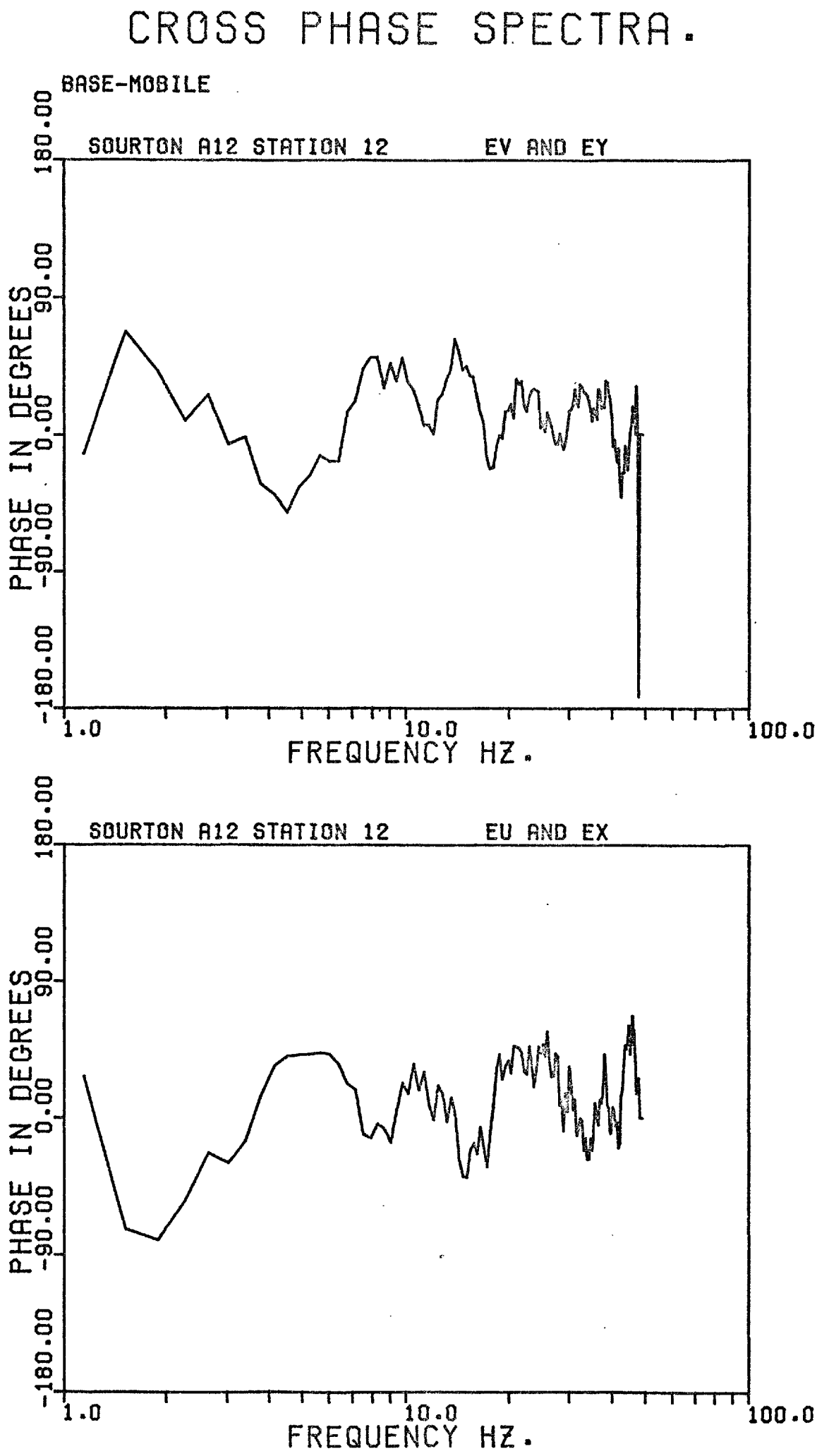


Figure 5/14 Station 12 cross phase spectra

SOURTON A12 STATION 12

COMPONENTS EV/EY

	FREQ.	CROSS POWER	AMP RT	PHASE
1	4.953	0.861085+03	1.178	-98.865
2	5.548	0.116755+04	2.450	-98.568
3	6.214	0.217395+04	2.325	-28.385
4	6.960	0.329745+04	1.546	-50.958
5	7.795	0.417505+04	1.417	-16.577
6	8.731	0.726795+04	0.903	-97.460
7	9.779	0.248665+04	0.560	-105.682
8	10.953	0.138945+04	0.690	-23.771
9	12.268	0.205355+04	0.743	-29.287
10	13.740	0.722455+04	0.375	-66.361
11	15.390	0.822915+04	0.357	12.524
12	17.237	0.299065+04	0.352	18.507
13	19.307	0.107915+04	0.225	27.244
14	21.625	0.103265+04	0.206	22.105
15	24.221	0.233495+04	0.189	15.048
16	27.128	0.303095+04	0.322	13.441
17	30.385	0.986955+03	0.406	-6.547
18	34.032	0.629125+03	0.256	-20.274
19	38.118	0.451045+03	0.275	-5.257
20	42.694	0.268105+03	0.272	27.318
21	47.819	0.398955+02	0.238	32.944
22	53.560	0.154005+03	0.273	0.568

COMPONENTS EU/EX

	FREQ.	CROSS POWER	AMP RT	PHASE
1	4.953	0.205755+02	0.406	-12.566
2	5.548	0.657415+02	0.396	77.853
3	6.214	0.372435+02	0.363	104.875
4	6.960	0.957705+02	0.318	5.272
5	7.795	0.172255+03	0.233	43.262
6	8.731	0.261415+03	0.195	68.826
7	9.779	0.670485+02	0.130	46.270
8	10.953	0.300455+02	0.183	-1.227
9	12.268	0.531715+02	0.224	19.600
10	13.740	0.836685+02	0.178	-23.569
11	15.390	0.967025+02	0.152	-74.789
12	17.237	0.168615+03	0.118	-66.761
13	19.307	0.164105+03	0.105	-3 312
14	21.625	0.150535+03	0.112	-1.425
15	24.221	0.175735+03	0.123	24.683
16	27.128	0.192835+03	0.113	34.463
17	30.385	0.187395+03	0.143	19 300
18	34.032	0.190055+03	0.148	19.030
19	38.118	0.140285+03	0.141	13.795
20	42.694	0.700195+02	0.131	10.341
21	47.819	0.357795+02	0.136	-11.811
22	53.560	0.467545+02	0.129	6.058

Figure 5/15 Print-out for Station 12 Digitized section

Ampl.
Phase

Element / Freq.	ESTIMATES 1	2	3	4	5	6	AVE.		SKEW
A11	0.50656	0.55564	0.51340	0.54524	0.49761	0.55554	0.53119		0.85235
31.281	68.28398	75.38472	68.12724	68.28398	61.96498	68.11520	68.20256	14	
A22	0.55611	0.57924	0.58620	0.57376	0.57018	0.59301	0.57977		0.93438
31.281	70.66221	73.76415	70.63221	70.83886	63.25565	71.12696	70.83256	14	
A12	0.23083	0.39106	0.23618	0.25319	0.18494	0.25718	0.24435		0.96217
31.281	-33.31472	-33.31472	-36.39667	-40.41554	-38.88104	-44.26548	-38.59885	14	
A21	0.07395	0.06328	0.07955	0.07762	0.16119	0.07476	0.07773		1.08273
31.281	138.60224	144.16856	146.02880	144.90118	138.60224	151.59810	145.28258	14	
A11	0.15527	0.27941	0.07183	0.93362	0.30148	1.81863	0.74484		0.08657
33.569	20.90612	-83.04135	64.11172	20.90612	-54.29121	113.91110	54.95677	15	
A22	0.43583	0.50862	0.51184	0.20163	0.43659	1.16670	0.57900		0.14715
33.569	90.68621	110.53919	90.68621	47.45962	112.24272	60.28712	72.28504	15	
A12	0.44414	1.00180	0.51832	0.79324	0.81460	2.23491	0.99916		0.30644
33.569	72.50642	72.50642	52.65345	176.45398	83.86881	-47.21705	63.59918	15	
A21	0.12775	0.23430	0.12797	0.24804	0.25428	0.49606	0.24996		0.13286
33.569	10.21699	-1.14540	-11.33952	85.41432	10.21699	-133.14787	-12.21402	15	
A11	0.43707	0.68194	0.49911	1.22467	2.58637	1.34365	0.87613		0.13257
35.858	61.60931	-163.85900	79.76344	61.60931	-7.32425	73.05476	69.00920	16	
A22	0.47645	0.83065	0.58901	0.54408	0.35738	0.68980	0.57484		0.63803
35.858	94.17800	135.92676	94.17800	76.02367	-25.64935	78.32305	85.67573	16	
A12	0.19536	1.71383	0.34059	0.30481	1.38970	0.56119	0.35049		0.31154
35.858	91.88811	91.88811	50.13935	-42.64359	-144.42622	-16.56388	20.20500	16	
A21	0.05056	0.35965	0.03792	0.31074	1.28142	0.35155	0.18769		0.01755
35.858	61.28317	-62.40249	-176.88947	130.21573	61.28317	152.65200	41.31561	16	
A11	0.32455	0.29909	0.32301	0.36502	0.24489	0.36188	0.34369		0.79436
38.147	54.71512	46.70901	54.93195	54.71512	66.73298	55.27620	54.90960	17	
A22	0.67754	0.67943	0.68796	0.67399	0.75067	0.68538	0.68129		0.96391
38.147	73.08380	76.14290	73.08380	72.86698	73.34425	72.82124	72.96396	17	
A12	0.09273	0.20616	0.09295	0.08538	0.10149	0.08531	0.08909		0.99849
38.147	81.73800	81.73800	78.67890	89.74411	61.17542	84.89868	83.76492	17	
A21	0.04195	0.04594	0.04649	0.03165	0.24485	0.03901	0.03978		1.58065
38.147	-75.30033	-55.23875	-76.06078	-87.81819	-75.30033	-90.17311	-82.46310	17	

Figure 5/16 Telluric Tensor Printout, Line A/12, Station 9

CHAPTER 6

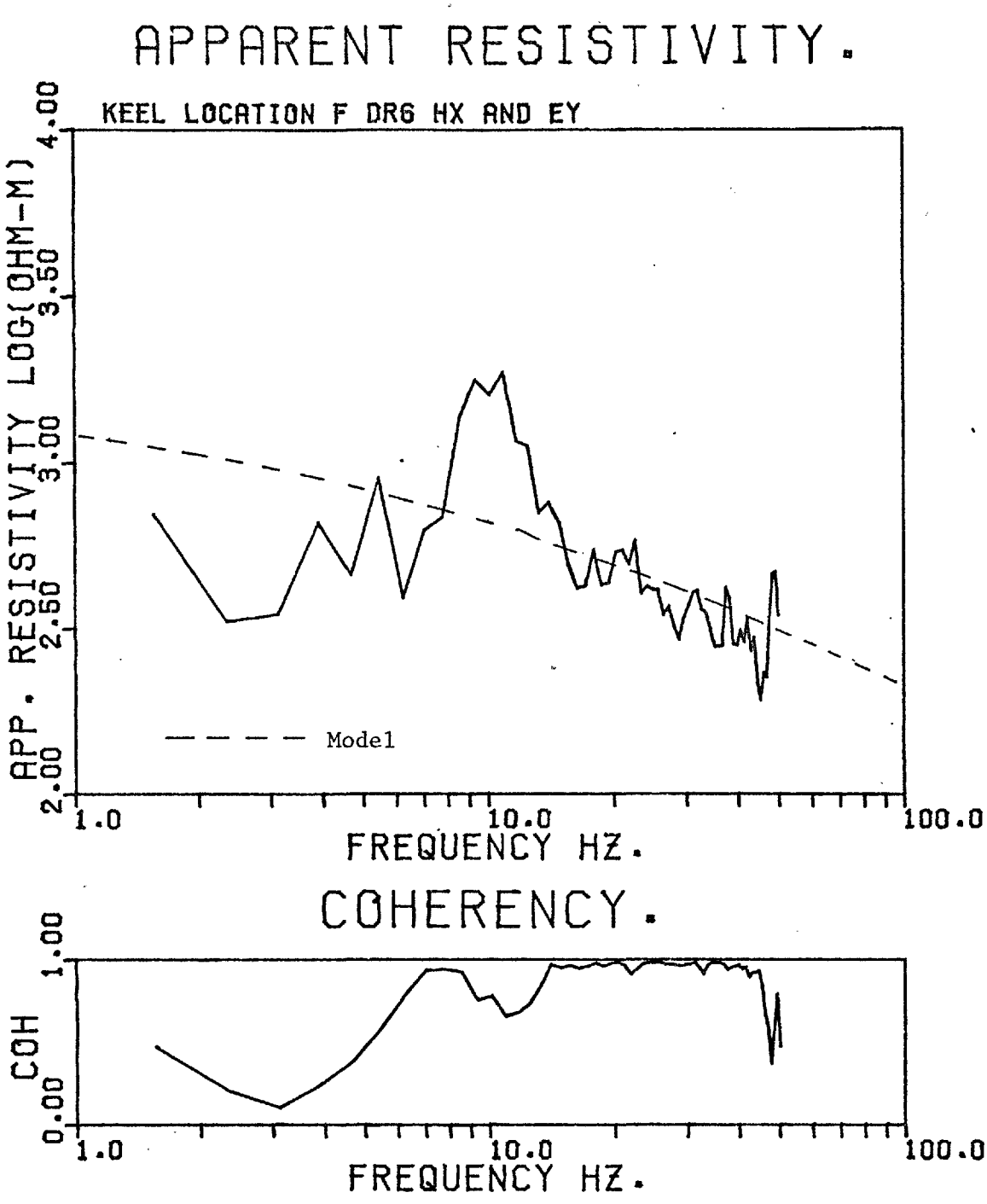
MODELLING AND INTERPRETATION

6.1 Model studies are the only realistic way of determining geological structure from the results of telluric or magnetotelluric surveys. Contour maps of survey results often show trends which coincide with known geology; the difficulty lies in interpreting features which lack such control. Interpretation thus depends on a knowledge of the anomalies caused by specific structures. For electromagnetic methods the calculation of such anomalies by approximate numerical techniques is especially important, because of the limitations of analytical methods and inconveniences of laboratory modelling. Features such as topographic irregularities, overburden and irregular conductivity variations can be modelled numerically. One dimensional layered models are, of course, readily soluble analytically and often provide valuable insight into the approximate behaviour of the field in more complicated situations (see section 1.5) Their simplicity allows them to be used with great success in quantitative interpretation by successive approximation, or by the use of standard curves. Recent developments include a non-linear least squares program for optimising the fits of multilayer models to experimental data (Laird and Bostick, 1969). This program automatically generates an "initial guess" model, as a starting point. Unfortunately, magnetotelluric data is often of poor quality or limited bandwidth, and only warrants approximate interpretation by comparison with 2 or 3 layer standard curves (Keller and Frischknecht, 1966, p 243, Yungul, 1961).

An example of a simple two layer, one dimensional model is shown in Figs 6/1 and 6/2. It is fitted

to the magnetotelluric data described in 4.4. The model results were generated by an interactive computer program, using equation 1:48 and written to enable multilayer one dimensional models to be calculated rapidly, on line, from a computer terminal. The starting model, chosen by comparing the field results with two layer curves (Keller and Frischknecht, 1966, p 219) was modified until an adequate fit with the real amplitude and phase responses was achieved. The coherency plot gives a good indication of the reliability of the field results, as a function of frequency and suggests that below 7Hz, and between 9 and 14Hz, the apparent resistivity and phase estimates are of doubtful validity. The low coherency at these frequencies corresponds with low power spectral densities in both electric and magnetic fields (see Fig 4/4). Low power density between 9 and 14Hz is frequently observed in records of this type, and corresponds to the "gap" between the first and second Schumann resonances. The poor coherency below 8Hz is probably due to magnetometer preamplifier 1/f noise, the magnetometer being an earlier, less sensitive design than that depicted in Fig 2/5.

The high coherency in the range 15 - 45Hz is diagnostic of either a one dimensional situation with random source field polarization, or a two/three dimensional situation with a plane polarized source field. In order to distinguish between these alternatives, the perpendicular magnetic field recorder outputs were connected to the X and Y deflection inputs of an oscilloscope for display in polar form. It could then be seen that the section of record used for Fig 6/1 was approximately randomly polarized, justifying a one dimensional interpretation.



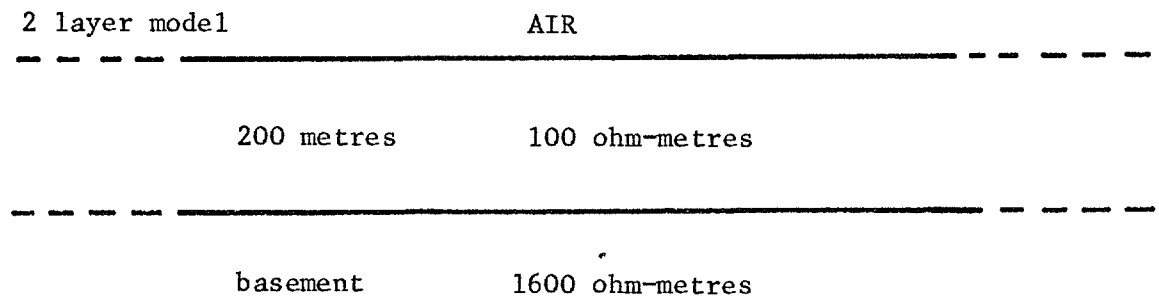
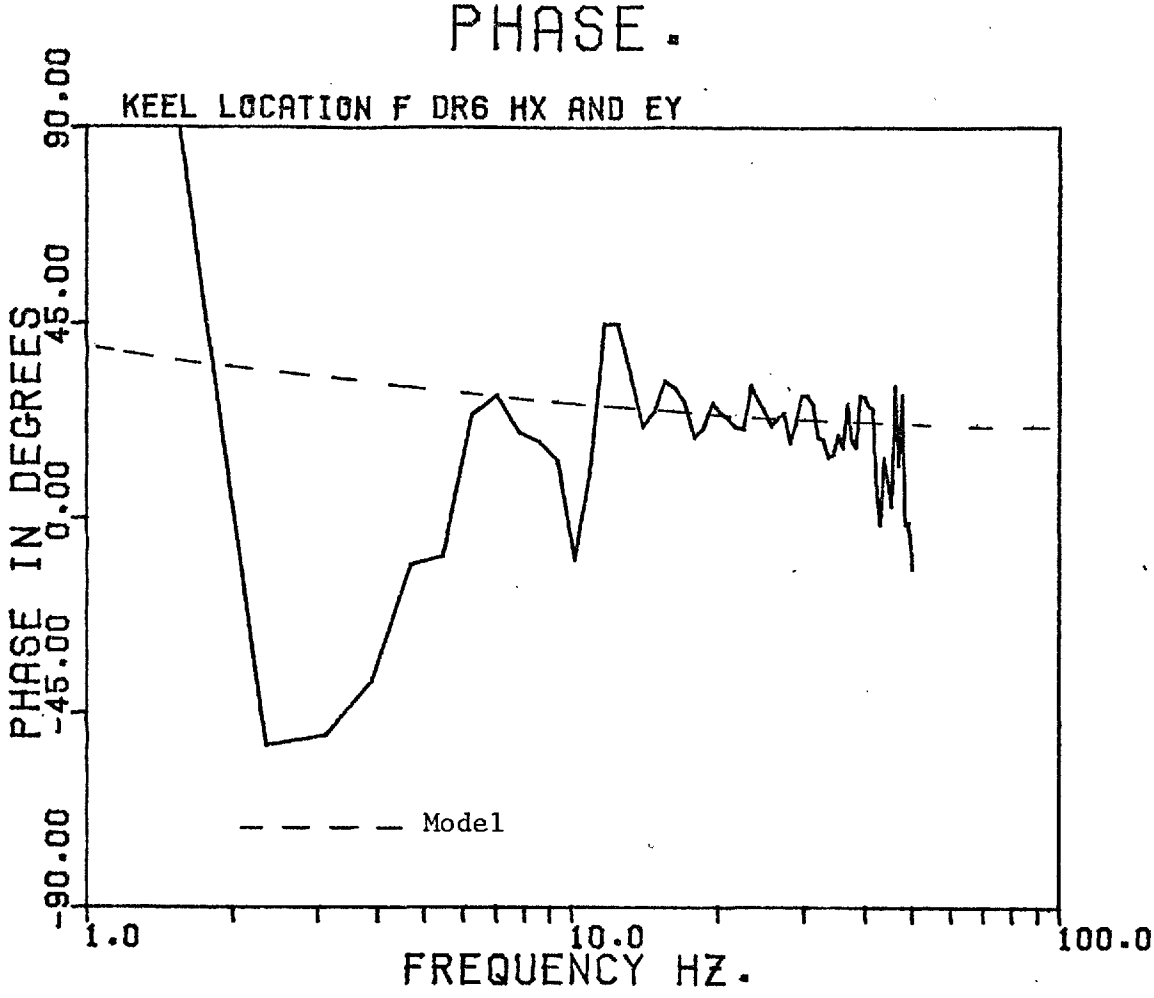


Figure 6/1 One dimensional model fitted to magnetotelluric data from Ireland (see also Fig 6/2)



	THICKNESS METRES	RESISTIVITY OHM-M.
LAYER 1	200.0	100.0
LAYER 2	INFINITY	1600.0

FREQUENCY (HZ.)	RESISTIVITY (OHM-M.)	PHASE (DEG.)
1.00	1192.41	37.76
1.26	1151.56	37.04
1.58	1107.78	36.26
2.00	1061.13	35.43
2.51	1011.77	34.54
3.16	959.89	33.61
3.98	905.79	32.64
5.01	849.87	31.63
6.31	792.59	30.59
7.94	734.50	29.53
10.00	676.21	28.47
12.59	618.36	27.42
15.85	561.62	26.41
19.95	506.61	25.44
25.12	453.94	24.54
31.62	404.13	23.74
39.81	357.62	23.07
50.12	314.73	22.56
63.10	275.68	22.25
79.43	240.58	22.16
100.00	209.45	22.34

2 layer model

Figure 6/2 One dimensional model fitted to magnetotelluric data from Ireland (see also Fig 6/1)

6.2 Two dimensional Models

It was shown in section 1.7 that the fields in a two dimensional model propagate in the independent TE and TM modes. Analytical solutions of the scalar Helmholtz equations determining the behaviour of the electric field parallel to strike (TE) and the magnetic field parallel to strike (TM) have been described only for certain restricted cases. D'Erceville and Kunetz (1962) give TM solutions for a number of vertical fault models, overlying basement of infinite or zero conductivity. Their analysis of the TE polarization, however, has incorrect boundary conditions (Patrick and Bostick, 1969). Solutions for dipping contacts are given in Geyer (1972) and for dipping anisotropic layers in Negi and Saraf (1972) and Reddy and Rankin (1971).

Several authors have recently described numerical techniques for the solution of more general two dimensional cases. There are three popular approaches: the transmission surface analogy (Swift, 1971; Wright 1970), the finite difference method (Jones and Pascoe, 1971) and the finite element technique (Coggon, 1971; Silvester and Haslam, 1972). In all of these, the modelled region is divided into a number of small elements or cells; the three approaches differ in the manner in which solutions for the diffusion equation are obtained.

The finite difference method is intuitively the simplest and is used in the computer programs listed in Jones and Pascoe (1971). Refinements to the original programs have since been published, and several authors have made use of this material for modelling real situations (Pascoe and Jones, 1972). Owing to the complexity of the computation of two dimensional models, automatic fitting to real data with curve matching algorithms, of the type used for

one dimensional data, is not at present an economic proposition. It is likely, however, that this situation will change with the advent of improved computational methods.

6.2.1 The Finite difference method

The finite difference method has been applied to many physical model problems (see Vitkovitch 1966 pp 103 - 156). Briefly, the approach as applied to TE and TM polarizations for a two dimensional case, is as follows (for details see Jones and Pascoe, 1971 and Appendix B). The transverse electric or magnetic field in a model is represented by a complex number at each point on a rectangular grid. A value of conductivity is also assigned to each element of the grid, so that any desired conductivity distribution can be represented within the limits of resolution imposed by the grid spacing. The field at any grid point can be used to calculate field values at adjacent points by Taylor series approximations. The simplest case is the "five point" difference relation, in which terms of the Taylor series higher than the third order are neglected, giving a quadratic approximation to the field over any three adjacent horizontal or vertical grid points. This is adequate provided the grid spacing is sufficiently small in regions where the field varies rapidly. Each point in the grid is calculated in turn from its neighbours using the Finite difference equation until all have been covered. The whole operation is repeated until the maximum residual (the difference between successive values at a grid point) is smaller than a preset amount. The boundary conditions at interfaces between regions of unlike conductivity affect the construction of the difference equations, and the different formulations for the TE and TM polarizations lead to solutions for the two cases which are quite independent. For both polarizations

the solution at the side boundaries of the grid approximates to a one dimensional case if the sides are sufficiently far from lateral conductivity variations in the centre region. Vertical grid spacings are arranged so that the fields at the bottom boundary tend to zero. The boundary conditions at the top of the grid are fundamentally different for the two polarizations. For the TM case (strike along the x-axis), Ampère's law, equation 1:4, with the neglect of displacement current gives

$$\frac{\partial Hx}{\partial y} = J_z \qquad 6:1$$

There is no current flow across the air/earth boundary so that $J_z = 0$ and hence $\partial Hx/\partial y = 0$. Hx is therefore set to a constant value at the surface and is also constant in the air layer above. In the TE case Ex and Hy can both vary along the surface, and Hy is a constant at $|y| = \infty$. The surface value of Ex as $|y| \longrightarrow \infty$ is determined by the wave impedance at the surface of the appropriate one dimensional case. Above the surface the conductivity is zero, so that the diffusion equation 1:16 becomes equivalent to Laplace's equation,

$$\frac{\partial^2 Ey}{\partial z^2} = 0 \qquad 6:2$$

The solution of this is

$$Ey = D_1 + D_2 z$$

where D_1 and D_2 are constants representing the amplitudes of downward and upward propagating waves, which are calculated in obtaining the surface wave impedance (see section 1.5). The boundary values across the top of the air layer are calculated by linear interpolation between the top values of Ey at the sides, a procedure which is only valid if the boundary is so far from the surface that perturbations in the field due to structure in the centre of the model are negligible.

6.2.2 Finite difference computer programs

As they stand, the programs of Jones and Pascoe (1971), with subroutine BYCOND from Pascoe and Jones (1972), leave room for improvement. There is a fairly serious error in their derivation of the difference equations, which means that the program is only valid for grids of identical square or rectangles (see Appendix B). This error has been corrected and other modifications made as below.

The original program was designed for a 40 x 40 grid. Changes have been made so that any size of grid can be used, a maximum limit being imposed by the central memory capacity of the computer. For economy, the smallest possible number of grid points should be used. Both the time taken for one iteration and the number of iterations required to achieve a solution of given accuracy increase with the number of grid points.

A facility for "over relaxation" has now been included in the iteration subroutine. For details of this technique, which improves the rate of convergence of the solution, see Vitkovitch (1966, p 120). The amount of central memory space required to run the original program has been cut by reducing the number of arrays containing the full set of grid points from 9 to 3. This allows models with about 3000 grid points to be run in the same central memory space previously occupied by a 1681 point model with only a slight increase in processing time.

Several practical points should be borne in mind when using the finite difference method

a) The grid spacing is critical, especially if large conductivity contrasts are to be modelled (see Appendix B). A given grid design can often only be used over a small range of frequencies or conductivities.

b) Although the TE and TM polarizations have different optimum grid designs, the same grid can often be used satisfactorily for both.

c) Discontinuities in the field at the boundaries, when the residuals are negligibly small, indicate faults in the mesh design.

6.2.3 Three dimensional Models

Three dimensional electromagnetic modelling techniques are not yet well developed. The only tractable analytical solution is for the case of a sphere, a classical problem which has been considered many times since the late 19th century. Recent investigators are Negi (1967) and Fuller (1971).

The finite difference method has been applied to limited three dimensional cases by Jones and Pascoe (1972), but details are not given of the precise formulation of the difference equations.

There is a semi-quantitative discussion of the effects of three dimensional bodies on the impedance tensor in Word et al. (1970).

6.3 Interpretation of Sourton Tors results

It is immediately clear from the profiles in Figs 5/5 and 5/6 that there is a zone of anomalously high conductivity causing a "low" in the telluric field near station 13 on line A12. The minimum value of the field ratio Ev/Ey is.07, and of Eu/Ex is 0.2. In both cases the anomaly appears to be greater at higher frequencies, but for Eu/Ex this is almost certainly due to the Eu preamplifier noise level which increases towards low frequencies. The field strength over the anomaly is about .02 microvolts r.m.s./metre, which gives an input signal of only 0.6 microvolts for a 30 metre electrode separation. The input noise for the Ev preamplifier was of the same order, and for the Eu preamplifier was somewhat greater. The lack of coherency of the

signals over the anomaly also points to random noise influences. Digital processing, using much longer sections of record than could be digitized by hand, would probably alleviate this problem.

The electric field at the surface, for a given magnetic field, is proportional to the square root of the apparent resistivity. A change in the electric field ratio from 1.0 at the base station to 0.07 at station 13 therefore represents about a 200:1 change in apparent resistivity. Fig 6/3 shows the results of an Induced Polarization and resistivity traverse along part of line A12, plotted with $(Ev/Ey)^2$, from the 32Hz traverse shown in Fig 5/6. The field ratios have been normalized to coincide with the resistivity at station 7. The similarity between the resistivity and telluric measurements is striking.

In addition to the distinct anomaly near station 13, there is also a steady decrease in the amplitudes of the roving station fields all the way across from base to station 17. It is probable that this is due to a resistivity contrast between the granite and the country rock (see Fig 5/1. At station 18 the resistivity seems to be rising as the traverse passes onto the Meldon Volcanics series (Tuffs).

Inspection of the maps of the I.G.S. horizontal loop electromagnetic survey shows that the traverse lines are not perpendicular to the longest axis of the anomaly, which is approximately parallel with the geological contacts in Fig 5/1 (see Fig 6/4). The small lateral extent of the anomaly suggests that a two dimensional interpretation is likely to be invalid. A departure from two dimensionality is also indicated by the fact that Ev/Ey, the field ratio most nearly parallel to "strike", has greater variations

than Eu/Ex. In a two dimensional case the electric field parallel to strike is only slightly affected by small, intense anomalies (Slankis et al. 1972). Two dimensional modelling is nevertheless useful for showing the approximate magnitude and distribution of the conductivity variations required to produce the observed profiles.

The model shown in Fig 6/5 was calculated using the program mentioned in 6.2.2. The granite (B) dips at an angle of 45° beneath the country rock (C) with a resistivity contrast of 3/2. The anomaly is simulated by a dipping sheet (D) of resistivity 20 ohm-metres, sandwiched between two layers (E) with resistivities of 100 ohm-metres. Fig 6/5 shows the calculated profile, compared with the 32Hz Ev/Ey results from Fig 5/6. The shape of the profile depends on two main factors:

1) The dip of the contact between B and C, and their resistivity contrast. The gradual reduction in the field from station 1 to station 18 is governed by these. A vertical contact produces too abrupt a transition.
2) The configuration of the dipping sheet of low resistivity. The layers D were introduced to make the edges of the anomaly less sharp. In practice, some smoothing would be introduced by the finite measuring electrode separation. In measuring the electric field over anomalies of this type, the smallest possible electrode separation should be used, consistent with obtaining a good signal to noise ratio.

The model does not explain the large phase shifts of the electric field near station 18 (see Figs 5/7 and 5/8). It is possible that these are due to a resistivity contrast between the Meldon Cherts and the Tuffs, or to the steep terrain at this end of the traverse (see Fig 5/1).

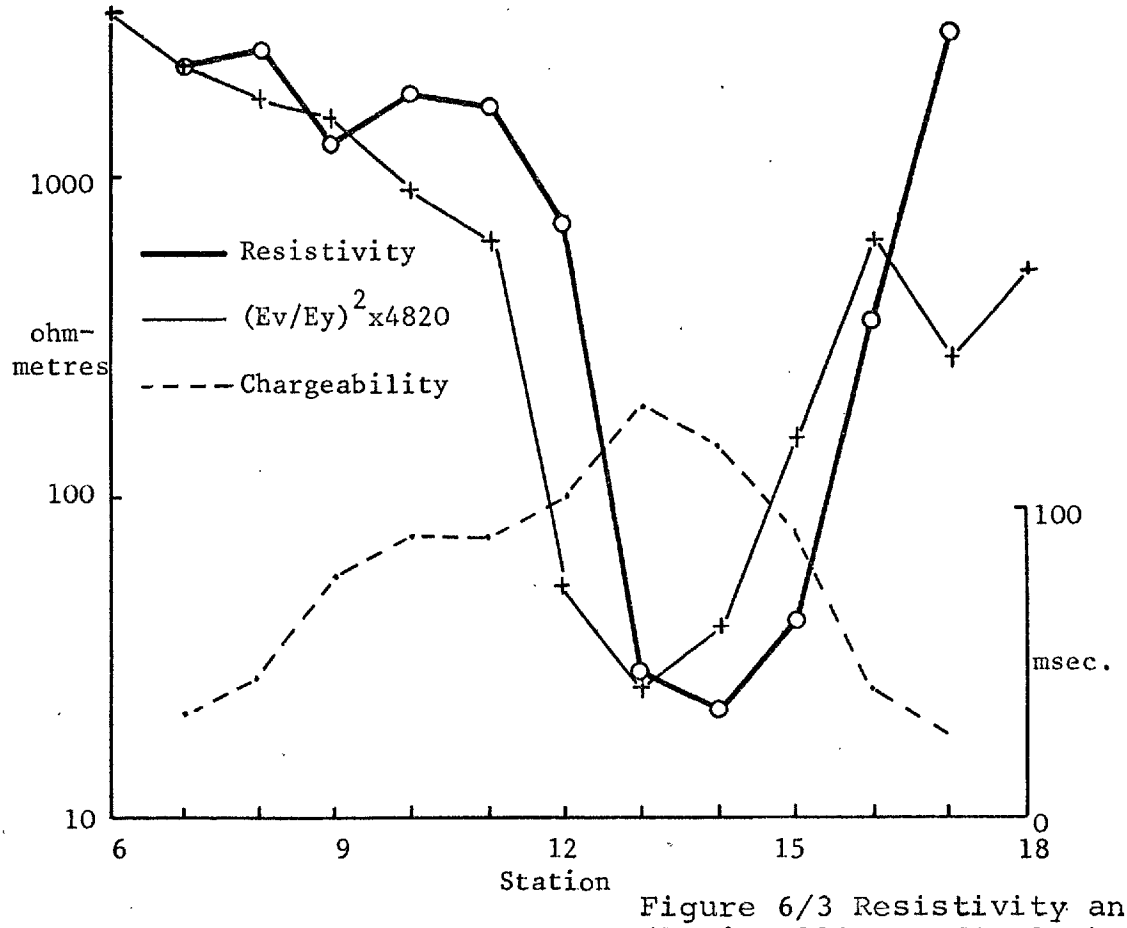


Figure 6/3 Resistivity and I.P. (100' collinear dipoles) compared with telluric traverse

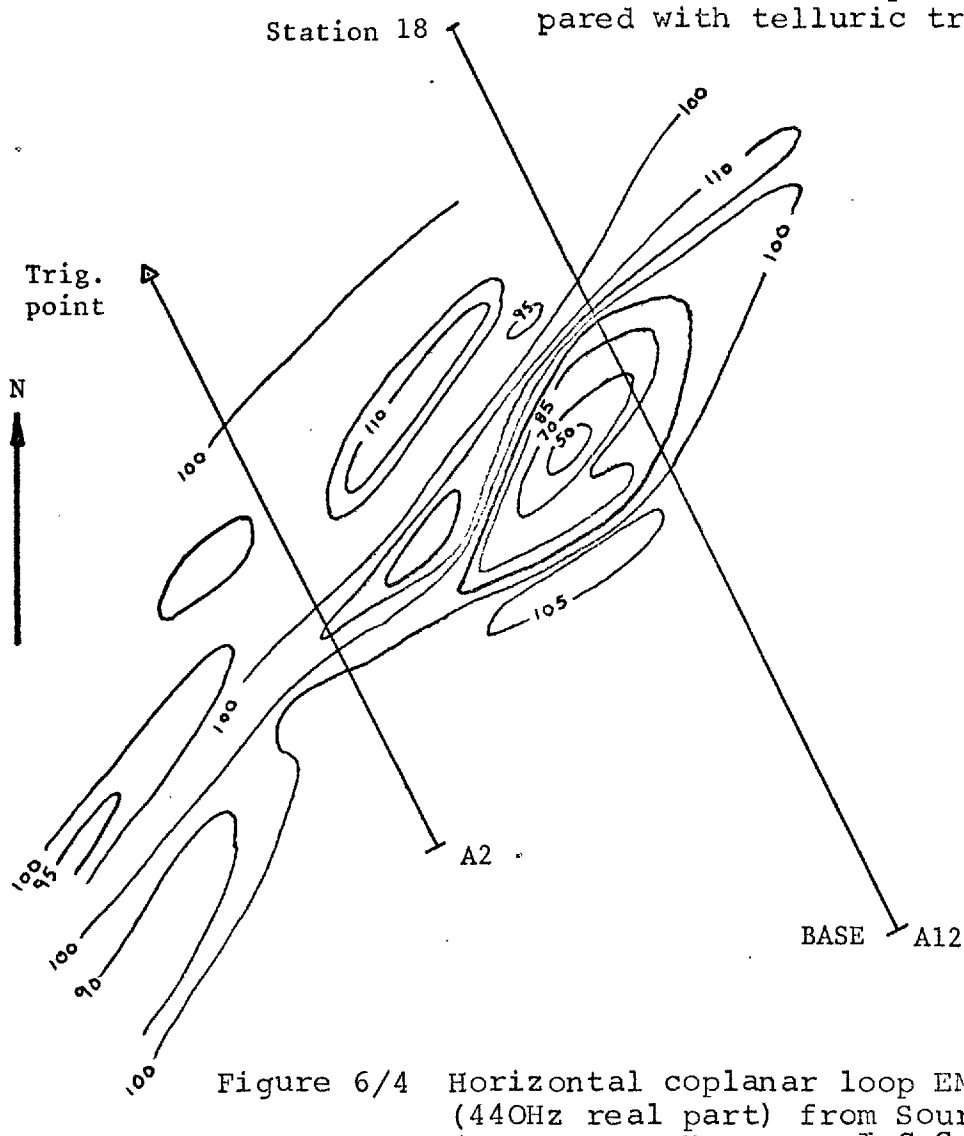
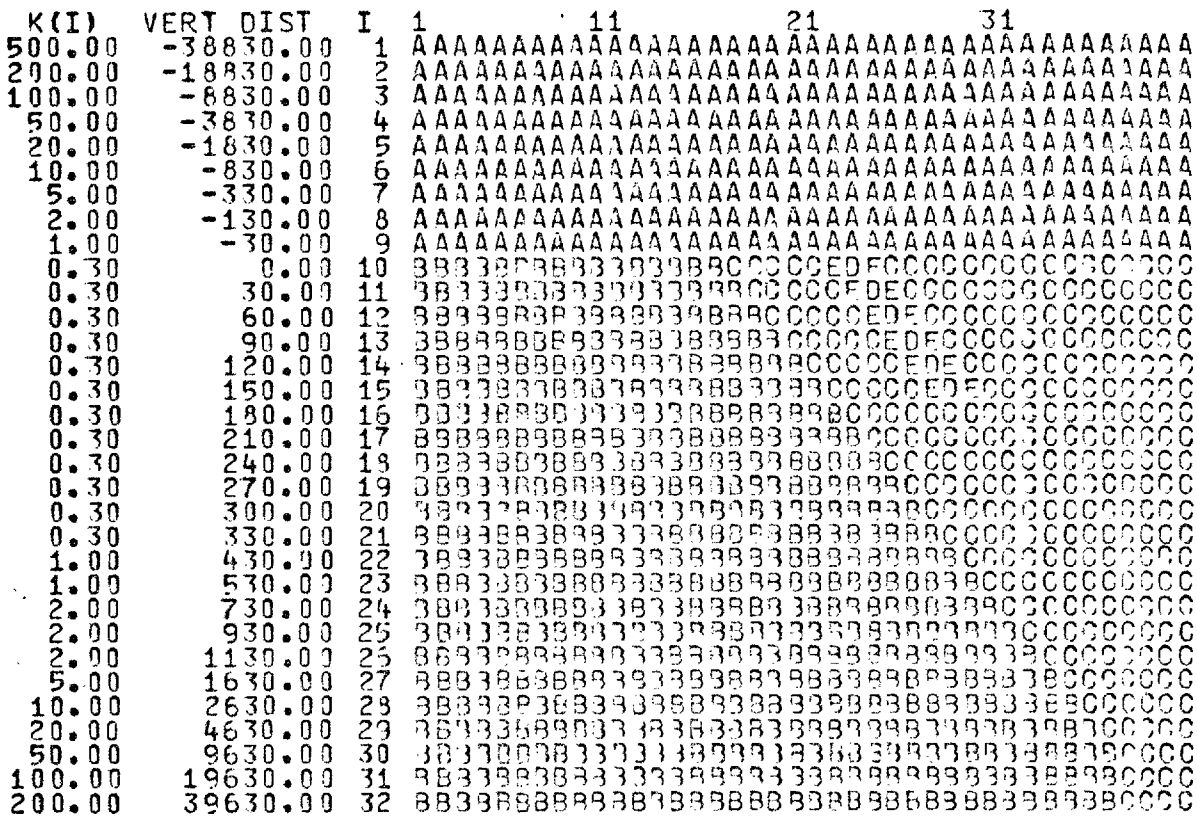


Figure 6/4 Horizontal coplanar loop EM results (440Hz real part) from Sourton Tor (Pers. com. K. Beer, I.G.S.)

SOURTON MODEL 15



BETWEEN COLUMNS SCALE

BASE AT COLUMN 11

1	AND	2	50000.00 METRES
2	AND	3	20000.00 METRES
3	AND	4	10000.00 METRES
4	AND	5	5000.00 METRES
5	AND	6	2000.00 METRES
6	AND	7	1000.00 METRES
7	AND	10	500.00 METRES
10	AND	11	200.00 METRES
11	AND	12	120.00 METRES
12	AND	30	30.00 METRES
30	AND	32	100.00 METRES
32	AND	35	200.00 METRES
35	AND	36	500.00 METRES
36	AND	37	1000.00 METRES
37	AND	38	2000.00 METRES
38	AND	39	5000.00 METRES
39	AND	40	10000.00 METRES
40	AND	41	20000.00 METRES

AREAS RESISTIVITIES

A	INFINITY	
B	1000.000	OHM-METRES
C	666.667	OHM-METRES
D	20.000	OHM-METRES
E	100.000	OHM-METRES

Figure 6/5 Two dimensional model for line A 12 Sourton Tor

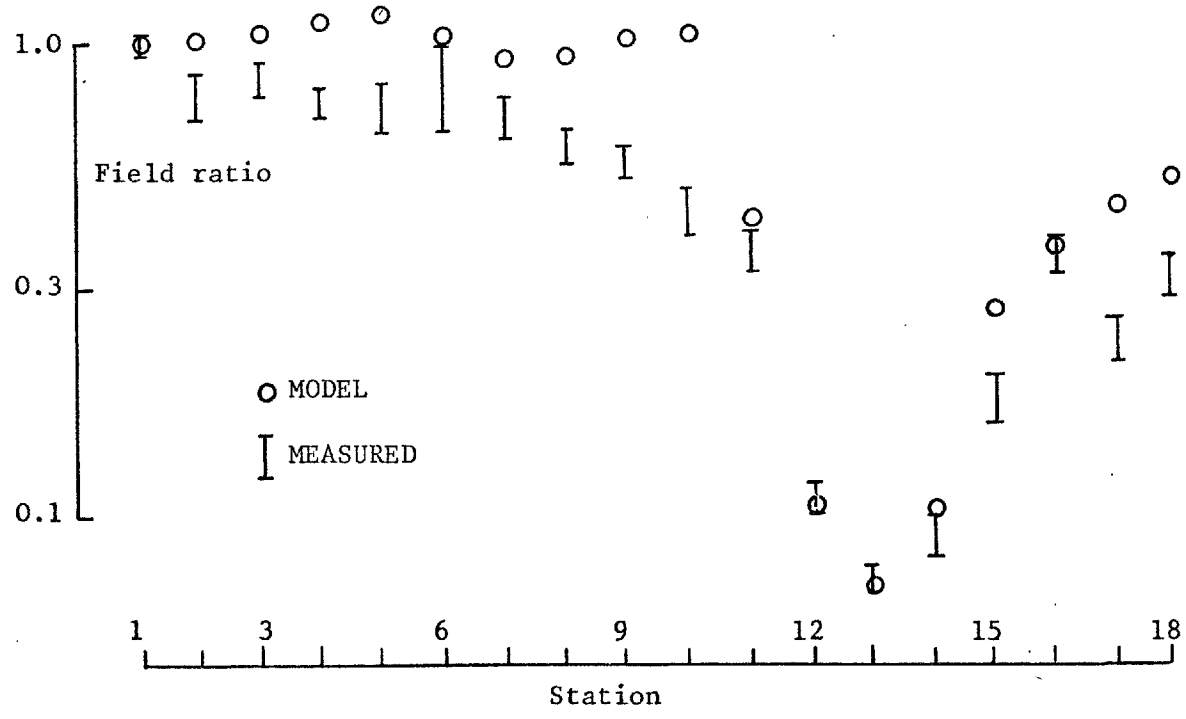


Figure 6/6 Model results compared with field results
Line A12, Ev/Ey, 32Hz.

CHAPTER 7

CONCLUSIONS AND SUGGESTIONS FOR FURTHER WORK

7.1 Summary

The primary emphasis of this project has been on the development of field equipment. It has been shown that the equipment functions satisfactorily under field conditions, and gives results consistent with those from other prospecting methods. Encouraging results have been obtained by using simple electronic analogue processing of field recordings. The radio telemetry system has enabled analogue methods to be used for direct measurement of relative telluric field strengths in real time. It was hoped that signal analysis in the field would lead to the eventual elimination of the necessity for recording. In practice it was found that readings taken in this way are very slow, owing to the long integration times involved, especially if measurements are required at several frequencies. Recordings have the advantage that they can be examined for reliability on playback and subjected to various different kinds of analysis; meter readings cannot satisfactorily be checked in retrospect for spurious signals. Analogue processing of the Sourton Tor recordings yielded better results than digital methods; this was due to limitations in the digitizing facilities rather than superiority of the analogue method. The full potential of the telluric method can only be realised by telluric tensor analysis of the four field components Ex, Ey, Eu and Ev. Analogue equipment for this task would be specialized and complicated; digital processing can be performed on modest computer installations using existing techniques.

7.2 Future developments

The field equipment described in this dissertation is currently being used to establish the behaviour of the electromagnetic field in several different geological situations. It is hoped that these case histories will help to create standard procedures for the analysis of E.L.F. field recordings by digital methods.

Possible future developments are outlined below; their feasibility could be tested by using the existing equipment:

a) A simple, highly portable system with a base and a roving station (each with one channel), incorporating a radio telemetry link. At the roving station there is analogue circuitry for measuring relative field strength, phase and coherency, at a number of frequencies. This equipment could be used for making rapid surveys of the relative telluric field strength approximately normal to the strike of suspected two dimensional anomalies.

b) Equipment similar to that described in a), but having a pair of induction magnetometers for making measurements of the relative magnetic field along profiles normal to the strike of suspected two dimensional anomalies. Variations of the vertical magnetic field could also be measured. This system would be more mobile than the telluric system in a), as there would be no need to lay out electrode spreads. Both systems could easily incorporate a facility for making recordings on a lightweight cassette tape recorder.

c) A lighter, more efficient version of the existing equipment with the main emphasis on

the recording capability, but with analogue circuitry for in-the-field analysis, and monitoring of record quality.

It would not be possible to make complete telluric or impedance tensor element determinations with the equipment in a) and b), although the directions of the principal axes in a two dimensional situation could be found in the way described in section 4.3 (p.72). Rapid coverage of a survey area could be achieved by making measurements perhaps at only two (widely spaced) frequencies. The equipment in c) would be designed for more comprehensive, but slower, measurement and interpretation.

A.1 General notes on operation and adjustment

a) Always check that the main amplifier DC input voltage range is not being exceeded when using high pass filter (S2 to AC). Set S3 to Lo and S4 to zero with S2 at DC. Check that the meter can be zeroed with VR36. (Fig A/5)

b) If either supply voltage is allowed to fall below 7.6 volts on load, cross talk between channels will occur. The current drain is high for the size of battery used in the battery pack, so unplug modules which are not being used.

c) Tune the radio receiver for maximum deflection of its tuning meter, not "by ear".

d) Ensure that Station A is functioning correctly, by listening to the F.M. carrier modulation, before making recordings.

e) Check DC balance of main amplifiers occasionally if S5 is at AC.

f) A module undergoing adjustment should be plugged with an extender card in its correct position in the rack. If a module is changed from one rack to another, it may need readjustment to compensate for slight differences in power supply voltages.

g) Check that the positive and negative battery voltages are at least 8 volts (S1 and M2 on battery pack, see Figs A/25, A/26) and that the positive supply to the module under test is at between 4.75 and 5.25 volts. The negative supply voltages should be within 3% of the positive supply voltages.

h) If a test source is connected to one of the input pins of a module, make sure that other modules connected to this pin via the frame wiring are unplugged. (see Figs A/1, A/2)

i) The negative series regulator transistors (T1 and T2, Fig A/25) are liable to be damaged if the negative stablized supply is short circuited. The positive supply is protected against short circuits.

A.2.1. Main Amplifier Notch Filter (Figs A/3 and A/5)

Instruments reqd: Audio oscillator 10-100 Hz, Oscilloscope or high impedance voltmeter. The frequency of the oscillator used for the alignment should be checked continuously on an accurate frequency meter.

Tuning	Max Rejection	-20dB flank
1st section	49.50 Hz	50.00 Hz
2nd section	50.50 Hz	50.00 Hz

a) Connect oscillator to input (pin 5) and 'scope to output of 1st section.
b) Set osc. to 15Hz and adjust level to give about 3v. p-p on 'scope. Note the amplitude.
c) Set osc. to 49.50Hz and trim VR1, 2 and 3 in turn to give minimum on 'scope (< 30 mV.)
d) Set osc. to 50.00Hz and trim VR4 to give 1/10th the amplitude observed in b. (-20dB)
e) Repeat steps b, c and d until output minimum at 49.50Hz and -20dB at 50.00Hz.
f) Remove link and connect oscillator to input of section 2, 'scope to output.
g) Set osc. to 15Hz and adjust level to give about 3v p-p on 'scope. Note the amplitude.
h) Set osc. to 50.50Hz and trim VR6, 7 and 8 in turn to give minimum on scope (<30mV)
i) Set osc to 50.00Hz and trim VR9 to give 1/10th the amplitude observed in g (-20dB)
j) Repeat steps g, h and i until output minimum at 50.50Hz and -20dB at 50.00Hz.
k) Replace link, connect osc to input (pin 5) and check that filter output is less than 1/100th (-40dB) between 49.3 and 50.7 Hz.

A.2.2 Low Pass Filter

Check that output is at least -40dB at 500Hz relative to output at 15Hz. -3dB frequency is -45Hz but this is obscured by notch filter. For information on calculation of component values for different frequencies see Burr Brown (1969).

A.2.3 High Pass Filter (Figs A/4 and A/5)

Offset adjustment:-

a) Short amplifier input (pin 5) to ground, set S5 to DC2, S3 to HI and S2 to DC.
b) Set M1 pointer to centre scale with VR36.
c) Switch S2 to AC and adjust VR15 until M1 pointer is again at centre scale.

The High pass -3dB frequencies are:-

Electric field Amplifiers (Red knobs)	0.255 Hz
Magnetic field Emplifiers (Yellow knobs)	0.562 Hz

To check these proceed as follows :-

d) Connect U.V. recorder to power stablizer board panel so that output of amplifier module is displayed.
e) Connect a supply of about 2v D.C. to input (pin 5) via a 1k resistor in series.
f) Set S2 to AC, S3 to LO, S4 to 0 and zero M1 with VR36.
g) Short pin 5 to ground
h) Start U.V. recorder on about 0.4" per sec when M1 steady.
i) Remove short from pin 5.
j) Stop recorder when transient has died away.
k) Check the chart against those from the other channels (see Fig A/6).

See Burr Brown (1969) for details of the calculation of component values for high pass filters.

A.2.4 A.C. meter zero adjustment

With S5 at AC and the input shorted, adjust VR44 until pointer of M1 is at left hand end of scale.

A.2.5 Gain Setting

a) Set S2 to DC, S3 to LO, S4 to zero.

b) Short input (pin 5) to ground. Connect sensitive meter to output (pin 1) and adjust VR36 for zero deflection.

c) Connect input (pin 5) to 1.5 v dry cell or similar low impedance source and measure voltage across input.

d) Connect voltmeter to output and adjust VR18 until voltage at output is the same as voltage at input, with reverse polarity.

e) The D.C. gains for different settings of S3 and S4 can be checked in a similar manner and should agree to within $\pm$ 1% of the values given in Fig A/4.

A.3 Dual V.C.O. module (Figs A/7, A/8 and A/9)

a) Plug V.C.O. module into frame with extender card. The two main amplifiers driving the V.C.O.s should also be in position.

b) Short the main amplifier inputs and set gain controls to LO 4 with S2 at DC so that -4 volts to +4 volts can be set at the V.C.O. inputs with VR36.

c) Connect an accurate voltmeter to input (1) (Pin 4) and a digital frequency meter to output (1) (Pin 7)

d) Set input voltage to 0.00 volts with VR36 on the appropriate main amplifier.

e) Adjust VR2(1) until frequency = f_o (See Fig A/7)

f) Set input to +4.00 volts with VR36.

g) Adjust VR1(1) until frequency = f_2

h) Repeat steps d to g until f_o and f_2 are within $\pm$ 0.1% of their prescribed values.

i) Set input to -4.00 volts and check that the output frequency is f_1, within $\pm$ 0.1%.

j) Connect oscilloscope to output and check that waveform is sinusoidal over the full range of input voltage. The amplitude should be 2.5-6.0 volts p-p.

k) Connect voltmeter to input (2) (pin 21) and frequency meter to output (2) (Pin 16) and repeat steps d to k for the other circuit on the board.

A.4 Pilot tone and mixer module (Figs A/10 and A/11)

Adjustment of carier levels:-

a) With the module on an extender card in the correct position in the rack, plug in the tape recorder and switch to "record".

b) Set tape recorder "record level" control to about ½ maximum.

c) Select each carrier in turn with S1 and adjust VR1-6 so that each carrier gives about ½ scale deflection on the record level meter.

d) Switch S1 to mix and check that mixed carrier is obtained.

Note:- When the system is used in "base/roving" mode, the carriers from station A are passed through filters in the demodulator board prior to mixing to reduce noise from the receiver. Their joint level is adjusted with VR7 on the module front panel. The relative level of carriers 1 and 2 can be adjusted by VR10 and VR11 at the Tx mixer/driver on the Station A power stabilizer board (see A.25), or by VR2 on the pilot tone/ mixer board.

A.5 Telemetry transmitter and receiver

See manufacturers' information for internal adjustments to the transmitter and receiver. The receiver has an output buffer connected to the

detector so that the input to the Pilot tone/ mixer is independent of the receiver volume control setting (see Fig. A/12). The output level of the TX mixer/driver on the Station A power stabilizer board should be adjusted with VR10 and VR11 (Figs A/24, A/25) so that it is correct for the particular transmitter used.

At the time of writing, the transmitter is a Bradley TX 27/1. (Output level of TX mixer/driver should be 2 volts p-p).

The receiver is a Heathkit "Mohican" GC-1U with buffer stage (Fig A/12) connected between the junction detector diode/C53 and chassis (see the receiver hand-book)

A.6.1. Dual Demodulator Module,bandpass filters

(Figs A/13 and A/14)
Plug the module, on an extender card, into its position in the station B rack (see Fig A/2). The input (pin 3) is connected to the BNC socket on the panel of the power stabilizer board, via the frame wiring.

a) Connect audio oscillator to input and set to 910Hz, 0.3 v p-p.
b) Connect oscilloscope to A1(1) output and adjust VR3(1) for maximum output.
c) Connect oscilloscope to A2(1) output, set oscillator to 810Hz, and adjust VR7(1) for maximum output.
d) Connect oscilloscope to A1(2) output, set oscillator to 2300Hz and adjust VR3(2) for maximum output.
e) Connect oscilloscope to A2(2) output, set oscillator to 1900Hz and adjust VR7(2) for maximum output.

A.6.2. Pulse width and offset adjustment

The pulse width (VR11) and the offset controls (VR23) are adjustable through holes in the module front panel. The aim of these settings is to make the output voltage of the demodulator equal to the input voltage of the corresponding V.C.O. for all frequencies. From Fig A/8 it is seen that the conditions shown in Fig A/15 should be true if the settings are correct.

If an accurate digital frequency meter and volt meter are available, the settings may be made as follows:-

a) Connect oscillator and frequency meter to the input and the volt meter to output (1) (Pin 23)
b) Set input frequency to $f_o(1)$ (see Fig A/15) and adjust offset VR23(1) and/or pulse width VR11(1) until output voltage is zero.
c) Set input frequency to $f_2(1)$ and set output voltage to +4.00 volts with the pulse width control VR11(1)
d) Reset input frequency to $f_o(1)$ and adjust offset control VR23(1) until output voltage is zero.
e) Repeat steps c and d several times to achieve optimum settings.
f) Check that output voltage is -4.00 volts at $f_1(1)$
g) Connect oscillator to output (2) (Pin 9) and repeat procedure for circuit (2).
Procedure for rough adjustment in the field :
CAUTION: Adjustments should only be attempted if serious drift is suspected.
h) Set up station A and station B as if for calibration, with electric preamps connected to all four inputs. Switch S3 to LO, S4 to zero, S2 to AC, S5 to DC2 and zero M1 with VR36 on all four main amplifiers.
i) Switch function switch on RMS meter box (Fig A/16) to AC1 with S4 on the filter/Phasemeter module switched to OUT.

j) Check that carriers .85 and 2.1 kHz are present at station B by monitoring with the tape recorder and selector switch S1 on pilot tone/mixer module.

k) Set oscillator output to zero volts.

l) The RMS meters should both read zero with the channel selector S5 on the filter/phasemeter (Fig A/18) in either position. Set up the channel selector relay (Fig A/2) so that channels 1 and 3 are selected with S5 in position P, 2 and 4 in position Q.

m) Set right hand RMS meter (channel 3) to zero with VR36 on main amplifier. With the oscillator still at zero, channel 1, RMS meter is set to zero with VR23(1) offset control on demodulator panel.

n) Apply 25 mV rms at about 15Hz to the preamplifier inputs. The RMS meters should now both read approximately full scale deflection when switched to AC1 on the meter box.

o) If the RMS meter readings in m differ by more than ±10%, the pulse width control VR11(1) is adjusted until the readings are the same.

p) Repeat steps n to o until demodulator output on the RMS meter is zero with the oscillator at zero, and is equal to the other RMS meter for other inputs.

q) Switch channel selector S5 on the filter phasemeter panel to Q and use the procedure in 1 through p to set demodulator (2).

A.7 Dual RMS meter (Figs A/16 and A/17)

With Filter/phasemeter module out, plug Dual RMS meter module with extender card into Station B frame. Plug RMS meter box into socket on module front panel, and set meter box switch to AC1.

Gain, symmetry and offset adjustment.

a) Connect oscillator to input, set to 50Hz 2.5 volts rms and observe waveform at output of A2.

b) Waveform should be a rectified sinewave of amplitude 3.54 volts with all peaks the same height. If alternate peaks are of different amplitudes, adjust VR9 to make them the same.

c) The amplitude of the rectified sinewave is adjusted with VR13, maintaining similarity of adjacent half cycles with VR9.

d) Now reduce the input amplitude to about 10mVolt rms. Adjust VR4 and VR14 in turn until a regular rectified sinewave of maximum amplitude is obtained.

e) Repeat steps b, c and d to achieve best settings.

f) Short input, connect sensitive voltmeter to A3 output and set VR18 for zero offset.

g) With meter box switch at AC1 adjust VR1 for full scale meter deflection with 2.5 volt rms input.

h) Reduce input to 0.25 volts rms and adjust VR22 for full scale meter deflection.

A.8.1 Filter/Phasemeter (Figs A/18 and A/19)

This circuit is experimental and subject to design changes; the following notes apply to issue 2 of the circuit diagram (Fig A/19)

A.8.2 Phasemeter adjustment

a) With RMS meter module in position and meter box plugged in, insert filter/phasemeter into correct position in frame. Remove the modules connected to the inputs (demodulator, main amplifiers etc)

b) Short inputs (pins 18 and 21) to ground and connect oscilloscope (on "DC") to A2 output.

c) Adjust VR7 so that A2 (Limiter 1) output voltage is close to zero. It will change sign very rapidly as VR7 is turned. Switch S2 to its other position; output will change polarity if adjustment incorrect.

d) Now transfer the 'scope to A4 output and set Limiter 2 output as nearly as possible to zero with VR14. S2 does not affect A4.

e) Connect oscillator to inputs (pins 18 and 21), set to 20Hz 1 v.rms and switch S2 to 180°. Observe square wave output at T2 collector and set left hand meter on meter box to 1/2 scale with VR23. (Meter box switch to PHASE, S3 to 2).

f) Leaving pin 18 open apply a momentary signal of about 1 volt rms to pin 21, to trigger bistable (T1 and T2) into ON state. Set meter to zero with VR26.

g) Leaving pin 21 open apply momentary signal of about 1 volt rms to pin 18 to trigger bistable into OFF state. Set meter to full scale deflection with VR23. (VR24 if U.V. galvo is being used as meter)

h) Repeat steps e, f and g until best setting is achieved.

A.8.3 Filter adjustments:

Figure A/19 shows component values for filter frequencies of about 2, 8, 14 and 32 Hz in positions A, B, C and D of S1. The Q is 5 for all frequencies. For information about the calculation of component values for other frequencies and Q factors see Burr Brown (1969).

To set filters, proceed as follows

a) Connect oscillator to input (pin 18 and 21) and set to desired frequency, with amplitude about 1 volt rms.

b) Connect oscilloscope to filter output (pin 2) and adjust VR3 for maximum output.

c) To set filter 2 to the same frequency, switch S2 to 0° and observe phasemeter. Rotate VR8 until phase meter is just at the transition point between zero and full scale deflection. It is considerably easier to tune the filters for equal phase shift at resonance than to tune for individual maximum output.

A.9 Electric Preamplifier (Figs A/20 and A/21)

It is possible for this circuit to "latch up" (output remains at +9 or -9 volts irrespective of input). This condition can be avoided by switching on with the input switched to DC, with S2.

With $C_9 = C_{10} = 10^{-6}$F and $R_{10} = R_{11} = 10^7$ ohms, the input time constant with S2 in the AC position is 10 seconds, giving a high pass response with -3dB point at 0.0159 Hz.

The low pass response of the amplifier is controlled by C1 and C4. If C4 = C1 = .01 microfarad and R1 = R4 = 100 kilohms, the upper -3dB point is at 160Hz.

A.9.1 DC Balance adjustment:

a) Ground both inputs; connect voltmeter to output and turn VR9 to give zero volts at output.
Gain and common mode Rejection Ratio:
The DC gain of the circuit is fixed by the ratio R1/R2. With R1 = 100K $\pm$2% and R2 = 1K $\pm$2% the gain is x 100 $\pm$3%. The CMRR is best optimized at the frequency where the largest common mode effects are expected, which is probably 50 or 60Hz.
The procedure is as follows:

b) Connect oscilloscope to output, and oscillator across input terminals. Set desired frequency with amplitude about 25 mVrms.

c) Adjust VR3 and VR4 in turn until minimum amplitude is seen on the oscilloscope. Note the amplitude V_1 of the waveform.

d) Now ground either input with the oscillator at the same setting. A much larger amplitude V_2 will be seen on the 'scope. The Common Mode Rejection Ratio = V_2/V_1. A value of 1000 (60dB) should be attainable.

e) To check the gain at any frequency, connect oscillator across inputs, ground one input and measure the ratio of the input and output amplitudes. The oscillator amplitude is best set to about 25 mV rms for this test.

A.10 Magnetometer Preamplifier (Figs A/22 and A/23)

DC balance adjustment:

a) Short input with S2 and set DC voltage at output to zero with VR3. N.B. The circuit has a long time constant, so this adjustment should be performed slowly.

Gain check:

The circuit has a low pass response, determined by C2, R2 and R1. With R2 = 470k, R1 = 1k and C2 = 1.0 microfarads the gain should be unity at about 160Hz, or x20 at about 8Hz.

$$\text{Gain} = 1 + \frac{Z}{R} \quad \text{where } \frac{1}{Z} = \frac{1}{R_2} + jwC_2$$

b) Connect oscillator to input and oscilloscope to output. Set oscillator to 100mV rms at 8Hz and check that the output is about 2 Volts rms. The output amplitude should decrease as the frequency is increased.

A.11 Power Stabilizer Module (Figs A/24 and A/25)

The power stabilizer circuit requires no adjustment. Care should be taken to avoid short circuiting the negative stabilized supplies, as this may damage the series regulator transistors T1 and T2.

A.12 Timer Module and U.V. recorder interfacing (Fig. A/28)

The Timer module is used in conjunction with the Lennartz demodulator to provide triggering for the timing line generator of an S.E. Laboratories type 3006 U.V. Oscillograph. Its input is taken

from the output of the 6.4 kHz pilot tone band pass filter in the Lennartz unit. (see Lennartz Handbook). A flying lead on the Timer module board enables various triggering rates to be selected.

The U.V. recorder interface circuit gives a full scale deflection of about 4 cms (C300 galvonometers) for $\pm$1 volt demodulator output. The galvonometers are critically damped and have a flat response to well over 100Hz. Trimmers are provided for small sensitivity adjustments.

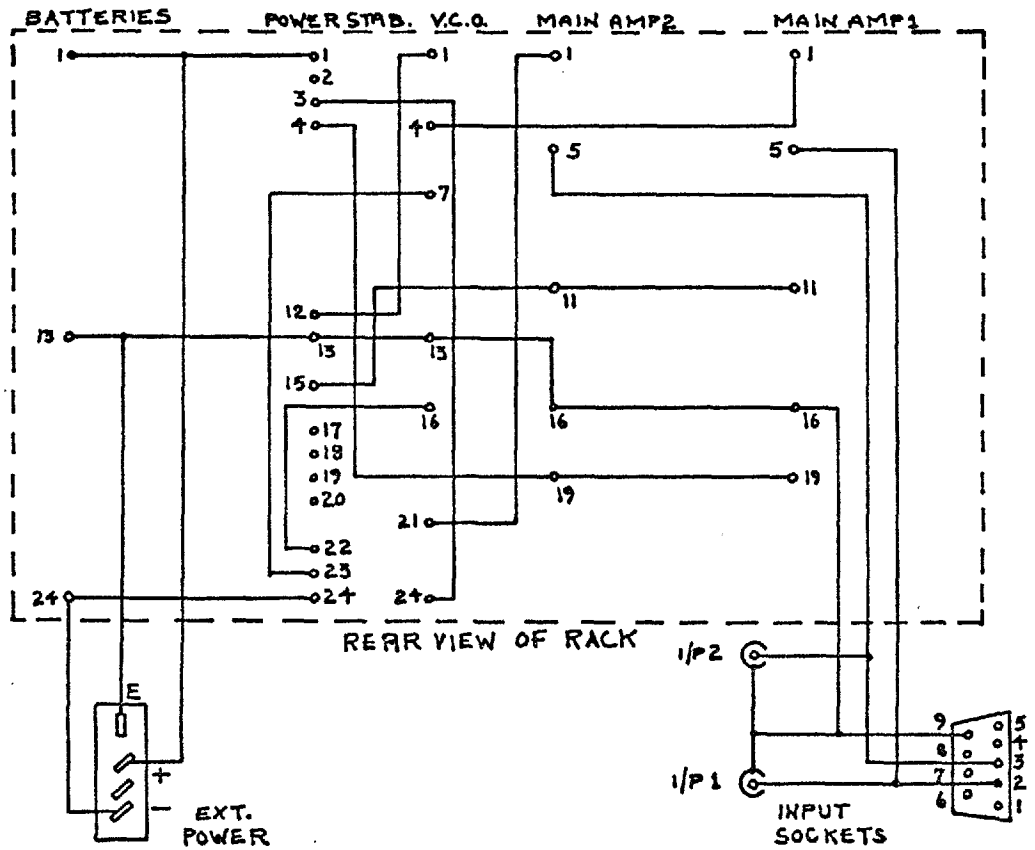


Figure A/1 Main Frame Wiring, Station A

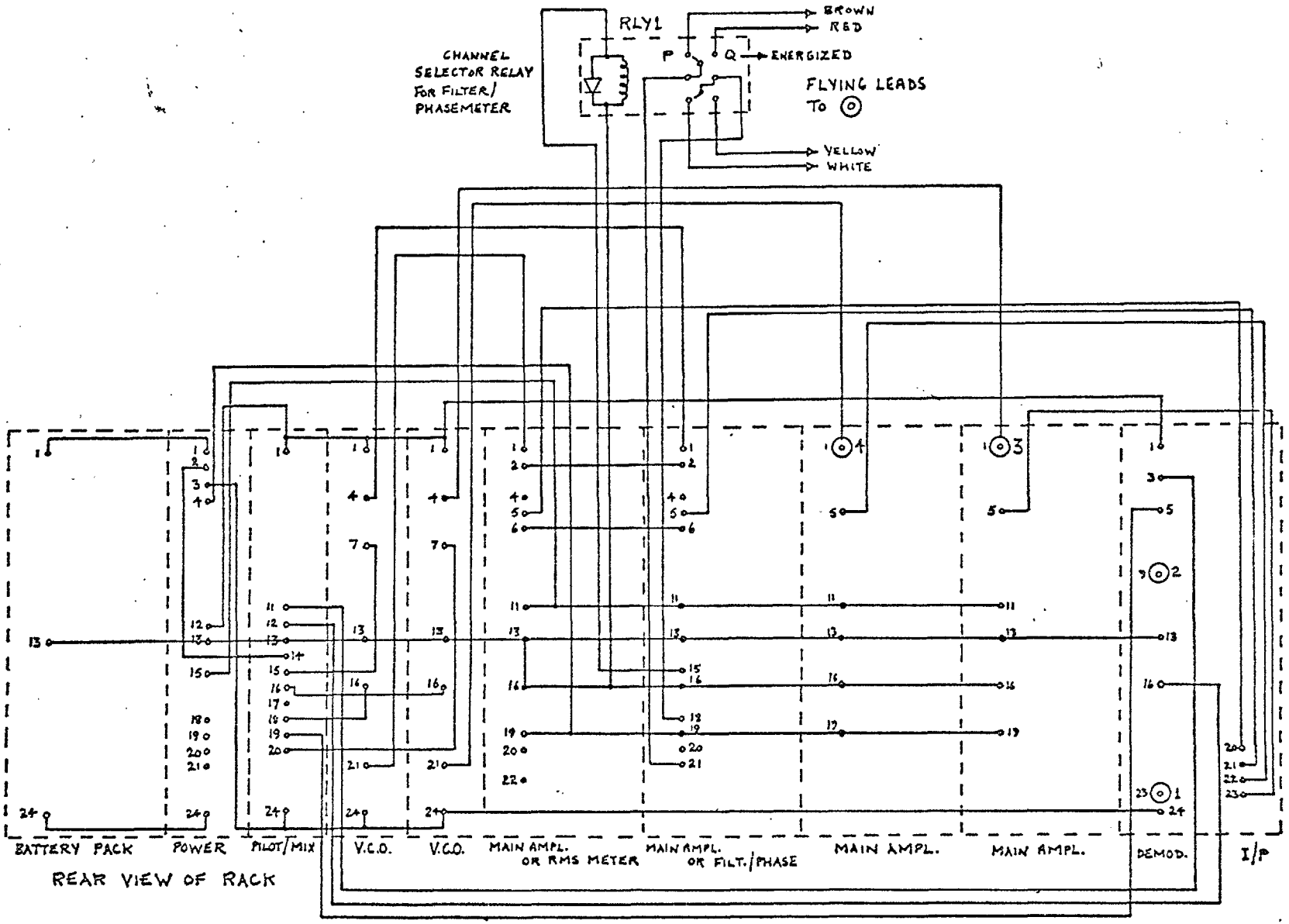


Figure A/2 Main Framewiring Station B

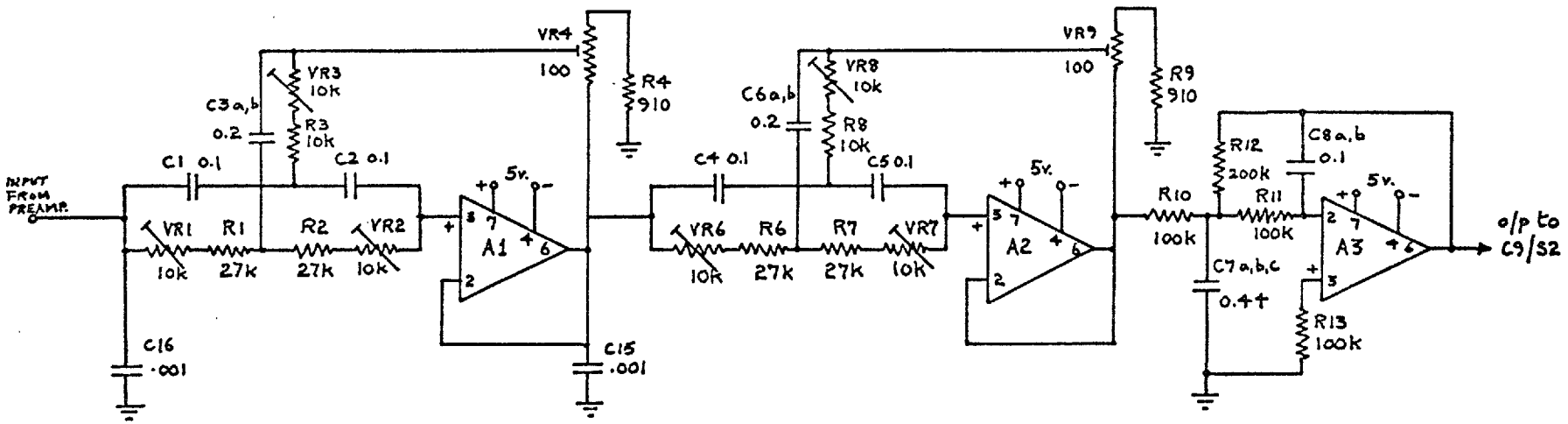
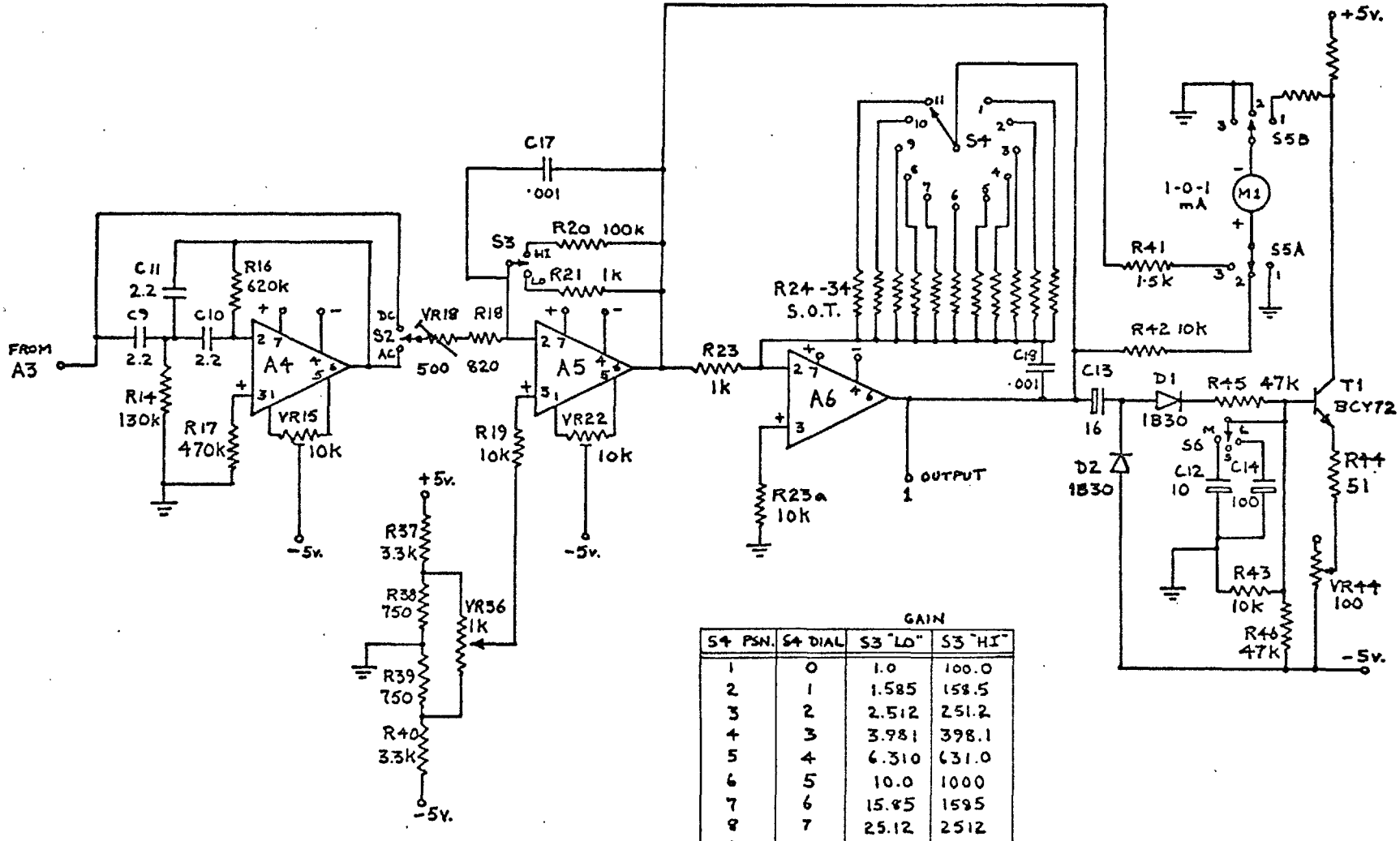


Figure A/3 Main Amplifier module, notch and low pass filters



GAIN

S4 PSN.	S4 DIAL	S3 "LO"	S3 "HI"
1	0	1.0	100.0
2	1	1.585	158.5
3	2	2.512	251.2
4	3	3.981	398.1
5	4	6.310	631.0
6	5	10.0	1000
7	6	15.85	1585
8	7	25.12	2512
9	8	39.81	3981
10	9	63.10	6310
11	10	100.0	10000

Figure A/4 Main Amplifier module, high pass filter and gain stages

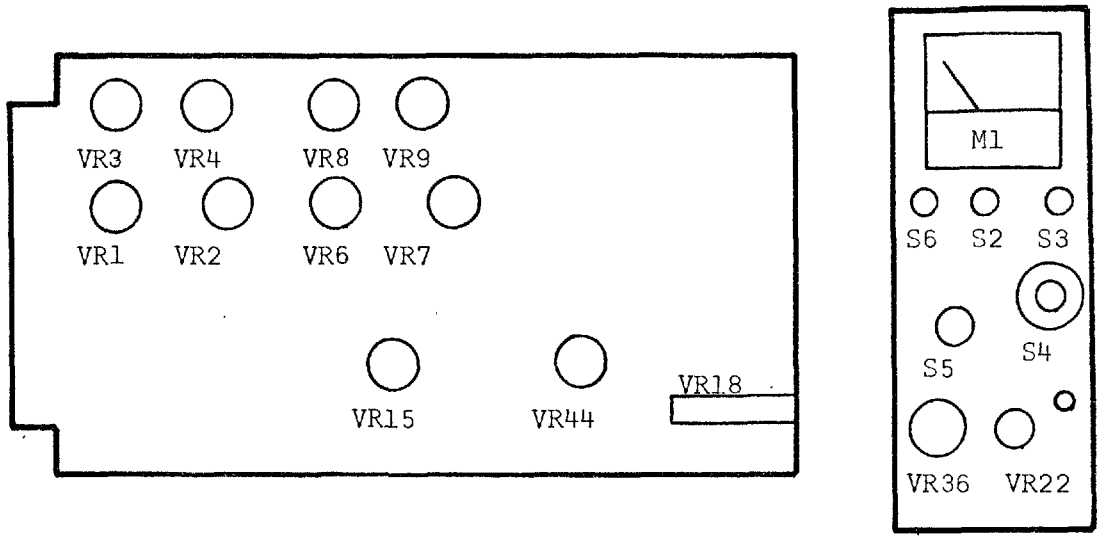


Figure A/5 Main Amplifier module, control layout

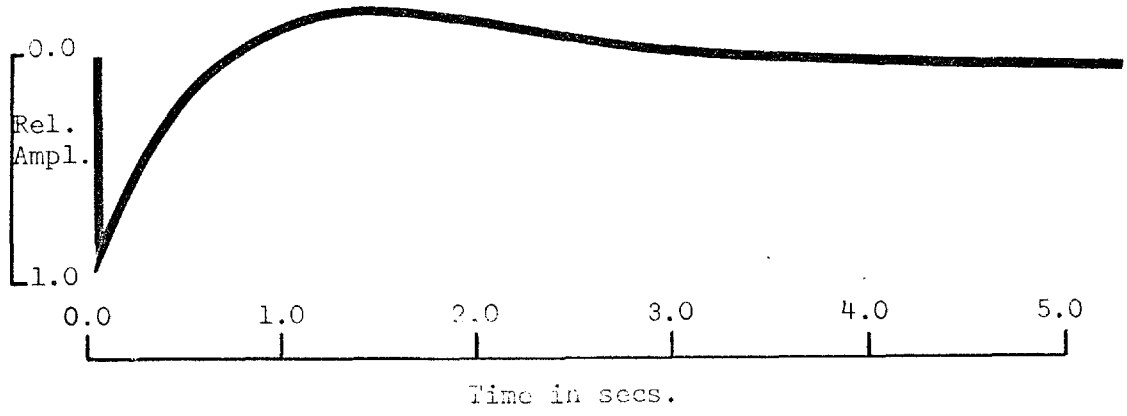
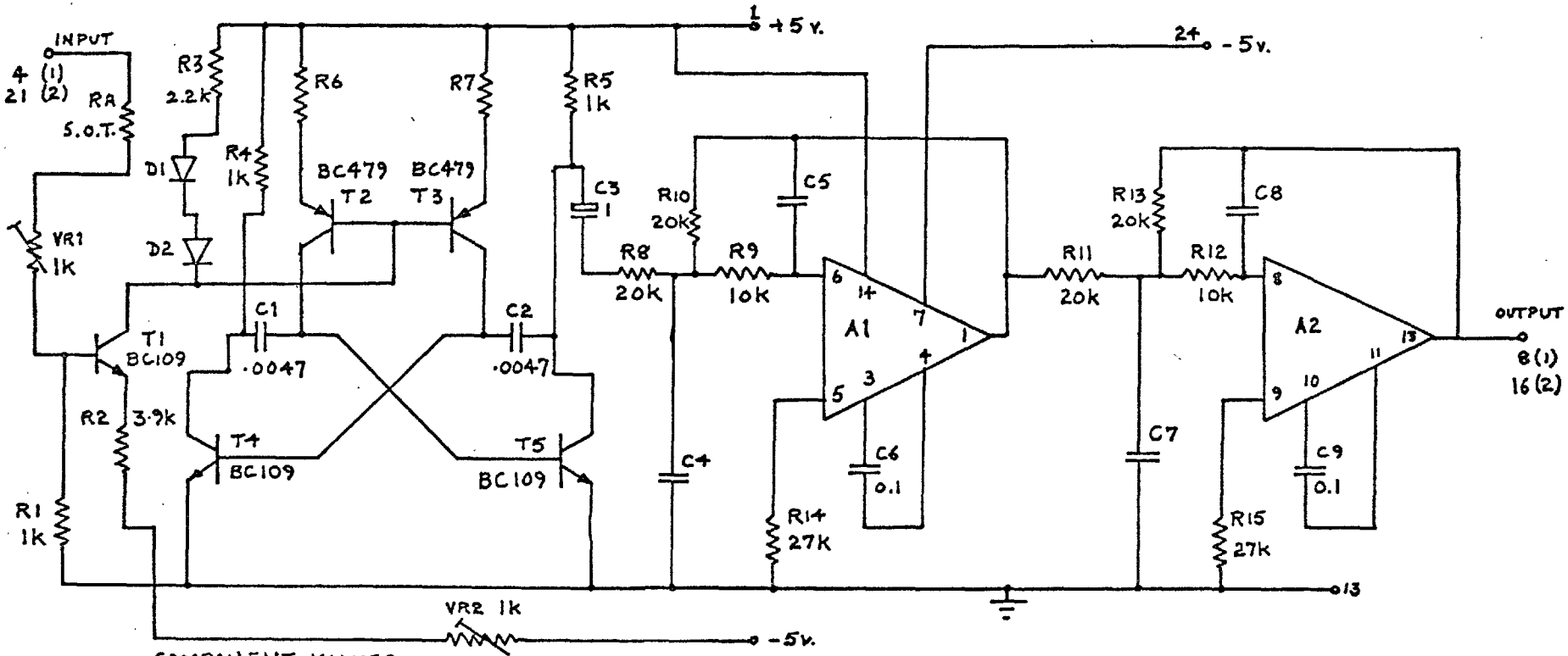


Figure A/6 Main Amplifier module, high pass filter step response



COMPONENT VALUES

CENTRE FREQ.	DEVIATION %	UPPER FREQ	LOWER FREQ	-3 DB. POINT	R6&R7	C4 & C7	C5 & C8
0·860 KHz	±15	·989 KHz	·731 KHz	1·0 KHz	75 k	·022 μF	5600 pF
2·10	±15	2.415	1.785	2.3	33 k	·01 μF	2200 +220 pF
4.40	±15	5.060	3·740	5.4	15k	3000 +1000 pF	1000pF
9·5	±7·5	10.213	8·788	11·0	6·8k	1000 +1000 pF	470 +47 pF
13·0	±7·5	13.975	12.025	15·0	4.7 k	1000 +470 pF	330 +47 pF
17·5	±7·5	18.812	16.187	20·0	3.9k	1000 +150 pF	270 +10 pF

Figure A/7 Dual V.C.O. module circuit

f_o = centre frequency input grounded.

f_1 = lower cal. frequency input=-4.0 volts.

f_2 = upper cal. frequency input=+4.0 volts.

Channel	f_o kHz	f_1 kHz	f_2 kHz	Module no.
1	0.860	0.731	0.989	1
2	2.100	1.785	2.415	1
3	4.400	3.740	5.060	2
4	9.500	8.788	10.213	2
5	13.000	12.025	13.975	3
6	17.500	16.187	18.812	3

Figure A/8 V.C.O. frequency settings

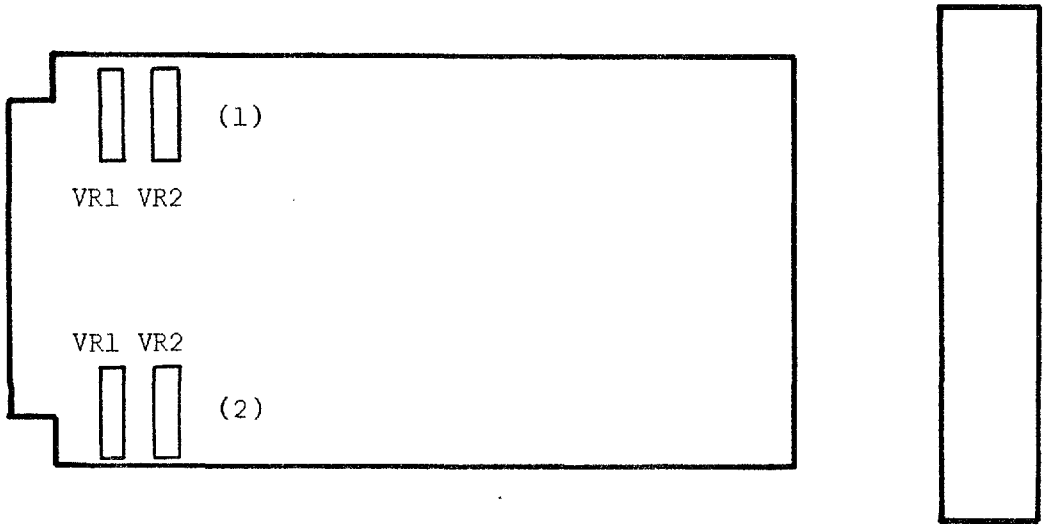


Figure A/9 Dual V.C.O. module control layout

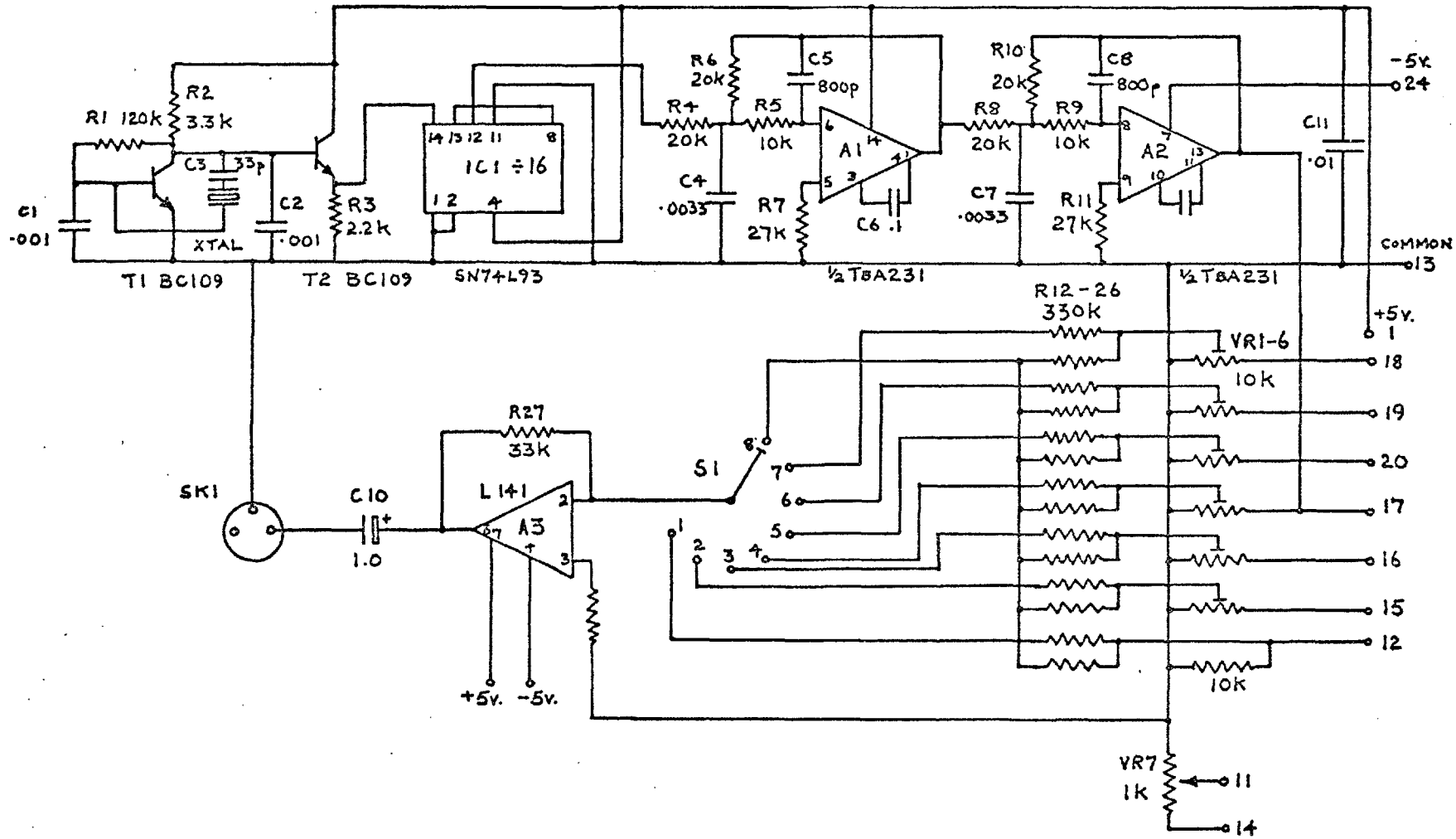


Figure A/10 Pilot tone/mixer module circuit

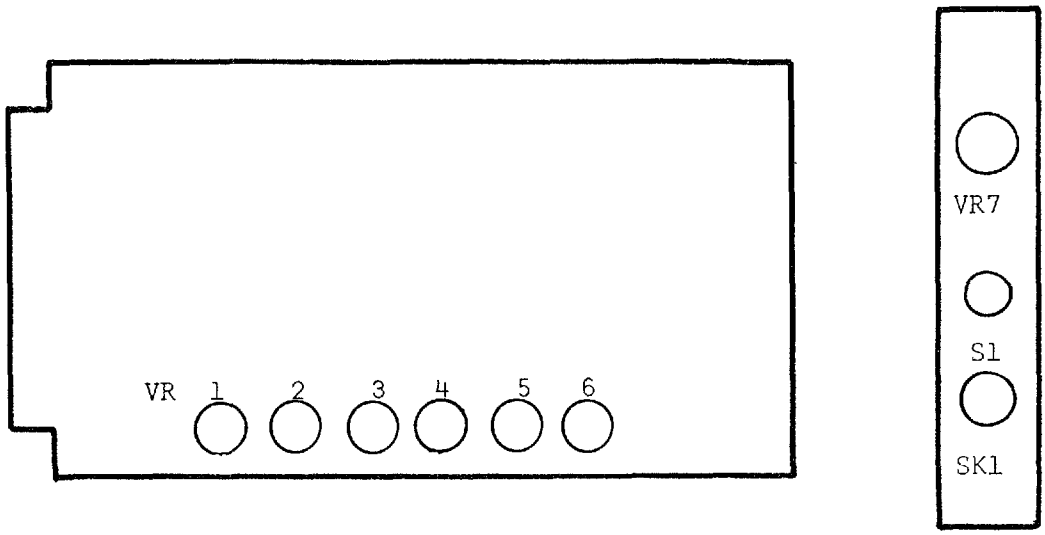


Figure A/11 Pilot tone/mixer module, control layout

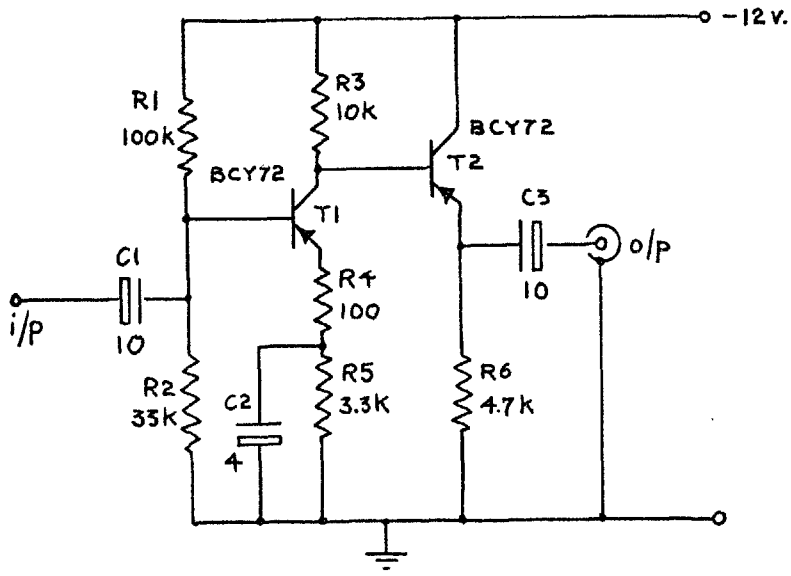
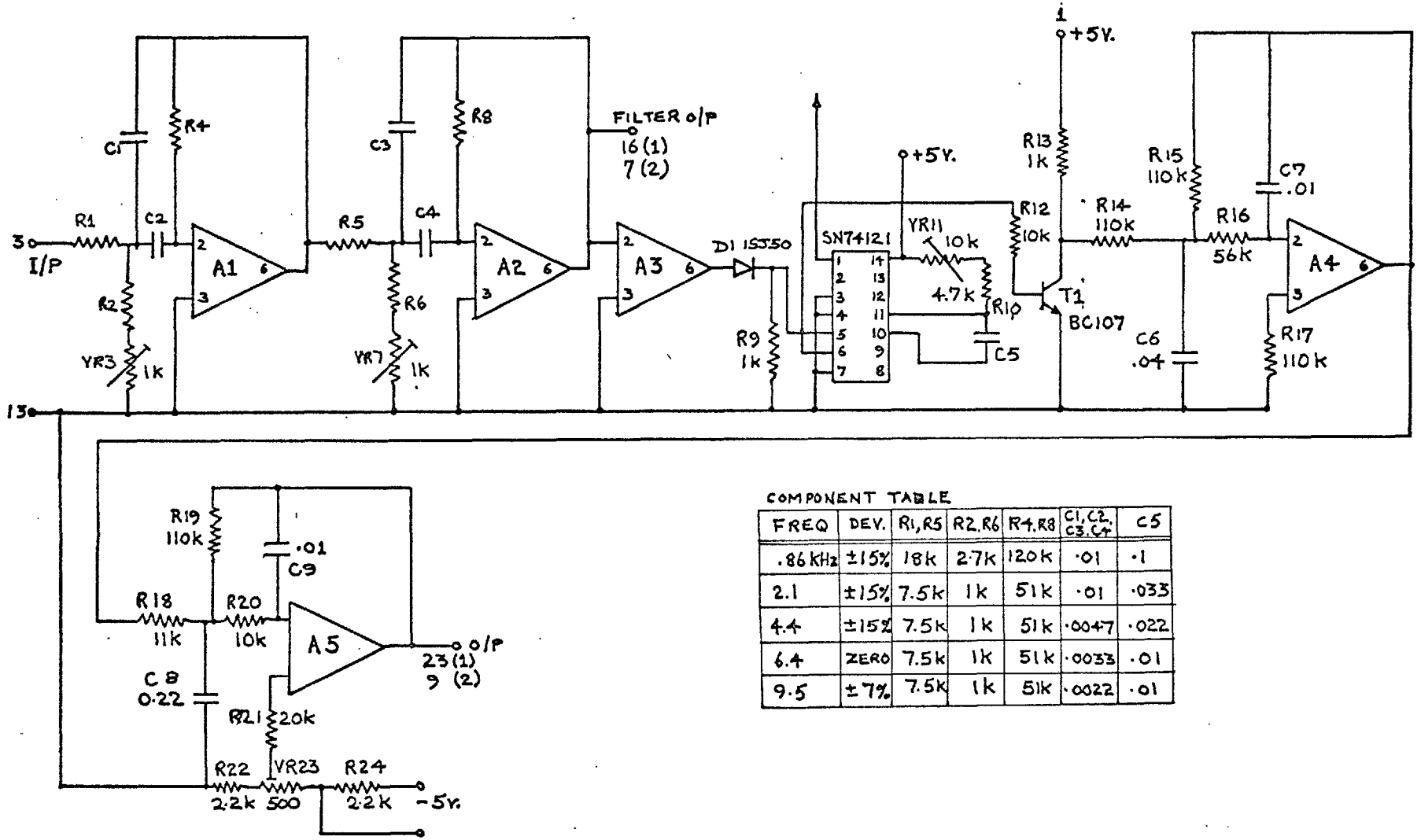


Figure A/12 Receiver output buffer circuit



COMPONENT TABLE

FREQ	DEV.	R1, R5	R2, R6	R4, R8	C1, C2, C3, C4	C5
.86 kHz	±15%	18k	2·7k	120k	·01	·1
2.1	±15%	7.5k	1k	51k	·01	·033
4.4	±15%	7.5k	1k	51k	·0047	·022
6.4	ZERO	7.5k	1k	51k	·0033	·01
9.5	±7%	7.5k	1k	51k	·0022	·01

Figure A/13 Dual demodulator module circuit

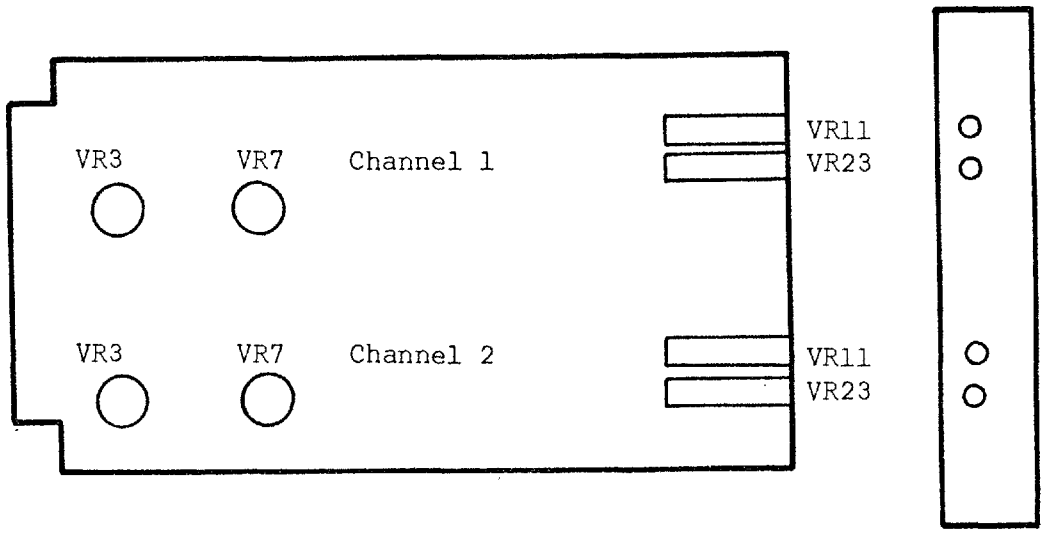


Figure A/14 Dual demodulator module, control layout

Channel	Input freq. kHz	Output Volts
1	f_o 0.860	0.00
	f_1 0.731	-4.00
	f_2 0.989	+4.00
2	f_o 2.100	0.00
	f_1 1.785	-4.00
	f_2 2.415	+4.00

Figure A/15 Dual demodulator settings

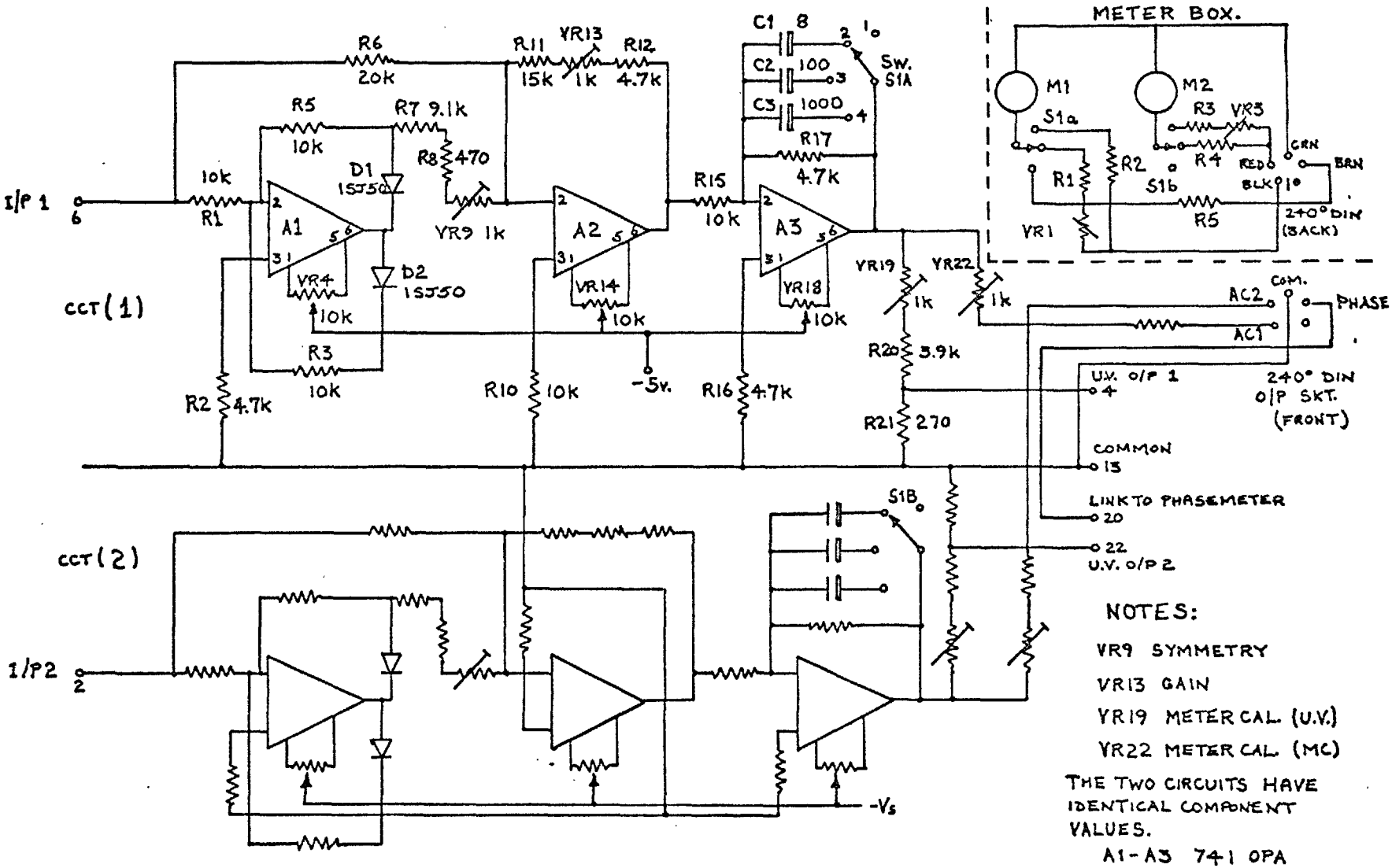


Figure A/16 Dual RMS meter module and meter box circuits

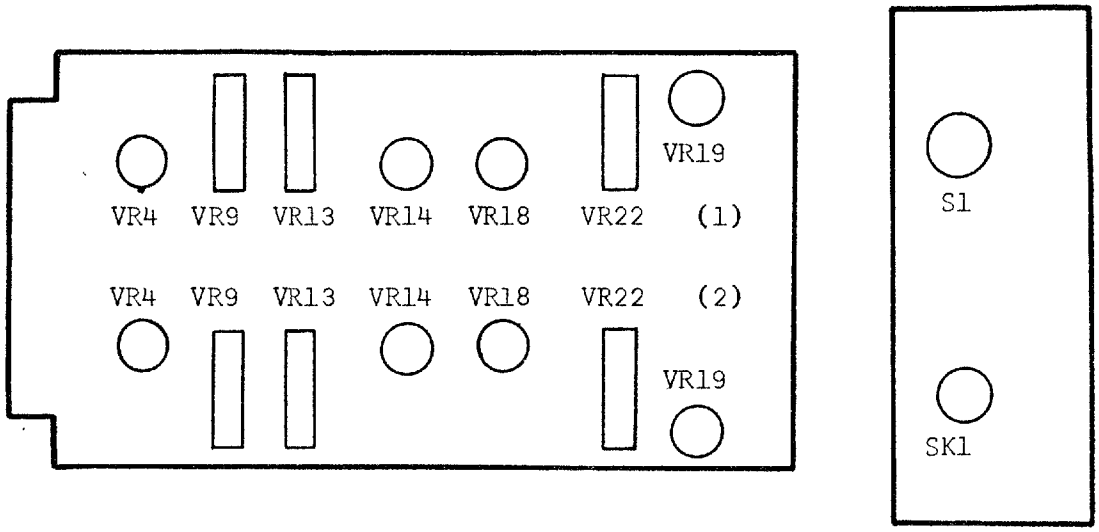


Figure A/17 Dual RMS meter module,control layout

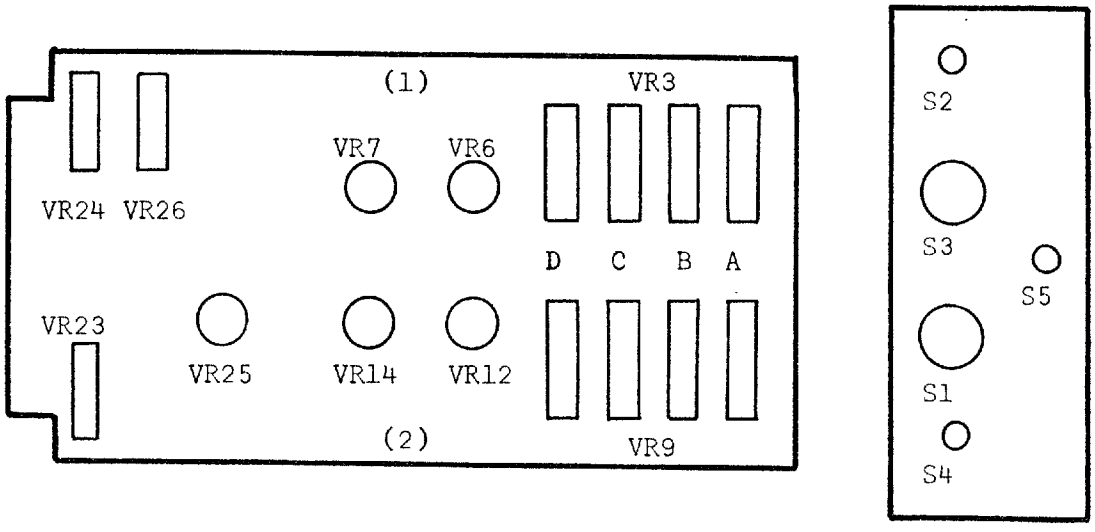


Figure A/18 Filter/Phasemeter module, control layout

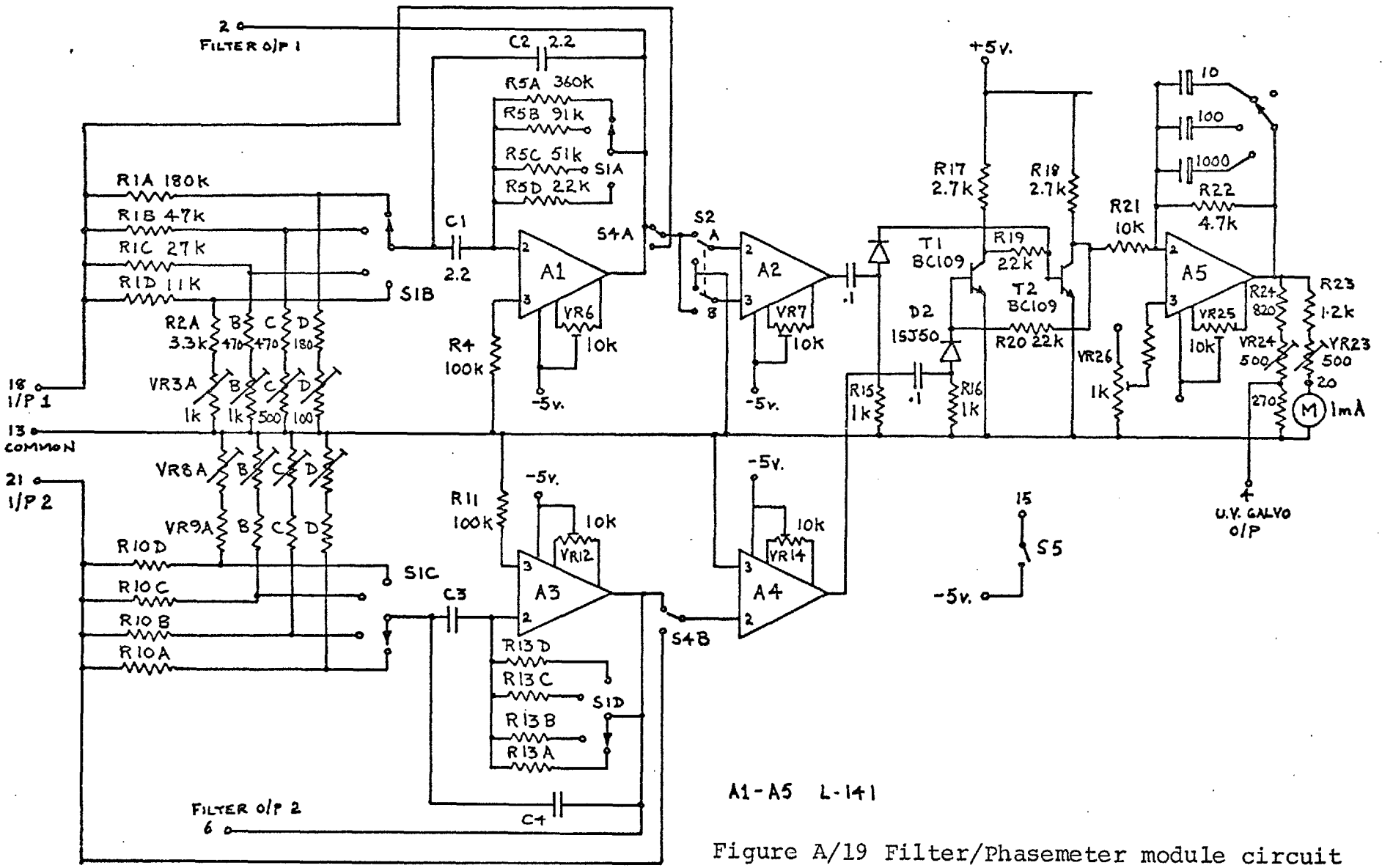


Figure A/19 Filter/Phasemeter module circuit

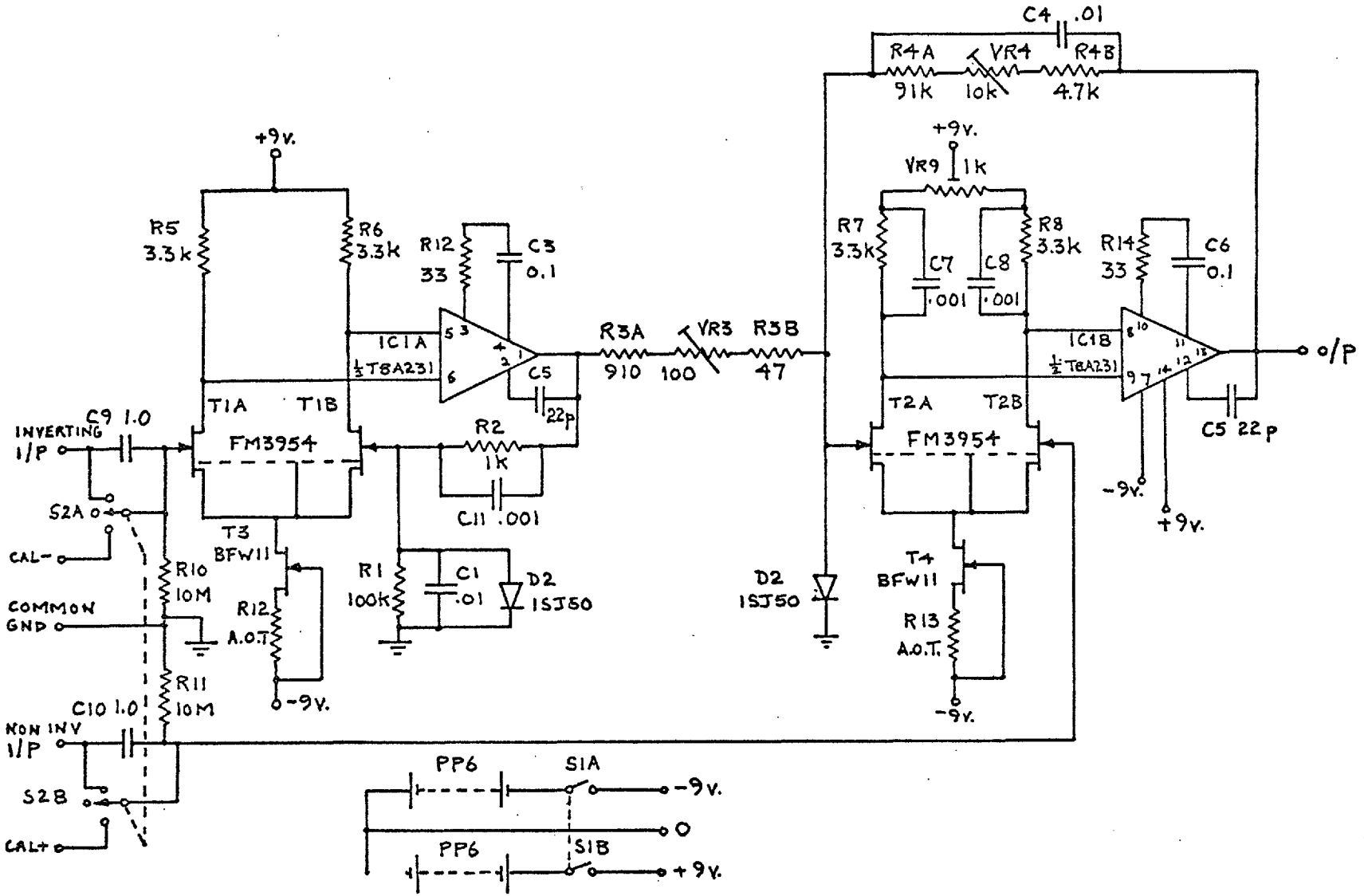


Figure A/20 Electric Field Preamplifier circuit

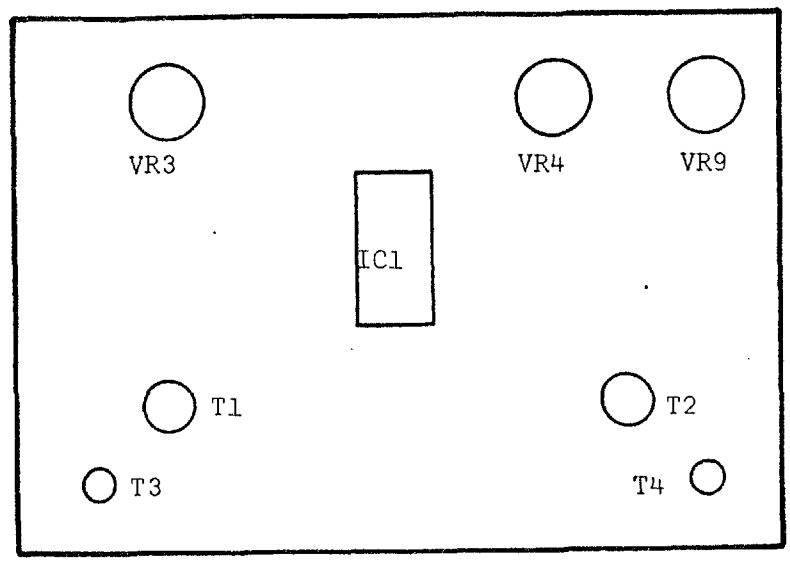


Figure A/21 Electric Field Preamplifier Layout

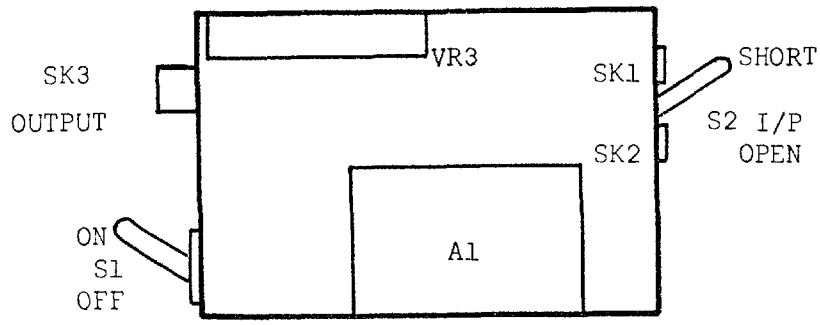


Figure A/22 Magnetometer Preamplifier Layout

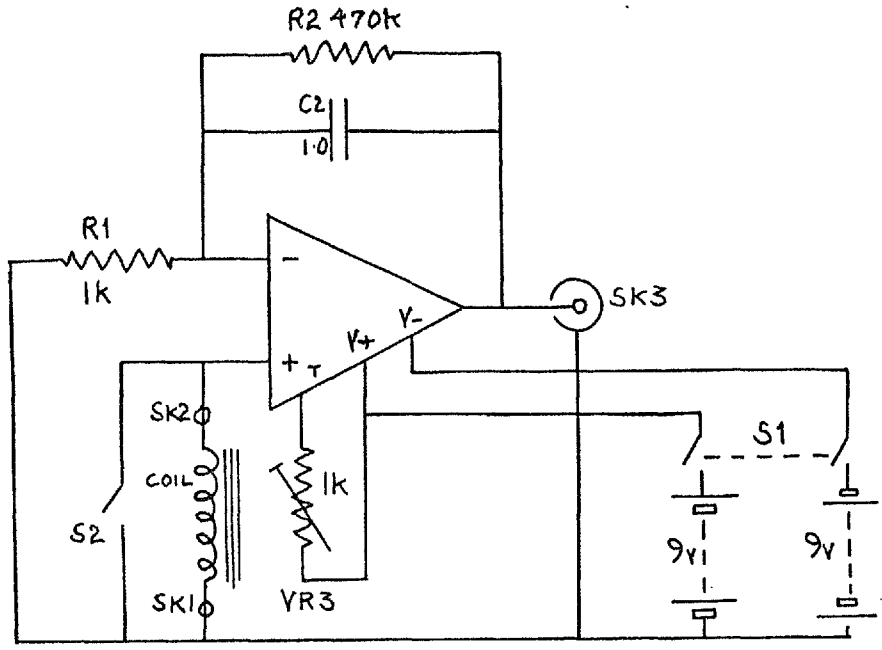


Figure A/23 Magnetometer Preamplifier circuit

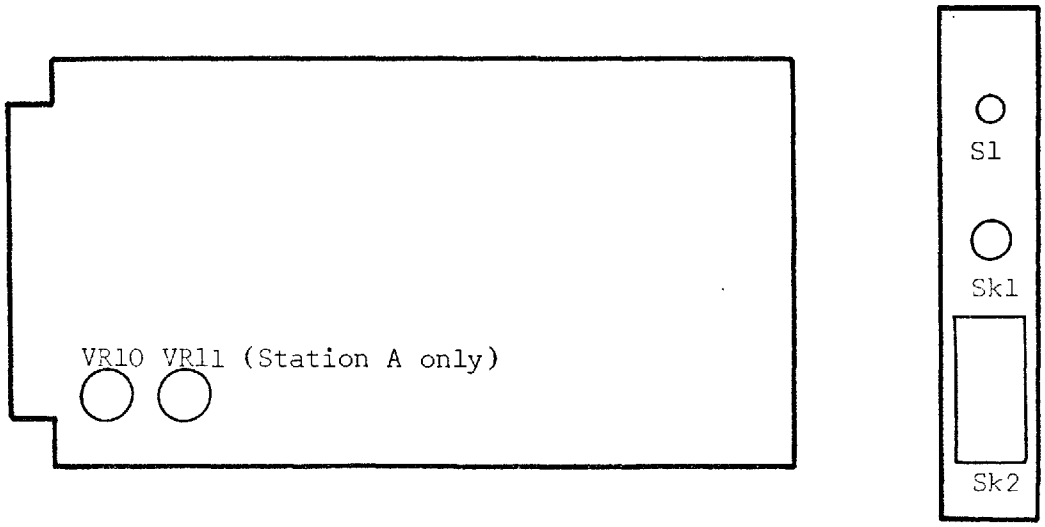


Figure A/24 Power Stabilizer module, control layout

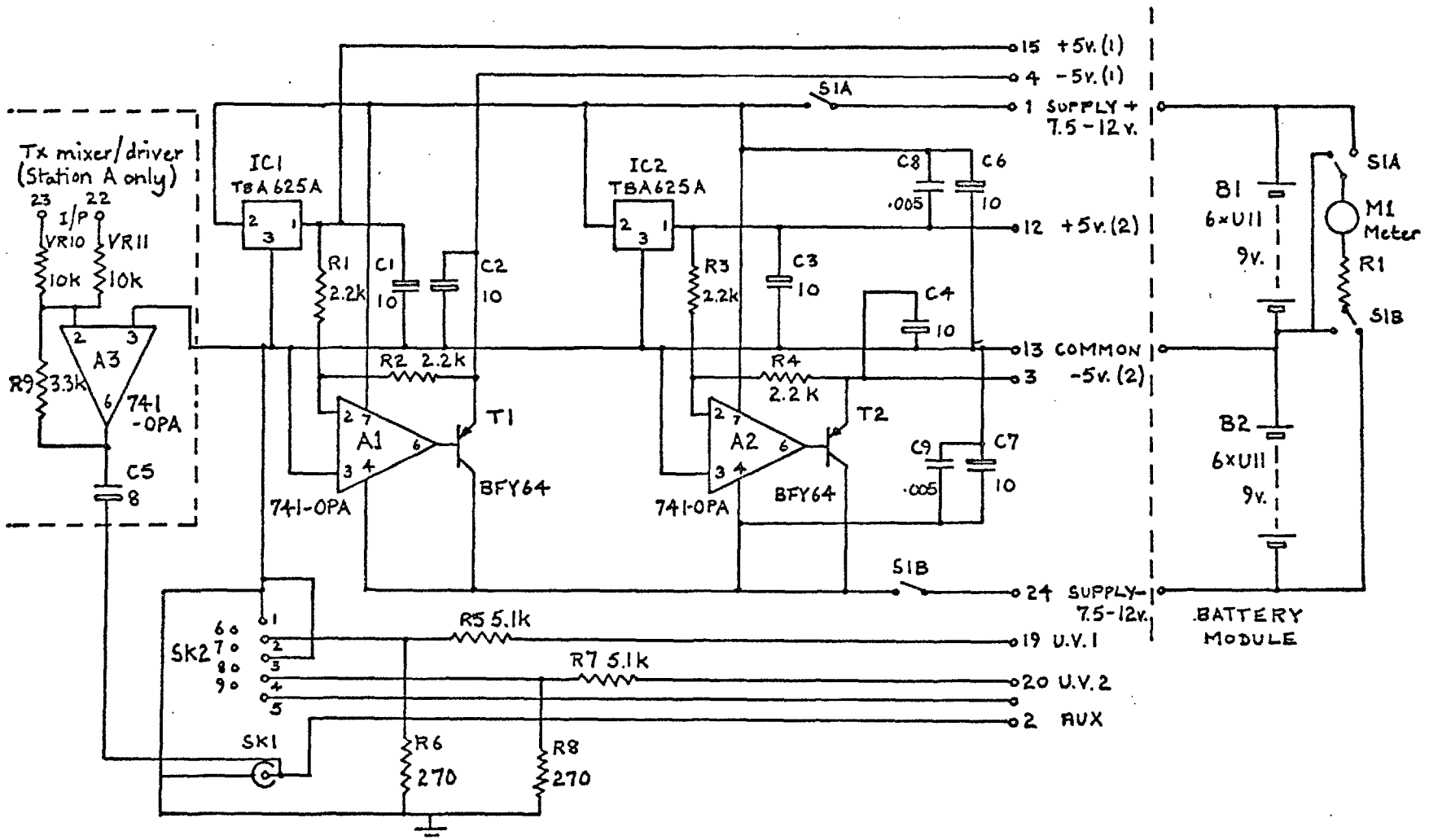


Figure A/25 Power Stabilizer module and battery module circuits

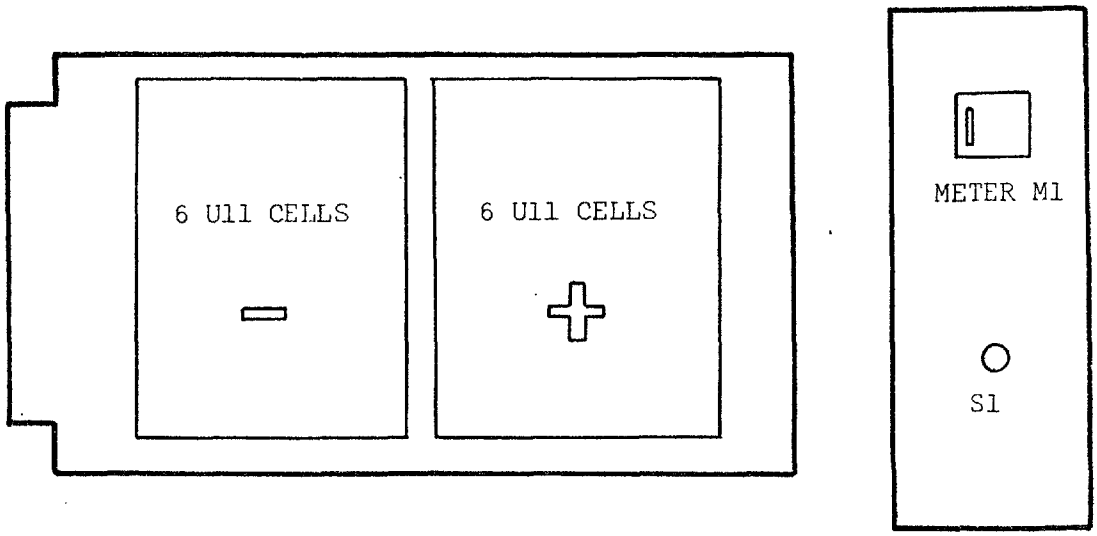


Figure A/26 Battery Module Layout

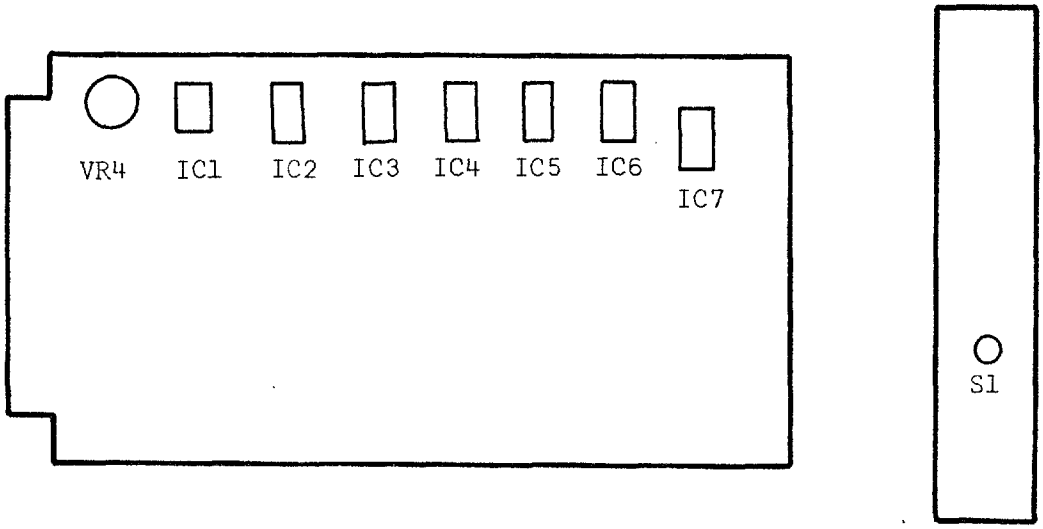


Figure A/27 Timer Module, control layout

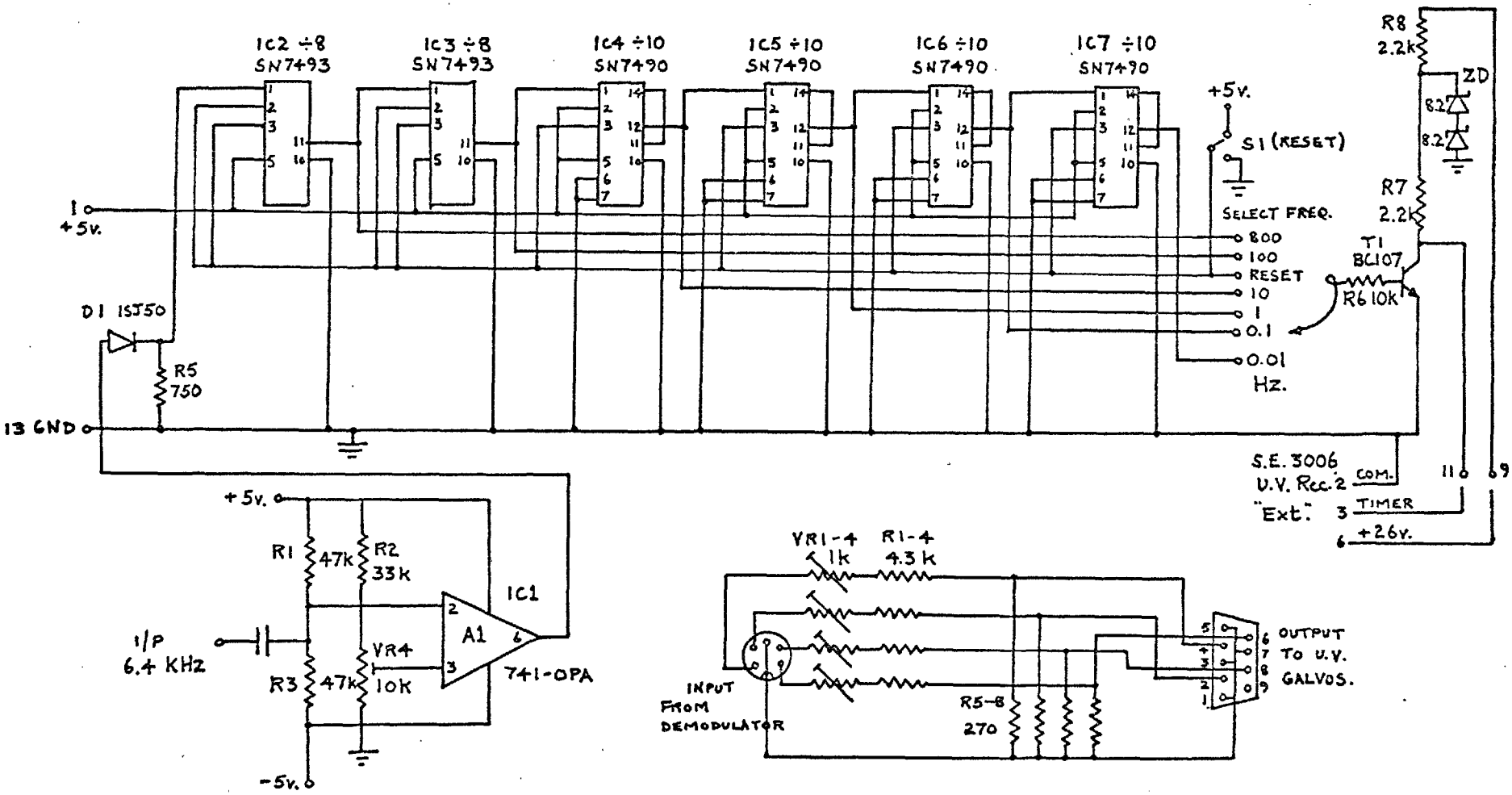


Figure A/28 Timer Module Circuit,
Lennartz demodulator/U.V. recorder interface circuit

APPENDIX B

Submitted for publication to the Geophysical Journal of the Royal Astronomical Society, August 1973

Computer Modelling of Electrical Conductivity Structures

by

K. Williamson
C. Hewlett
H.Y. Tammemagi

Geophysics Department, Imperial College,

London S.W.7

Proposed as a :

Letter to the Editor,
Geophysical Journal of
the Royal Astronomical Society

B.1 The study of the Earth by means of its natural electro-magnetic field has received a stimulus with the development of numerical solutions of Maxwell's equations for two-dimensional conductivity structures (Madden and Swift 1969, Wright 1970). In particular, Jones and Pascoe (1971) and Pascoe and Jones (1972) have published general computer programs which have received widespread application. It is the purpose of this note to reveal and discuss an error in their mathematical derivation.

The Taylor's Series expansions illustrated on p 7 of Jones and Pascoe (1971) can be solved for $(\partial^2 f/\partial y^2)_o$ and $(\partial^2 f/\partial z^2)_o$ by Cramer's Rule or by algebraic manipulation. Substitution into their equation (10) yields

$$f_o\left(2/d_1d_3 + 2/d_2d_4\right) - \eta^2 g_o = f_1\left(\frac{2}{d_1^2+d_1d_3}\right) + f_2\left(\frac{2}{d_3^2+d_2d_4}\right) + f_3\left(\frac{2}{d_3^2+d_3d_1}\right) + f_4\left(\frac{2}{d_4^2+d_4d_2}\right) \qquad (1)$$

It is clear that equation (1) is only equivalent to equation (12) of Jones and Pascoe under special circumstances, that is, when $d_1 = d_3$ and $d_2 = d_4$ (or when $d_1 = d_2 = d_3 = d_4$). Similarly, their equation (13) is incorrect and the error is carried forward in the subsequent derivations. The electro-magnetic responses calculated by the computer programs of Jones and Pascoe (1971) are only correct when the conducting configuration is defined by a grid of identical rectangles or squares.

In order to illustrate that this error can be significant a simple conductivity configuration, as shown in Fig 1, was solved using computer programs based on those listed by Jones and Pascoe (1971) with the substitution of Subroutine BYCOND from Pascoe and Jones (1972). The programs were executed twice, using the corrected formulae for the second run. Both the E-polarization and

H-polarization cases were considered, and a forty by forty mesh was chosen, with irregular grid spacings (Table 1).

The apparent resistivities calculated for H-polarization by the two methods are shown in Table 2; the results deviate by as much as 55% and generally by about 20%. The E-polarization case shows similar discrepancies. (Admittedly an extreme case of irregular grid spacing was chosen).

To achieve continuity of the electro-magnetic fields with the boundary conditions, certain criteria must be observed. The grid size in regions where the field changes rapidly must be sufficiently small to justify the neglect of third and higher order derivatives in the Taylor expansion used to form the finite difference equations. In addition, the distances to the side and bottom boundaries from conductivity contrasts must be large compared with the corresponding skin depths. These essential constraints on grid size can usually only be satisfied by constructing meshes with variable grid spacings. In the vicinity of conductivity contrasts, the grid spacings must be small (relative to the skin depth) increasing in size as they approach the boundaries. Thus, if realistic conductivity models are to be constructed, variable grid sizes are an essential part of the mesh design. This point has not always received the attention it deserves.

Equations (12) and (13) of Jones and Pascoe and the subsequent derivations based on them are incorrect when meshes containing irregular grid spacings are considered. The design of physically realistic conductivity models requires the use of variable grid sizes; equation (1) should therefore be used as a basis for modifying the relevant sections in Jones and Pascoe (1971).

We are grateful to Mr R.B. Matthews for reviewing the first draft of this letter.

Grid Number	H (km)	K (km)	Grid Number	H (km)	K (km)
1	50.0	500.0	21	5.0	2.0
2	20.0	200.0	22	10.0	5.0
3	10.0	100.0	23	5.0	2.0
4	5.0	50.0	24	10.0	5.0
5	2.0	20.0	25	5.0	2.0
6	2.0	10.0	26	10.0	5.0
7	1.0	5.0	27	5.0	2.0
8	2.0	2.0	28	10.0	5.0
9	1.0	1.0	29	5.0	10.0
10	0.5	0.5	30	10.0	20.0
11	1.0	0.2	31	5.0	10.0
12	0.5	0.5	32	10.0	20.0
13	1.0	0.5	33	20.0	10.0
14	0.5	1.0	34	10.0	20.0
15	1.0	0.5	35	20.0	10.0
16	0.5	1.0	36	20.0	20.0
17	1.0	0.5	37	50.0	50.0
18	0.5	1.0	38	100.0	100.0
19	1.0	0.5	39	200.0	200.0
20	0.5	1.0	40	500.0	500.0

Table 1. Grid spacings in kilometres (K-vertical, H-horizontal)
The nine top rows are assigned zero conductivity.
The conductivity contrast lies between horizontal grids 20 and 21.

Grid Number	Apparent Resistivity (computed according to Jones and Pascoe (1971))	Apparent Resistivity (using corrected program)	Difference per cent
2	0.74	0.90	18
3	0.74	0.90	18
4	0.75	0.90	17
5	0.77	0.92	16
6	0.78	0.93	16
7	0.79	0.95	17
8	0.79	0.96	18
9	0.78	0.96	19
10	0.77	0.95	19
11	0.75	0.95	21
12	0.72	0.92	22
13	0.70	0.90	22
14	0.64	0.84	24
15	0.61	0.80	24
16	0.51	0.69	26
17	0.46	0.62	26
18	0.32	0.45	29
19	0.24	0.35	31
20	0.08	0.13	38
21	0.05	0.11	55
22	88.33	130.9	33
23	77.66	109.3	29
24	75.39	104.9	28
25	73.30	100.7	27
26	72.72	99.51	27
27	72.12	98.22	27
28	71.96	97.85	26
29	71.84	97.50	26
30	71.81	97.44	26
31	71.92	97.46	26
32	71.98	97.53	26
33	72.13	97.71	26
34	72.46	98.12	27
35	72.61	98.31	26
36	72.86	98.62	26
37	73.02	98.85	26
38	73.22	99.11	26
39	73.31	99.27	26
40	73.46	99.55	26

Table 2. Apparent resistivities in ohm. metres.
The percentage difference arising due to the mistake in the original program of Jones and Pascoe is shown in Column 4.

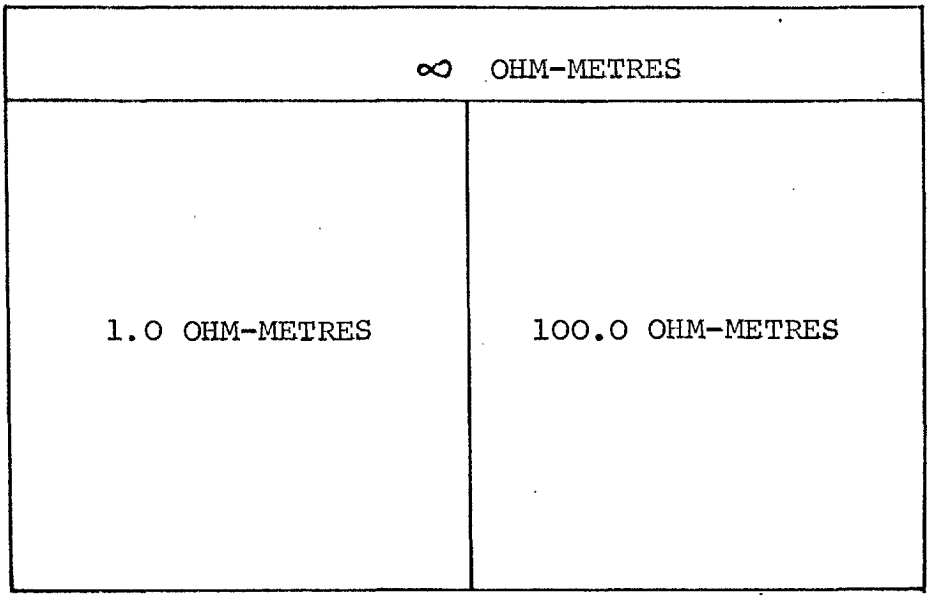


Figure 1 The resistivity model (not to scale)
Frequency = 0.01Hz

References

Jones, F.W., and Pascoe, L.J., 1971. A general computer program to determine the perturbation of alternating electric currents in a two-dimensional model of a region of uniform conductivity with an imbedded inhomogeneity, Geophys. J.R. Astr.Soc. 24, 3-30.

Madden, T.R., and Swift, C.M.Jr., 1969. Magnetotelluric studies of the electrical conductivity structure of the crust and upper mantle, Geophysical Monograph 13, ed. P.J. Hart, American Geophysical Union

Pascoe, L.J., and Jones, F.W., 1972. Boundary conditions and calculation of surface values for the general two-dimensional electromagnetic induction problem, Geophys. J.R. Astr. Soc., 27, 179-193.

Wright, J.A., 1970. Anisotropic apparent resistivities arising from non-homogeneous, two-dimensional structures, Can. J. Earth Sci., 7, 527-531.

LIST OF REFERENCES

AARONS J. Low Frequency E.M. Radiation 10-900Hz J.G.R., 61, No.4, 1956, p 647

AIRY, Sir George. Annual report to the Board of Visitors of the Royal Greenwich Observatory June 1861

BECKER A. Design formulas for Electromagnetic Sensing coils. Geoexploration, 5, 1967, p 81-88

BEER K. Institute of Geological Sciences, Annual Report, H.M.S.O. 1966

BENDERITTER Y., HOANG NGOC THACH, JOLIVET A. Magnetotelluric method for mining exploration English text of 35th meeting of the E.A.E.G., Brighton 1973

BENDERITTER Y., DUPIS A. Technique de mesure de la phase entre champ tellurique et champ magnetique dans la methode de prospection magneto-tellurique. Ann. de Geophys. 21, 1965, 605-606

BERDICHEVSKY M.N. Electrical Exploration with Telluric Currents. English Translation. Quart. Colo. School Mines, Jan. 1965

BLACKMAN R.B. and TUKEY J.W. The measurement of Power Spectra. Dover Publications Inc. N.Y., 1959

BLEANEY B.I. and BLEANEY B. Electricity and Magnetism. O.U.P., London, 1959

BLEIL D.F. Natural Electromagnetic Phenomena below 30 KC/S. Ed. D.F. Bleil from NATO Advanced Study Institute, Bad Homburg, W. Germany Jul. 1963. Plenum Press, N.Y., 1964

BOZFORTH R.M. and CHAPIN D.M. Demagnetizing factors of Rods. J. Appl. Phys. v.13, 1942, p 320

BRAILSFORD F. Physical Principles of Magnetism D. Van Nostrand Co. Ltd. London 1966

BURR BROWN CORP. Active R-C Networks. Burr Brown Research Corp., Tucson, Arizona, 1968

CAGNIARD L. Basic theory of the magnetotelluric method of geophysical prospecting, Geophysics, 18, 1953, 605-635

CANTWELL T. Detection and analysis of low frequency magnetotelluric signals. PhD thesis, M.I.T. Cambridge, Massachusetts, 1960

CHAIZE L. and LAVERGNE M. Signal et Bruit en Magnetotellurique. Geophys. Prosp. 18(1), March 1970, 64-87

CLAYTON P. Operational amplifiers. Wireless World, Vol 75, Apr. 1969, 154-159

COGGON J.H. Electromagnetic and electrical modeling by the finite element method. Geophysics 36(1) 1971, 132-155

COOLEY J.S. and TUKEY J.W. An algorithm for the machine calculation of complex Fourier series Math. Computation 19, 1965, 297-301

d'ERCEVILLE I. and KUNETZ G. The effect of a fault on the Earth's natural Electromagnetic field Geophysic, Vol 27(5), Oct. 1962, 651-665

EDMONDS E.A., McKEOWN M.C. and WILLIAMS M. British Regional Geology. South West England, H.M.S.O., 1969

FAIRCHILD. The application lf Linear Microcircuits. By the Applications Engineering Staff of the S.G.S. Fairchild Group. 2nd issue, 1967

FENNING P. Summ. Prog. Geol. Surv. for 1964 p 85 H.M.S.O. 1965

FORDE R.D. Magnetotellurics - a dissertation submitted for the D.I.C. and the Degree of M.Sc. at London University 1972.

FULLER B.D. Electromagnetic response of a conductive sphere surrounded by a conductive shell. Geophysics 36(1), 1971, 9-24

GALEJS J. Frequency Variations of Schumann Resonances J.G.R. (Space Physics) 75(16), June 1970, 3237-3251

GEYER R.G. The effect of a dipping contact on the Behaviour of the Electromagnetic field Geophysics 37(2), Apr. 1972, 337-350

GIRLING F.E.J. and GOOD E.F. Active Filters - A practical approach on feedback amplifier theory 1. Survey of circuits. Wireless World, Vol 75, Aug. 1969, 348-352

HERMANCE J.F. and GRILLOT L.R. Correlation of Magnetotelluric, Seismic and Temperature Data from Southwest Iceland. J.G.R. 75(32) 1970, p 6582

HOPF L. Introduction to the Differential Equations of Physics. Dover Publications Inc., N.Y. 1948

JOLIVET A. Étude d'un équipement léger pour la prospection magneto-tellurique de sub surface. Ph.D. Thesis, Faculté des Sciences de Paris, 1969

JONES F.W. and PASCOE L.J. A general computer program to determine the perturbation of alternating electric currents in a two-dimensional model of a region of uniform conductivity with an imbedded inhomogeneity. Geophys J.R. Astr. Soc. 24, 1971, 3-30

JONES F.W. and PASCOE L.J. The perturbation of alternating geomagnetic fields by three dimensional conductivity inhomogeneities. Geophys J.R. Astr. Soc. 27, 1972, 479-485

KELLER G.V. and FRISCHKNECHT F.C. Electrical Methods in Geophysical Prospecting. Pergamon Press, 1966

KLEWE H.R.J. Interference between Power Systems and Telecommunication lines. Report, Ref. M/T 126, Electrical Research Assoc. G.B., 1958

LAIRD C.E. and BOSTICK F.X., Jr. One dimensional Magnetotelluric Inversion Techniques. Electrical Geophysics Research Laboratory University of Texas. Technical Report No.101 Dec.1, 1970

LLANWYN-JONES D. and KEMP D. Experimental and Theoretical observations on the transient Excitation of Schumann Resonances. J. Atmos. & Terr. Phys. 32, 1970, 1095-1108

LUTSENKO B.N. and PUSHNOI B.M. Applications of the Mutual-Correlation method for measuring the Angle of Polarization of the Magnetic Component of Natural Electromagnetic Fields. Izv. Earth Physics Series 3, 1965, pp 103-108

NEGI J.G. Electromagnetic screening due to a disseminated spherical zone over a conducting sphere. Geophysics 32, 1967, 69-87

NEGI J.G. and SARAF P.D. Impedance of a Plane Electromagnetic Wave at the Surface of a Layered Conducting Earth with Dipping Anisotropies. Geophys. Prosp. 20(4), Dec. 1972, 785-799

N.S. NATIONAL SEMICONDUCTORS CORP. National Linear Applications Handbook. National Semiconductor Corp., 1972

NISENOFF. Superconducting Magnetometers with sensitivities approaching 10^{-10} gauss. C.N.E.S. conference on low magnetic fields, Paris, 1969

PARASNIS D.S. Mining Geophysics. Elsevier Publishing Co., Amsterdam, 1966

PASCOE L.J. and JONES F.W. Boundary conditions and calculation of surface values for the general two-dimensional electromagnetic induction problem. Geophys J.R. Astr. Soc., 27, 1972 p 179-193

PATRICK F.W. and BOSTICK F.X., Jr. Magnetotelluric Modeling Techniques. Electrical Geophysics Research Laboratory, University of Texas. Research report no.58 Jan 7, 1969, 86pp

RANKIN D. and BURKE M.D. A New Induction Coil Magnetometer for Geomagnetic Sensing. Workshop on Electromagnetic Induction, University of Edinburgh, Sept. 1972

REDDY I.K. and RANKIN D. Magnetotelluric effect of Dipping Anisotropies. Geophys. Prosp. 19(1), Mar. 1971, 84-97

ROY J.L., REYNOLDS J. and SANDERS E. An astatic magnetometer with negative feedback. Pub. Earth Physics Branch 42, No.5, 1972, 167-182

SCHUMANN W.O. On the radiation-free self oscillations of a conducting sphere, which is surrounded by an air layer and an ionospheric shell (In German) Z. Naturforsch., 72, 1952, 149

SCINTREX LTD. Scintrex georama newsletter. Scintrex Ltd., Ontario, Canada. August 1972

SHAND J.A. Some Quantitative Characteristics of the Schumann E.L.F. natural electromagnetic Background. Can.J. Phys. 44(3), Mar.1966, p 449-459

SILVESTER P. and HASLAM C.R.S. Magnetotelluric Modelling by the Finite Element Method. Geophys. Prosp. 20(4), 1972, 872-891

SIMS W.E. and BOSTICK F.X., Jr. Methods of Magnetotelluric analysis. Electrical Geophysics Research Laboratory University of Texas, Technical Report no.58 Jan 7, 1969

SLANKIS J.A. and BECKER A. Telluric and Magnetotelluric Measurements at 8Hz. Trans. Soc. Min. Eng. AIME 244, June 1969, 237-244

SLANKIS J.A., TELFORD W.M. and BECKER A. 8Hz Telluric and Magnetotelluric Prospecting Geophysics 37(5), oct 1972, p 862-878

SPARROW J.G. and NEY E.P. Lightning observations by satellite. Nature 232, Aug. 1971, 540-541

SRIVASTAVA S.P. Method of Interpretation of magnetotelluric data when the source field is considered. J.G.R. 70, 1965, 945-954

SWIFT C.M., Jr. A magnetotelluric investigation of an electrical conductivity anomaly in the Southwestern United States. PhD. thesis M.I.T., Cambridge, Massachusetts, 1967.

SWIFT C.M., Jr. Theoretical Magnetotelluric and TURAM response from two dimensional inhomogeneities. Geophysics 36(1), 1971, 38-52

TAMMEMAGI H.Y. and LILLEY F.E.M. A Magnetotelluric Traverse in Southern Australia. Geophys. J.R. Astr. Soc. 31, 1973, 433-445

TERMAN F.E. Radio Engineers Handbook. McGraw Hill, New York, 1942.

VITKOVITCH D. Field Analysis. Experimental and Computational methods. Ed. D. Vitkovitch. D. Van Nostrand Co. Ltd., London, 1966

VLADIMIROV V.A. and KLEIMENOVA N.G. On the structure of the Earth's natural electromagnetic field in the frequency range of 0.5-100 cps. Bull. Izv. Acad. Sci. USSR Geophys. Ser. (A.G.U. translation), 1962, p 852

VOZOFF K. The Magnetotelluric Method in the Exploration of Sedimentary Basins. Geophysics 37(1), Feb. 1972, p 98-141

WAIT J.R. Electromagnetic waves in stratified media Pergamon Press, London, 1962

WARD S.H. et al. Prospecting by use of natural alternating magnetic fields of audio and sub audio frequencies. Canadian Mining and Metallurgical Bulletin, Aug. 1958

WORD D.R., SMITH H.W. and BOSTICK F.X. An investigation of the Magnetotelluric tensor impedance method. Electrical Geophysics Research Laboratory University of Texas. Technical Report no. 82, Mar.15 1970, 264pp

WRIGHT J.A. Anisotropic apparent resistivities arising from non-homogeneous, two-dimensional structures. Can. J. Earth Sci. 7, 1970, 527-531

YUNGUL S.H. Magnetotelluric Sounding three layer interpretation curves. Geophysics 26(4), 1961, p 465

YUNGUL S.H. Measurement of telluric "Relative Ellipse area" by means of"Vectograms" Geophysics 33, 1968, 127-131

YUNGUL S.H., HEMBREE M.R. and GREENHOUSE J.P. Telluric anomalies associated with isolated reefs in the Midland Basin, Texas. Geophysics 38(3), 1973, 545-556

ZEPLER E.E. and PUNNET S.W. Electronic Devices and Networks. Blackie & Son Ltd., London, 1963